Synthetic modelling of core-mantle boundary topography

By Loes Rutten
Supervisors: Arwen Deuss & Jeannot Trampert

January 13, 2017

Abstract

In this study, the resolvability of core-mantle boundary topography was studied using synthetically generated seismic body waves. The full-waveform synthetic seismograms calculated at 2130 stations due to four earthquakes on the equator in the PREM model were compared to the seismograms for an Earth consisting of PREM and the core-mantle boundary (CMB) topography model of Li *et al.* (1991a) scaled to a peak-to-peak amplitude of 8km. The ray theoretical predictions for travel time delays due to CMB topography were compared to delays measured from cross-correlation of full waveform synthetic seismograms generated using SPECFEM3D. The assumption that delays caused by mantle heterogeneities and delays caused by CMB topography are linearly additive was investigated by comparing the separate travel time differences due to mantle heterogeneities and CMB topography to the time difference due to their combined effects. Single and double P and S-wave reflections were studied, as well as Pdiff and Sdiff. We found that ray theory correctly predicts that uplifted topography results in early arrivals of PcP, ScP, ScS, ScSScS, ScSScP, ScPPcP and PcPPcP, provided that the arrivals do not interfere with other phases, that reflection coefficients are higher than 0.1 and that angles of incidence are sufficiently sharp. For all core reflections, delays predicted by ray theory are equal or larger in magnitude than the delays observed in synthetic seismograms, by factors 1.0 to 2.5. For the diffracted phases Pdiff and Sdiff, we found a relationship between positive CMB topography and late arrivals. This delay as a response to uplifted topography can be explained by longer arclengths at larger core radii combined with slow propagation velocities sampled at the underside of the CMB. Linear decomposition is valid for all phases mentioned above.

Contents

1 Introduction

The core-mantle boundary (CMB) is the Earth's largest discontinuity, marking a chemical transition from the solid silicate-rich mantle to the liquid iron-nickel rich outer core. This change in material properties causes the density to double and P-wave velocity to drop. S-waves completely vanish as transverse motion is not possible through liquid media. Although the CMB is often depicted as a smooth and spherically symmetric surface, it has been suggested that there exist areas of heterogeneous chemistry and topography on the CMB, analogous to continents at the Earth's surface (Creager & Jordan 1986).

From a geophysical point of view, the CMB is interesting to study because its structure may give relevant information about the processes that take place at the base of the mantle, which in turn have implications on the dynamics in the rest of the mantle. Forte *et al.* (1995) deducted from the free retrograde core nutation period that the CMB has an excess dynamic ellipticity, beyond hydrostratic equilibrium. They suggested that the most viable mechanism causing the excess ellipticity is the dynamic stress exerted on the CMB by the thermal convective flow in the mantle. In a study on the origin of LLSVPs, Lassak & McNamara (2007) simulated the dynamic response of the CMB to thermal upwellings and downwellings and to diffent types of thermochemical piles. They found that subduction related downwellings result in CMB depressions, and that upwellings result in elevated CMB topography. On the other hand, thermochemical piles leave a relatively flat and slightly positive signature on CMB topography.

In a more recent study by Soldati *et al.* (2012), CMB topography and mantle velocity were treated as joint parameters. Assuming that the CMB should be depressed under relatively dense and sinking regions of the lowermost mantle, and uplifted under less dense, rising ones, and assuming that the effects of thermal heterogeneity govern over the effects of compositional heterogeneity, they were able to produce CMB topography maps that fit seismic observations equally well as purely seismic ones. This shows that the predictions on the qualitative relationship between mantle dynamics and CMB topography are valid. However, comparing the predictions on the peak-to-peak amplitude between mantle convection models and seismic data studies, Koelemeijer *et al.* (2012) found that CMB topography is overestimated by dynamic models and that constraints on peak-to-peak amplitude should be inferred from seismology.

There is currently no agreement on peak-to-peak amplitude nor spatial distribution of CMB topography. Hager *et al.* (1985) found an anti-correlation between long-wavelength components of the Earth's geoid and CMB topography, with a best fit for 1.5 km peak-to-peak topography. Several studies on normal modes suggest peak-to-peak amplitudes of approximately 4 km (Li *et al.* 1991a) to 5 km (Ishii & Tromp 1999). The trade-off between the density heterogeneity in the lowermost mantle and CMB topography is a large factor of uncertainty for estimates from normal modes.

An overview of CMB topography reconstructions based on bodywave inversions is given in Table 1. The first CMB topography studies date from the 1980s and were based on PcP and different branches of PKP (Creager & Jordan 1986; Morelli & Dziewonski 1987). Although the range in published peak-to-peak amplitude has converged to a range of 3 to 8 km in the subsequent decades, a discrepancy between PcP and PKP solutions remains despite improvements in the seismic data (Rodgers & Wahr 1993; Boschi & Dziewonski 2000; Soldati *et al.* 2003). Several causes were hypothesised including radial anisotropy of the lower mantle, outer core heterogeneity and the irresolvability of D" heterogeneity and CMB topography (Garcia & Souriau 1999).

Body wave inversions are based on ray theory. Ray theory provides expressions for travel times, paths and amplitudes of waves of infinite frequencies. Although ray theory has proven to be an effective tool to map large parts of the Earth's interior, it does not provide a description for effects originating from the finite nature of the frequency of the waves, including diffraction and Fresnel zones (Hubral *et al.* 1993).

By means of forward modeling, it is possible to generate synthetic seismograms that follow from the solution of the full wave equation, which includes the effects due to the finite nature of seismic waves. These full-waveform synthetic seismograms can be used to investigate whether proposed CMB topography models indeed affect the waveform and arrival times as ray theory supposes, or whether there is a descrepancy between inferences drawn from finite frequency and infinite frequency ray theory at the CMB. Forward modeling of separate and combined contributions of CMB topography and mantle structure also allows us to investigate the resolvability of these two features.

The methods in this research are analogous to those of Koroni and Trampert (2012). In their study on the topography of 410 and 660 km discontinuites, synthetic seismograms were used to compare the effect of discontinuity topography on SS waveforms to the effects predicted by ray theory. Their main findings were that ray theory is able to retrieve the right sign of the topography but underestimates the amplitude. Moreover, they found that the effects of mantle heterogeneity and discontinuity topography are not additive.

In this study, synthetically generated seismograms are used as a tool to investigate whether CMB topography can be resolved by ray theory and whether volumetric heterogeneity and CMB topography are linearly independent variables.

Publication	Phases	Amp.	Main depressions	Main uplifts
Creager & Jordan 1986	P'DF, PKP2	±20 km	Australia, NA, SA	Pacific, EuA
Morelli & Dziewonski 1987	PcP, PKP_{bc}	±6 km	JAP, SA, NZ	Azores, EP
Rodgers & Wahr 1993	PcP	±6 km	CP, Australia	South Asia, EP
	$PKP_{ab/bc/df}$	±8 km	*Inconsistent*	*Inconsistent*
Vasco *et al.* 1998	PcP	±6 km	SA, Australia	Eurasia
Boschi & Dziewonski 2000	P, PcP	±7 km	SA	Pacific
	$PKP_{bc/df}$	±7 km	SP	EA
Sze & van der Hilst 2002	PcP, $PKKP_{bc/df}$ $PKP_{ab/bc/df}$	±3 km	EuA, NA	SEA, EP
Soldati *et al.* 2003	P, PcP	±7 km	CP, Atlantic	EA, SA
	PKP_{bc}	±4 km	SA	EA
	PKP_{df}	±7 km	SA (lat$>45°$)	EA, CA
Tanaka 2010	P4KP-PcP	±2 km	CP, Afr, Australia	SP, EuA

Table 1: Summary of reconstructions of CMB topography using body waves. The abbreviations have the following meaning: JAP = Japan, SA = South America, CA = Central America, NA = North America, NZ = New Zealand, CP = Central Pacific, EP = Eastern Pacific, SP = South Pacific, EA = East Asia, SEA = South East Asia, EuA = Eurasia, Afr = Africa

2 Methods

In order to investigate whether ray theory is a reliable method to deduce CMB topography from travel time measurements of seismograms, we compare forward calculations of ray theorical delays induced by CMB topography to full-waveform synthetic seismograms for core reflected and core diffracted phases. In the following sections, firstly the main properties of the studied phases are explained. The next section explains how ray theoretical delays are calculated. The last method section explains how full-wavefrom synthetic seismograms are calculated using SPECFEM3D_GLOBE and how travel time delays are calculated using cross-correlation. Then, it is explained how these delays measured from cross-correlation are used to investigate the relationship between CMB topography and travel time delays, as well as the assumption that delays due to CMB topography and mantle heterogeneity are linearly additive. Relevant concepts from theoretical seismology are briefly restated where needed, but basic knowledge of the physical and mathematical description of seismic waves is assumed. A complete treatise of seismology can be found in *Introduction to Seismology* (Shearer 2009) and a mathematical description of seismic waves in *Quantitative Seismology* (Aki and Richards 2002).

2.1 Seismic phases

The seismic phases that contain information on CMB topography are phases that interact with the CMB via reflection, refraction or diffraction. In this study we focus on different configurations of P and S waves of single and double core reflections as well as diffracted phases.

The single core reflections PcP, ScP, PcS and ScS travel from a source to a bouncepoint on the CMB, where they are reflected towards the receiver. PcP and ScS phases travel along the same symmetric path, but ScS travels with a lower velocity. PcS and ScP phases have nearly the same arrival time for near-surface earthquakes, but pierce the CMB at different epicentral distances. The ScP phase has a bouncepoint at a relatively small angle from the source because S waves are refracted less than P waves. The PcS wave recorded at the same receiver bounced off the CMB at a relatively small angle from the receiver. The ray paths of these single reflections are shown in Figure 1a.

The double core reflections studied are PcPPcP, ScPPcP, ScPScP, ScSScP and ScSScS. Their initial path is similar to single reflections, but they are reflected back down into the mantle upon reaching the Earth's surface. The position of the bouncepoints again depends on the configuration of P and S segments, as is shown in Figure 1b.

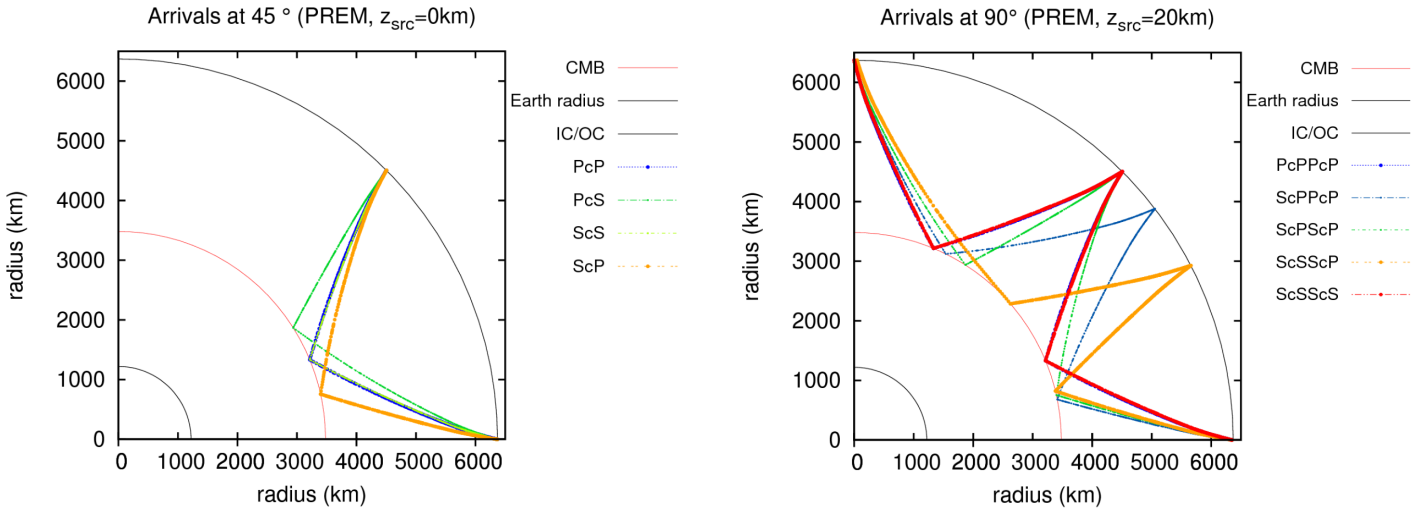

(a) (b)

Figure 1: Figure 1a shows the ray paths of PcP, ScP, PcS and ScS recorded by a receiver at 45° epicentral distance. Figure 1b shows ray paths of PcPPcP, ScPPcP, ScPScP, ScSScP and ScSScS recorded at 90° epicentral distance.

The diffracted phases Pdiff and Sdiff are also sensitive to CMB topography. As is shown in Figure 2a, these phases reach the CMB at a high angle of incidence and are subsequently diffracted along the CMB before travelling back to the Earth's surface. Although the diffractive nature of these phases does not allow for a ray theoretical estimate, we can use synthetic seismograms to study the relationship between the sign and magnitude of CMB topography and delays in arrival time.

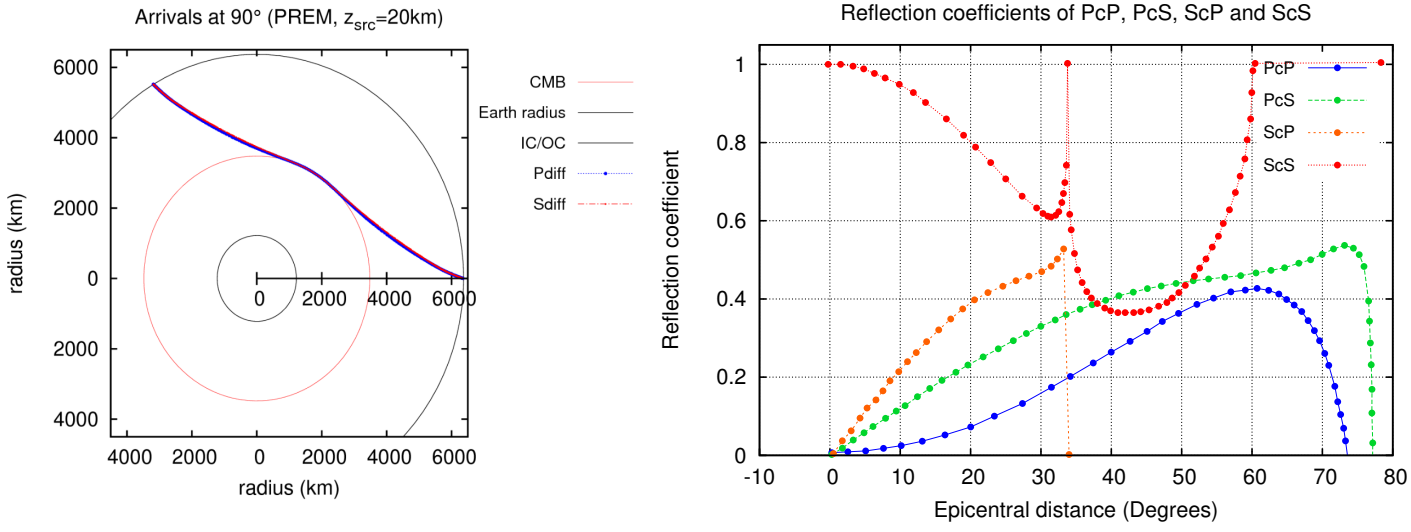

(a) (b)

Figure 2: Figure 2a shows ray paths of Pdiff and Sdiff recorded at 90° epicentral distance. Figure 2b shows the reflection coefficients of PcP, PcS, ScP and ScS. A reflection coefficient of 1 means the complete wave is reflected, a reflection coefficient of 0 means the complete wave is transmitted. This figure is a combination of Figure 7.25 and 7.26 from *Seismic waves and sources* (Ben-Menahmen & Singh 2012).

In order to know at what time a phase of interest arrives at a seismic station, we use the travel time curve shown in Figure 3. It shows the arrival time of different phases as a function of epicentral distance between source and receiver. When two phases in this figure cross or overlap, they arrive (nearly) simultaneously. Due to a superposition of waveforms, it may be more difficult to determine the exact arrival time in synthetic seismograms at epicentral distances where phases overlap.

The amplitude of the reflected phases depends on the reflectance at the bouncepoint. If the reflection coefficient is close to one, the amplitude of the reflected phase is high. If the reflection coefficient is low, most of wave's energy is transmitted into the core. The reflected phase subsequently has a lower amplitude, which may be too weak to be recorded at the seismogram. The reflection coefficients of single core reflections are shown in Figure 2b. The reflection coefficient of PcP remains below 0.1 at epicentral distances below 20°. ScP, PcP and PcS cease beyond 34°, 74° and 77° respectively whereas the reflection coefficient of ScS remains relatively high at all epicentral distances where it exists.

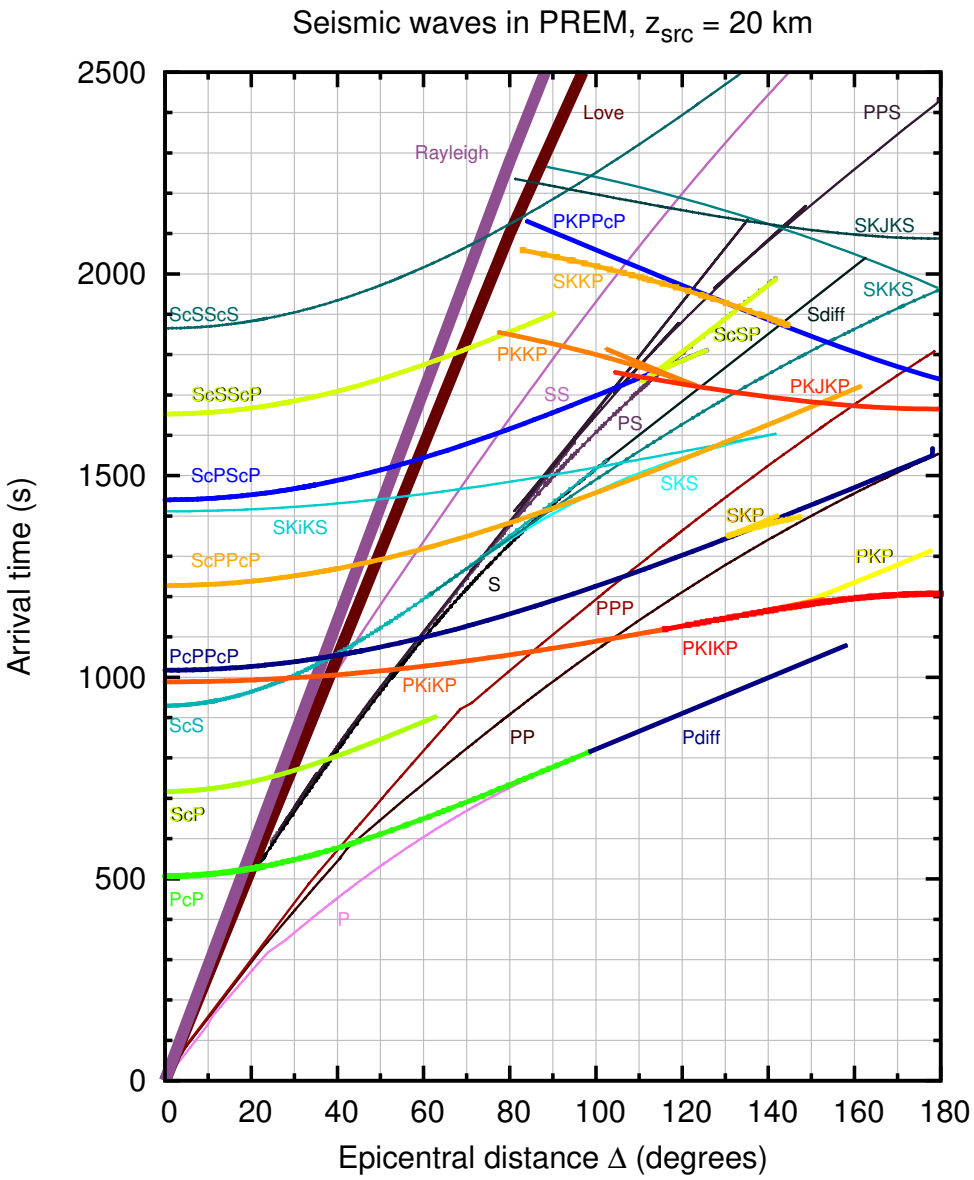

Figure 3: Travel time curve of the studied phases, as well as other phases that may interfere with them. The travel time curves were calculated using TauP (Crotwell *et al.* 1999) inside the PREM model for an earthquake at 20 km depth.

2.2 Ray theoretical delay

Ray theory is the high frequency approximation of the solution of the elastic wave equation. It provides relatively simple expressions for wave properties including travel times and amplitudes, but does not include effects of scattering and diffraction. Ray theory lies at the base of several seismological techniques including CMB topography reconstructions. By comparing forward calculations of the ray theoretical arrival times of seismic waves in an Earth with CMB topography to the measured time difference between synthetically generated full waveforms in Earth models with and without topography, we can evaluate the reliability of ray theory as a method to measure CMB topography.

We first need to calculate the ray theoretical predictions for travel time delays due to CMB topography in order to be able to compare them to the delays calculated from full-waveform synthetic seismograms. The ray theoretical travel time is calculated using TauP (Crotwell *et al.* 1999), a tookit that calculates ray theoretical arrival times for seismic phases in a 1D sperically symmetric background model. The delay times due to CMB topography were approximated by varying the CMB depth of the input model PREM for values between +9km and -9km over the range of relevant epicentral distances for PcP, ScS, ScP and PcS reflections. For each phase, a 3rd order polynomial fit was made to interpolate the difference in arrival time as a function of topograpy and epicentral distance. The fit for PcS is shown in Figure 4a. Given the epicentral distance between a source and a station and the topography at the location of the bouncepoint, the fit provides us with the predicted travel time delays under the assumption that ray theory holds.

In literature, the ray theoretical difference in arrival time due to topography is often approximated as

$$\delta t = 2h\cos(i)/v \tag{1}$$

where h is the height of the CMB topography, i is the angle of incidence of the wave at the CMB, and v is the velocity of the wave (Koroni & Trampert 2012). This approximation describes the delay due to topography well at small epicentral distances, but overestimates the delay at larger epicentral distances. This discrepancy is also visible in Figure 4a. The full-waveform synthetic seismograms were also compared to ray theoretical predictions calculated from this expression, allowing us to rule out if the approximation leads to significantly different final conclusions. The angle of incidence $\angle i$ was calculated as a function of the epicentral distance Δ, the Earth radius R_e and the core radius R_c and by approaching the ray paths as straight lines from source to bouncepoint to receiver:

$$\angle i = \arctan\left(\frac{R_e \sin(\Delta/2)}{R_e\cos(\Delta/2) - R_c}\right) \tag{2}$$

The geometry of this calculation is shown in Figure 4b.

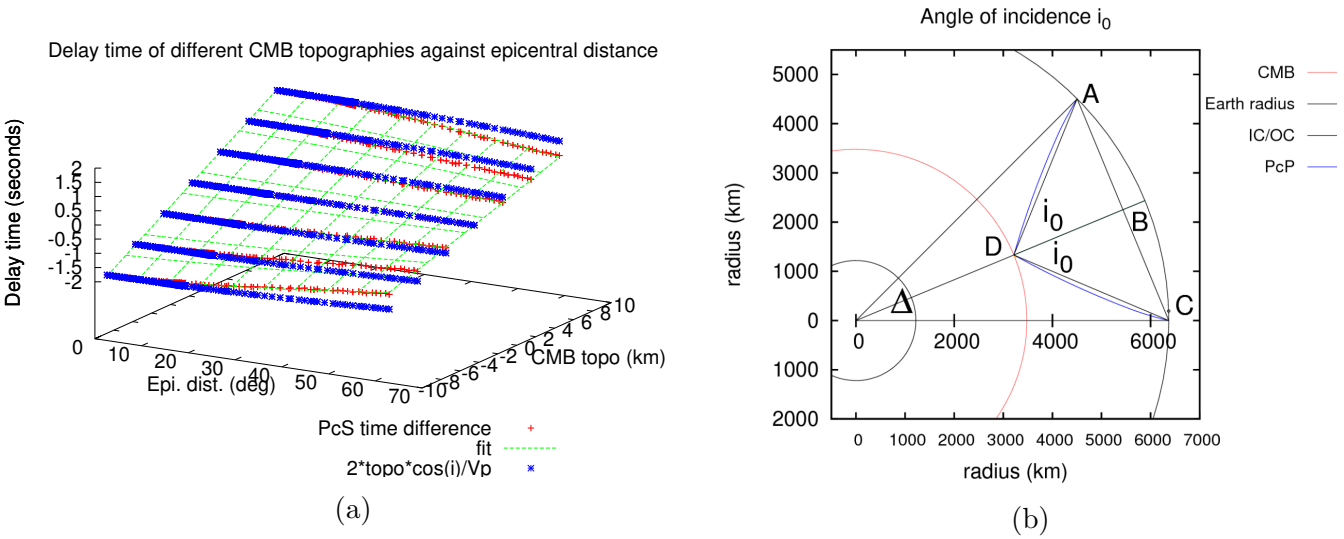

Figure 4: Figure 4a shows the delay time of the PcS phase as a function of CMB topography on one axis and epicentral distance on the other axis. The red datapoints were calculated by varying the height of the CMB in the PREM input model for TauP. The blue datapoints show the approximated time difference as calculated by $\delta t = 2h\cos(i)/v$. The green surface respresents a 2D 3rd order polynomial fit to the datapoints calculated using TauP. Figure 4b shows the geometry from which equation 2 was derived. The lenght $\|\mathrm{BC}\|$ is given by $\|\mathrm{BC}\| = \|\mathrm{0C}\|\sin\Delta/2$, where $\|\mathrm{0C}\| = R_e$. Length $\|\mathrm{BD}\|$ is given by the length of segment $\|\mathrm{0B}\| = R_e\cos(\Delta/2)$ minus the core radius $\|\mathrm{0D}\| = R_c$. The angle of incidence $\angle i$ is then given by the inverse tangent of $\|\mathrm{BC}\|$ over $\|\mathrm{BD}\|$.

2.3 SPECFEM3D

Synthetic seismograms are the source of information for this research. The seismograms were generated using SPECFEM3D_GLOBE version 5.1.5, a code which uses a spectral-element method to simulate elastic wave propagation in 3D Earth models (Komatitsch & Vilotte 1998). The waves that are simulated include finite frequency effects, which are neglected in ray theory. We generate waves for different Earth models with and without CMB topography. Comparing the seismograms then allows us to study the seismic response to this topography. As the basis input model, PREM (Dziewonski & Anderson 1981) was used. Simulations were made for the PREM model plus the CMB topography model of Li *et al.* (1991a) scaled to have peak-to-peak amplitudes of 8km and parametrized on spherical harmonic degree 0, 2 and 4. The topography model features two uplifted areas under Africa and the Pacific and is depressed under East Asia and America (Figure 5a). In order to study the independence of mantle heterogeneity and CMB topography, simulations were also made for PREM plus the S20RTS mantle model from Ritsema *et al.* (2004) and a for a combination of S20RTS and the CMB topography. Seismograms were then calculated for 2130 stations distributed equally over the globe, for four different 20km deep Earthquakes along the equator. The locations of the stations and earthquakes are shown in Figure 5b.

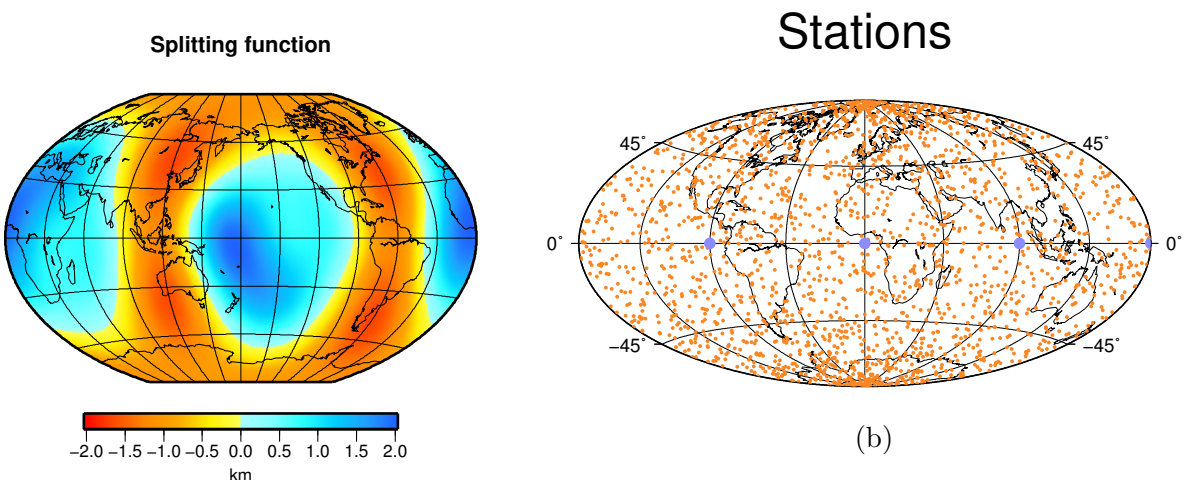

(a) (b)

Figure 5: a) CMB topography model by Li *et al.* (1991a) parametrized on spherical harmonic degree 0, 2 and 4. Although Li *et al.* predicted maximum topography of ±3 km, we scaled this to ±8 km in our study. b) Distribution of the 2130 stations over the globe (orange) and 4 earthquakes on the equator (blue).

2.3.1 Seismic sources

In order to obtain the best data for both P-waves and S-waves, two different sources were investigated: an explosive source with equal components along all three diagonal elements of the moment tensor, and a shear source with off-diagonal components only. The moment tensors are shown below. Although the shear source does produce P-waves, we expect a stronger P-wave signal from the explosive source. Therefore we will use the explosive source when studying the behaviour of P-waves and a shear source when studying S-waves.

$$M_{\text{explosive}} = M_0 \begin{bmatrix} 1 & 0 & 0 \\ 0 & 1 & 0 \\ 0 & 0 & 1 \end{bmatrix} \qquad M_{\text{shear}} = M_0 \begin{bmatrix} 0 & 1 & 0 \\ 1 & 0 & 0 \\ 0 & 0 & 0 \end{bmatrix}$$

2.3.2 Seismograms

For each seismic station, SPECFEM3D generates seismograms in the vertical, radial and transverse directions, from hereon referred to the Z-component, R-component and T-component of the seismogram. Two examples of a seismograms generated using SPECFEM3D are shown in Figure 6. The seismograms completely overlap, except at times for which the arrival time of an incoming phase is affected by the CMB topography. P-waves are only visible on the Z-component of the seismogram. S-waves are visible on both seismograms but are most explicit on the T and R-components of the seismogram. The R-component is similar to the T-component and is therefore not shown.

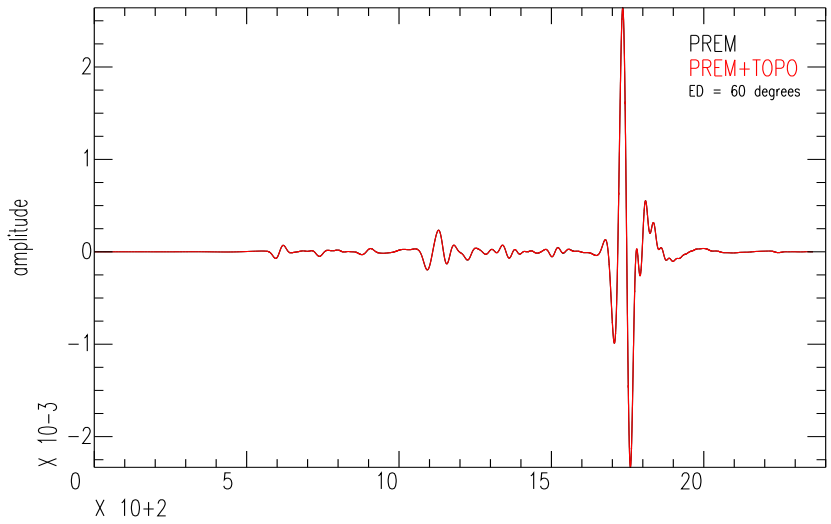

(a) Z-component

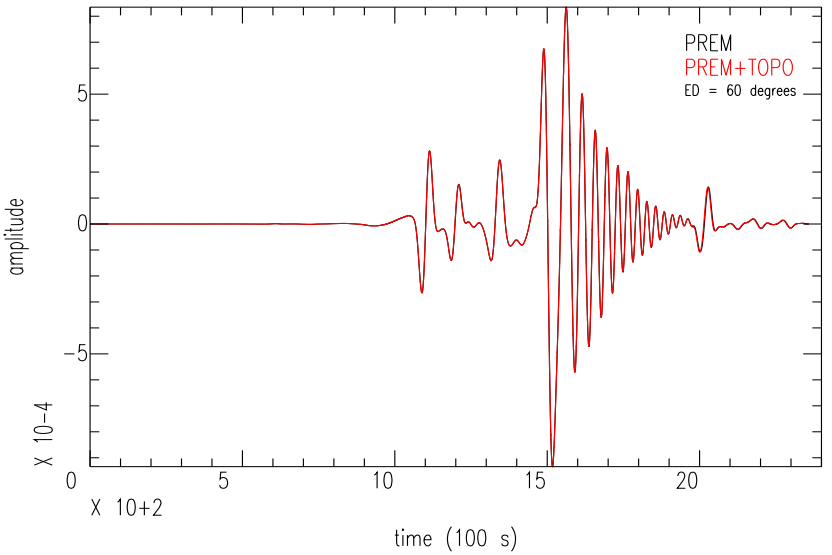

(b) T-component

Figure 6: Z-component (top) and T-component (bottom) of a seismogram measured by a station at an epicentral distance (ED) of 60° from a shear source. The black graph shows the seismograms for PREM and the red line shows the seismograms for PREM+TOPO. Some phases that can be identified in these seismograms are P at 605 s, ScS at 1195 s, SS at 1340s, SSS at 1527 s, ScSScS at 2016 s and the surface waves around 1700 s.

2.3.3 Cross-correlation

The presence of CMB topography may change the waveform of an incoming phase in different ways. Ray theory assumes that the shape of the waveform is conserved and that only the arrival time of the wavelet is affected. When this is the case, the time difference can be measured from the seismograms via cross-correlation. We apply cross-correlation on our data via the following steps: Firstly, the seismograms are detrended and filtered using a band pass filter with corner frequencies of $0.04\ s^{-1}$ and $0.4\ s^{-1}$. For a given phase, the expected arrival time at that epicentral

distance is calculated for PREM using TauP (Crotwell *et al.* 1999). A window of plus and minus 20 seconds is centered around the PREM arrival time. The time shift between the two seismograms that gives the highest correlation within the window is computed. If the correlation is less than 0.5 or if the time difference is larger than 20 seconds, the measurement is rejected. Otherwise, this difference in arrival time is recorded as $\delta t_{\text{measured}}$. For comparison, the CMB topography at the bouncepoint is also converted to a ray theoretical prediction according to the methods described in Section 2.2.

The bouncepoint is located at one half of the epicentral distance for symmetric single core reflections (PcP, ScS) and on one and three quarters for symmetric double reflections (PcPPcP, ScSScS). The coordinates of the bouncepoint of assymetric phases (ScP, PcS, ScSScP, ScPScP, ScPPcP) as a function of epicentral distance were calculated using TauP, as is shown in Figure 7b. The coordinates of the starting point and end of the path of the diffracted phases (Pdiff, Sdiff) along the CMB were calculated in a similar manner.

Figure 7a shows the T-component of the seismogram of Figure 6, windowed around the arrival of ScS. Comparing the two graphs with the naked eye, it is evident that the seismogram for PREM+TOPO is slightly delayed compared to PREM. However, it also shows that the shape of the seismogram is slightly altered due to the topography. Cross-correlation only takes into account the timeshift between waves that are sufficiently similar.

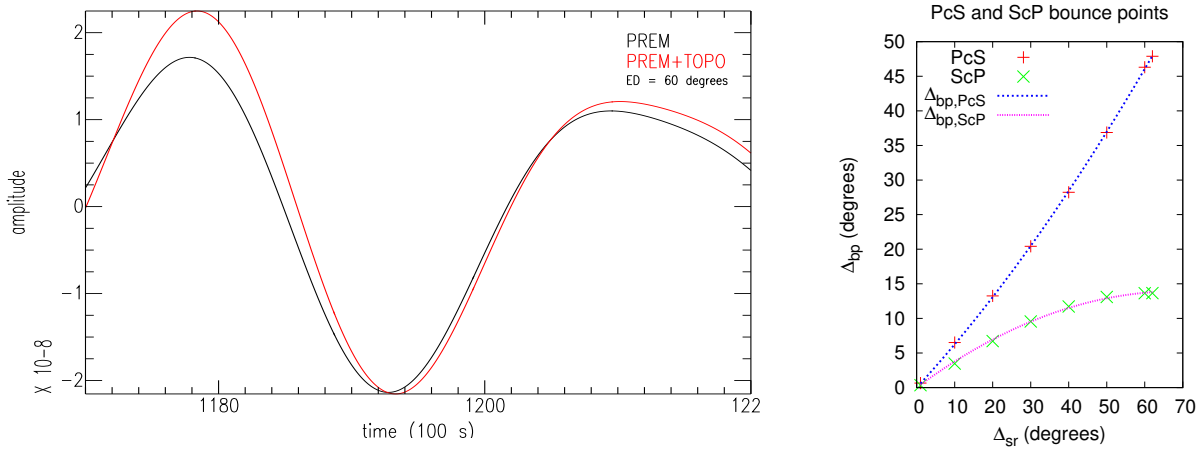

(a) (b)

Figure 7: Figure 1a shows the T-component of the seismogram at $\Delta = 60°$, centered around the predicted arrival of ScS. Figure 7b shows the dependence of the epicentral distance of the bouncepoint Δ_{bp} on the source-receiver epicentral distance Δ_{sr}. The fits yielded the following relationships: $\Delta_{bp,PcS} = 0.00284\Delta_{sr}^2 + 0.59736\Delta_{sr}$ and $\Delta_{bp,ScP} = -0.00297\Delta_{sr}^2 + 0.40647\Delta_{sr}$. Since ScS and PcP have symmetric wavepaths, their bouncepoints are simply given by $\Delta_{bp,ScS} = \Delta_{bp,PcP} = \frac{1}{2}\Delta_{sr}$

If the delay times measured from cross-correlation of synthetic seismograms are equal to the delay times predicted by ray theory, then ray theory provides a valid

description of the travel time delays due to CMB topography.

2.4 Linear decomposition of delay time

Another topic of interest is whether it is valid to linearly decompose the delays caused by CMB topography and delays due to heterogeneities in the mantle. In CMB topography reconstructions, it is often assumed that the total time difference δt_{total} between the arrival time observed in a seismogram $t_{\text{seismogram}}$ and the arrival time predicted by PREM t_{PREM} consists of two linearly independent contributions: One delay due to 3D mantle structure (e.g. S20RTS) and one delay due to CMB topography:

$$\delta t_{\text{total}} = t_{\text{seismogram}} - t_{\text{PREM}} \tag{3}$$

$$\delta t_{\text{total}} = \delta t_{\text{TOPO}} + \delta t_{\text{S20RTS}} \tag{4}$$

Under this assumption, it is possible to isolate the delay time due to CMB topography (δt_{TOPO}) by subtracting the delay times from the overlying mantle model (δt_{S20RTS}) from the total delay time difference obtained by substracting the 1D model (δt_{total}). The forward calculation of different combinations of Earth models by SPECFEM3D allows us to compare the combined effect of mantle heterogeneity and topography to the sum of their individual contributions measured from cross-correlation of the synthetic seismograms.

δt_{total} is found by measuring the arrival time difference between an Earth model with both mantle heterogeneity (S20RTS) and CMB topography, and the 1D model PREM: $\delta t^{[\text{S20RTS+TOPO}]-\text{PREM}}$. The individiual contribution of CMB topography to the total delay time is found by measuring the arrival time difference between two S20RTS Earth models, one with and one without CMB topography: $\delta t^{[\text{S20RTS+TOPO}]-\text{S20RTS}}$. The contribution of mantle heterogeneity to the total delay time is found by measuring the arrival time difference between the S20RTS Earth model and the 1D model PREM: $\delta t^{\text{S20RTS}-\text{PREM}}$.

The delay time due to the combined effects of mantle heterogeneity and CMB topography can now be compared to the two individual contributions. If the delays are linearly additive, the delay due to the combination of mantle heterogeneity and CMB topography should be equal to the sum of the individual delays. We now define the residual time $\delta t_{\text{residual}}$ as the difference between the combined delay and the two individual delays:

$$\delta t_{\text{residual}} = \delta t^{[\text{S20RTS+TOPO}]-\text{PREM}} - \delta t^{[\text{S20RTS+TOPO}]-\text{S20RTS}} - \delta t^{\text{S20RTS}-\text{PREM}} \tag{5}$$

If linear decomposition of mantle heterogeneities and topography is possible, then the first term on the right hand side will be equal to the second and third term. In that case $\delta t_{\text{residual}}$ equals zero. $\delta t_{\text{residual}}$ is computed for each source-receiver couple for all phases studied.

3 Results

To gain a general idea of the way that CMB topography affects the full-waveform synthetic seismograms generated by SPECFEM3D, we first present a series of individual seismograms in section 3.1. In the result sections that follow, we compare the travel time delays predicted from ray theory to the delays measured from cross-correlation for single and double core reflections. We also present the residual times for each phase, which rule out whether CMB topography and mantle heterogeneity are linearly additive. In a similar manner, we compare input CMB topography to delays measured from cross-correlation of the diffracted phases and study their linear decomposition in section 3.4. To gain an insight in the variability of the relationship between ray theoretically predicted delays and delays measured from cross-correlation as a function of epicentral distance, the ScS phase is analysed at 10° intervals in section 3.5. In section 2.2, two methods to calculate CMB topography were presented. In result section 3.6 we compare the conclusions drawn from the two methods.

3.1 Seismograms

Figures 8a to 9b give an overview of the seismograms that were calculated for the PREM model and the PREM+TOPO model using SPECFEM3D. If the incoming phases are unaffected by the CMB topography, the two seismograms overlap. If the arrival time of a phase is affected by CMB topography, the seismogram of PREM becomes visible around the arrival time of that phase. The most pronounced feature in each seismogram is the surface wave (at 200 s in Figure 8a, at 1200 s in Figure 8b). The waveform of the surface wave is unaffected by CMB topography. Therefore, when we subtract the PREM seismogram from the PREM+TOPO seismogram, the surface wave disappears while the differences between waveforms of phases that are affected by CMB topography are emphasised (bottom figures).

Figures 8a to 9b show the Z-component of seismograms created by an explosive source, travelling in an attenuated medium. As demonstrated in Appendix A, attenuation does not strongly affect cross-correlation measurements of P-waves. Therefore we are able to combine the data from the attenuated explosive source and the nonattenuated shear source. At small angles, subtracting one seismogram from the other reveals differences in arrival time for PcP, ScP, ScS, ScPScP, ScSScP. As the epicentral distance increases towards 40° (Figure 8b), the differences of arrival time of the double reflections ScPPcP, ScPScP and ScSScP become more explicit, while the difference between the seismograms near the PcPPcP arrivals is relatively small. At epicentral distances beyond 100°, the angle of incidence of the P-waves and S-waves onto the CMB is so large that they are diffracted in stead of reflected. The bottom graphs of Figures 9a and 9b show that besides the double reflections, Pdiff is also affected by CMB topography. Moreover, the seismograms beyond $\Delta = 100°$ show several additional peaks. Two of them can be attributed to PKKP and PKiKP, but the identification of other phases is more difficult because different waveforms overlap. The long period of the waveforms follows from the limited computational resolution of SPECFEM3D.

Figures 10a till 11b present the main features of the T-component of seismograms created by a shear source. At small epicentral distances (Figure 10a), the surface wave has the highest amplitude, but when subtracting the PREM seismogram from the PREM+TOPO seismogram, clear differences in the waveforms of ScS and ScSScS become visible. As can be seen in the travel time curve of Figure 3, ScS and the surface waves arrive simultainiously at an epicentral distance of 40°. Although the bottom seismogram of Figure 10b still reveals a difference between ScS waveforms of PREM and PREM+TOPO, cross-correlation may be unsuccesful due to the interference with the surface wave. Beyond 100°, Sdiff replaces ScS. This phase is also sensitive to CMB topography.

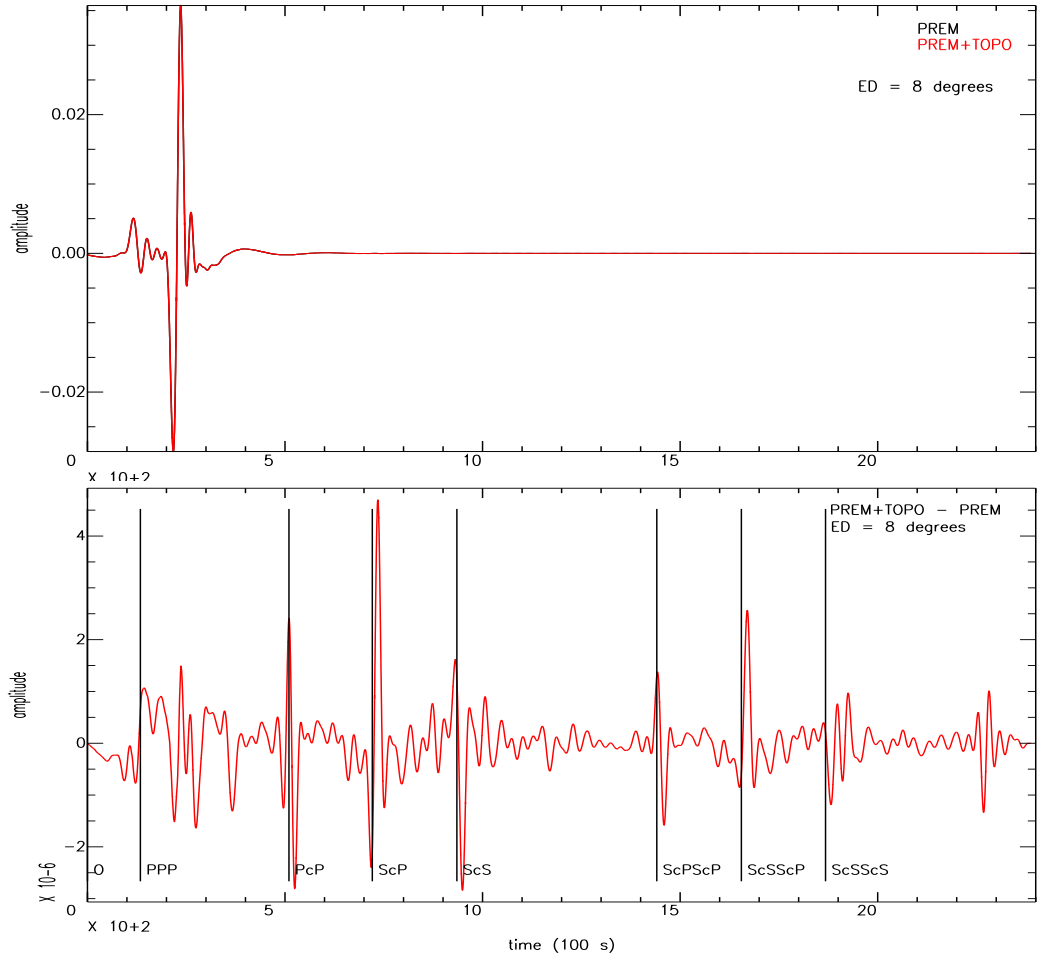

(a) $\Delta = 8°$

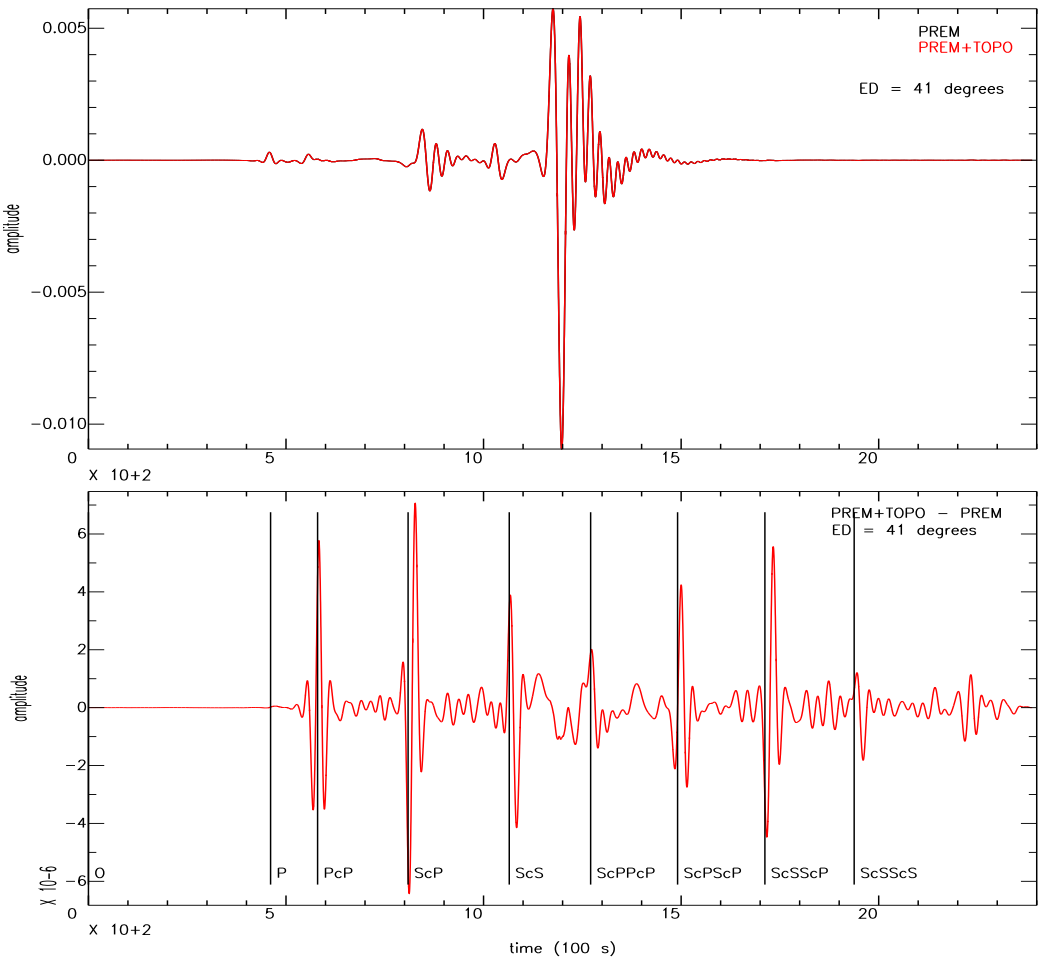

(b) $\Delta = 41°$

Figure 8: The top graph of Figure 8a shows the Z-component of two synthetic seismograms calculated for an explosive source in an attenuated medium at an epicentral distance of 8°. PREM is plotted in black and PREM+TOPO is plotted in red. The bottom graph shows the difference between the two seismograms as a function of time. Note that the scale of the amplitude decreases by several orders of magnitude. The labels show arrival time of phases as predicted by PREM. Figure 8b shows the same figure for an epicentral distance of = 41°. The surface wave at 1200s has the highest amplitude but other phases become visible on the seismogram too. Subtracting one seismogram from the other reveals significant differences in arrival time for PcP, ScP, ScS ScPScP and ScSScP.

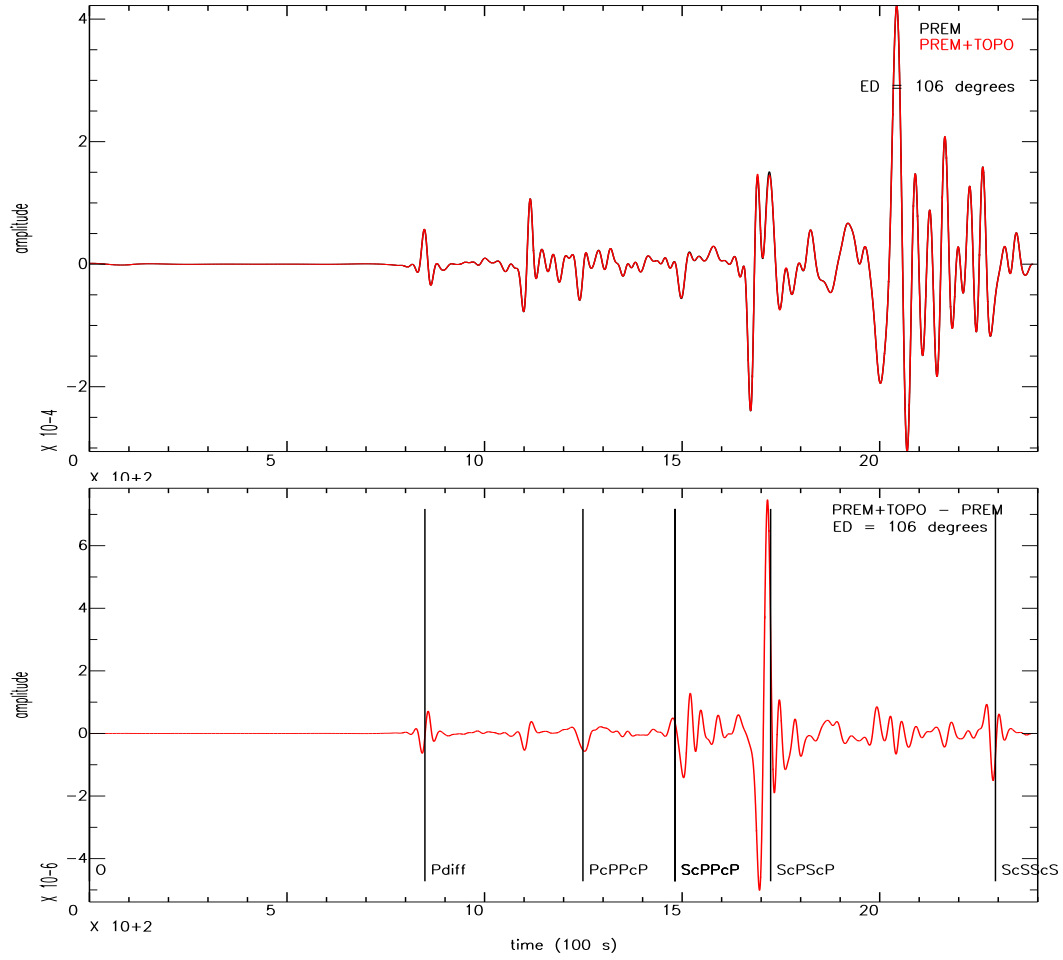

(a) $\Delta = 105°$

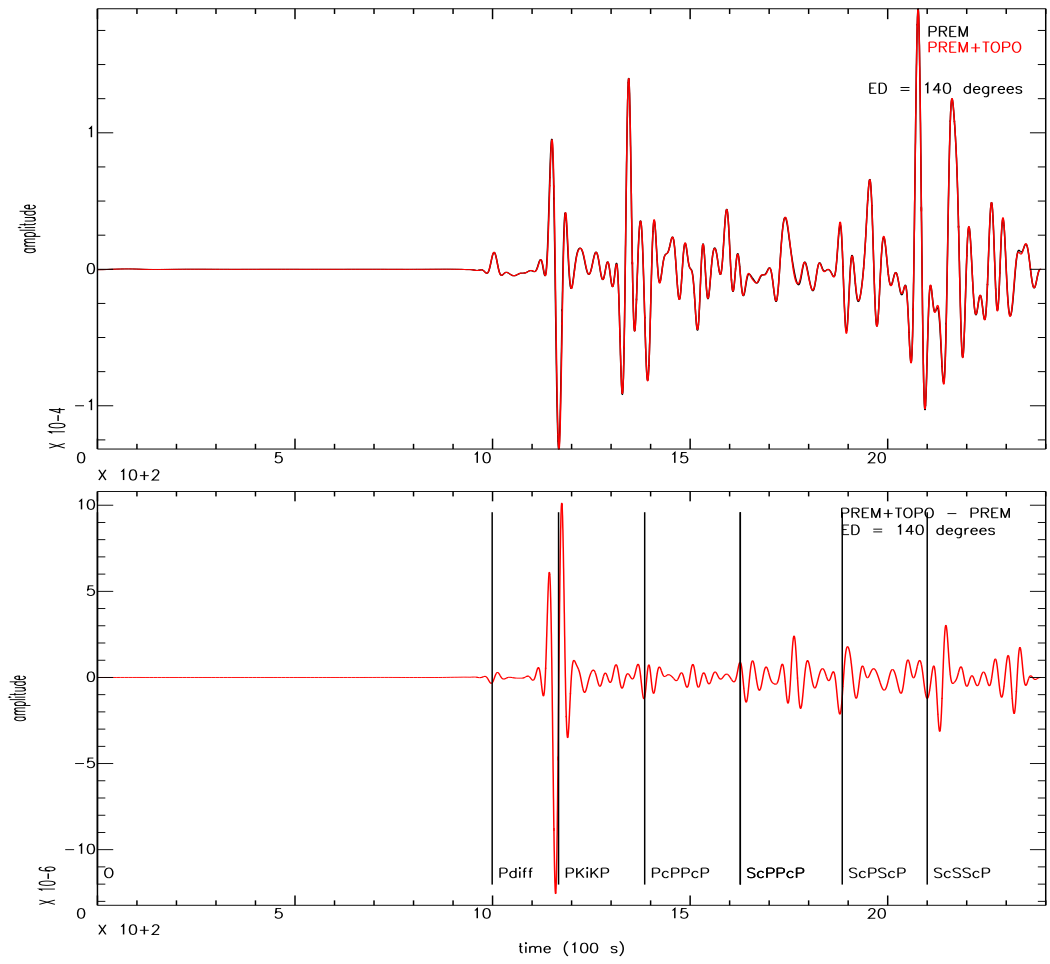

(b) $\Delta = 140°$

Figure 9: Figure 9a is the same as Figure 8a but for an epicentral distance of 106°. At this distance, Pdiff is measured in stead of PcP. Arrival times of Pdiff, ScPPcP, ScP-ScP, and ScSScS show small time differences between the two seismograms. The largest difference is measured at 1700s. Although this peak occurs close to the arrival time of ScP-ScP, it also corresponds to the arrival time of PKKP. Figure 9b is the same figure but for an epicentral distance of 140°. At this distance, many different phases are detected by the receiver. In the bottom graph, Pdiff and the double reflections do not stand out as much as at smaller epicentral distances. However, there is a peak that corresponds to the PREM arrival time of PKiKP.

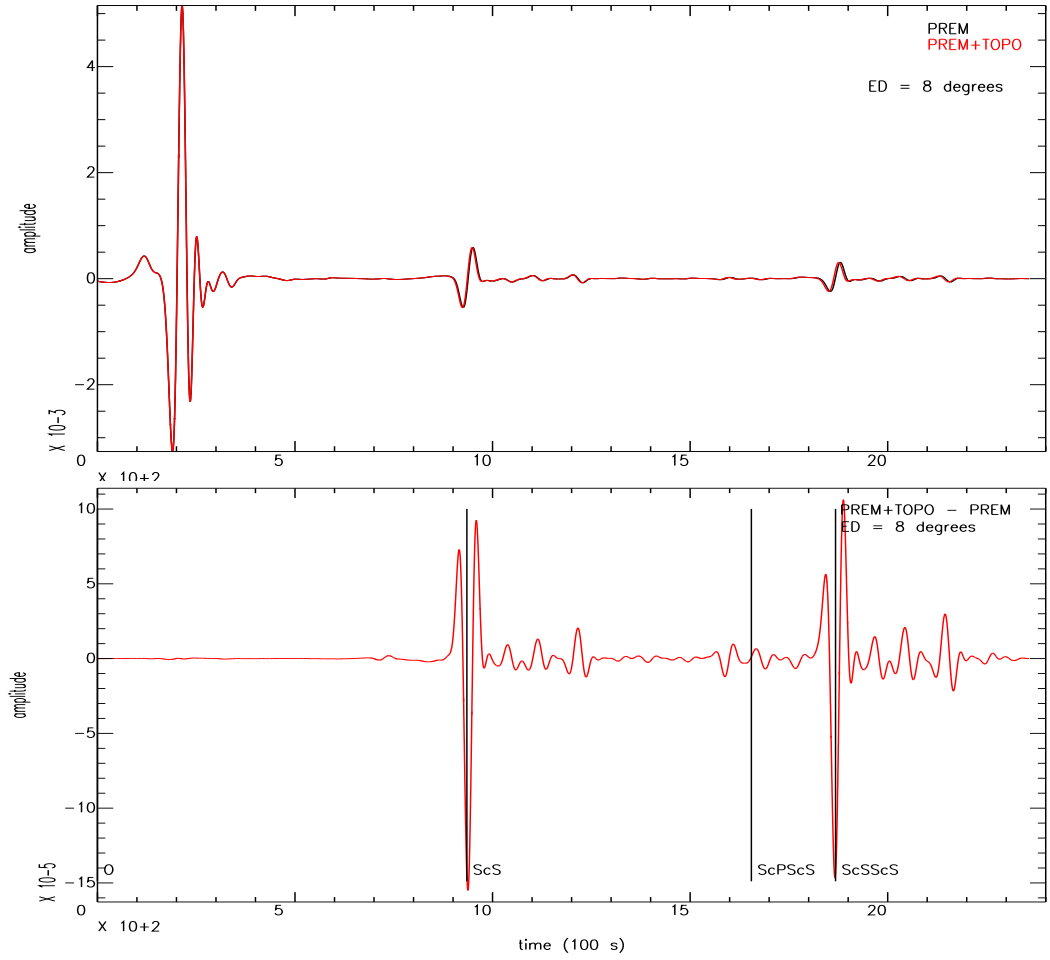

(a) $\Delta = 8°$

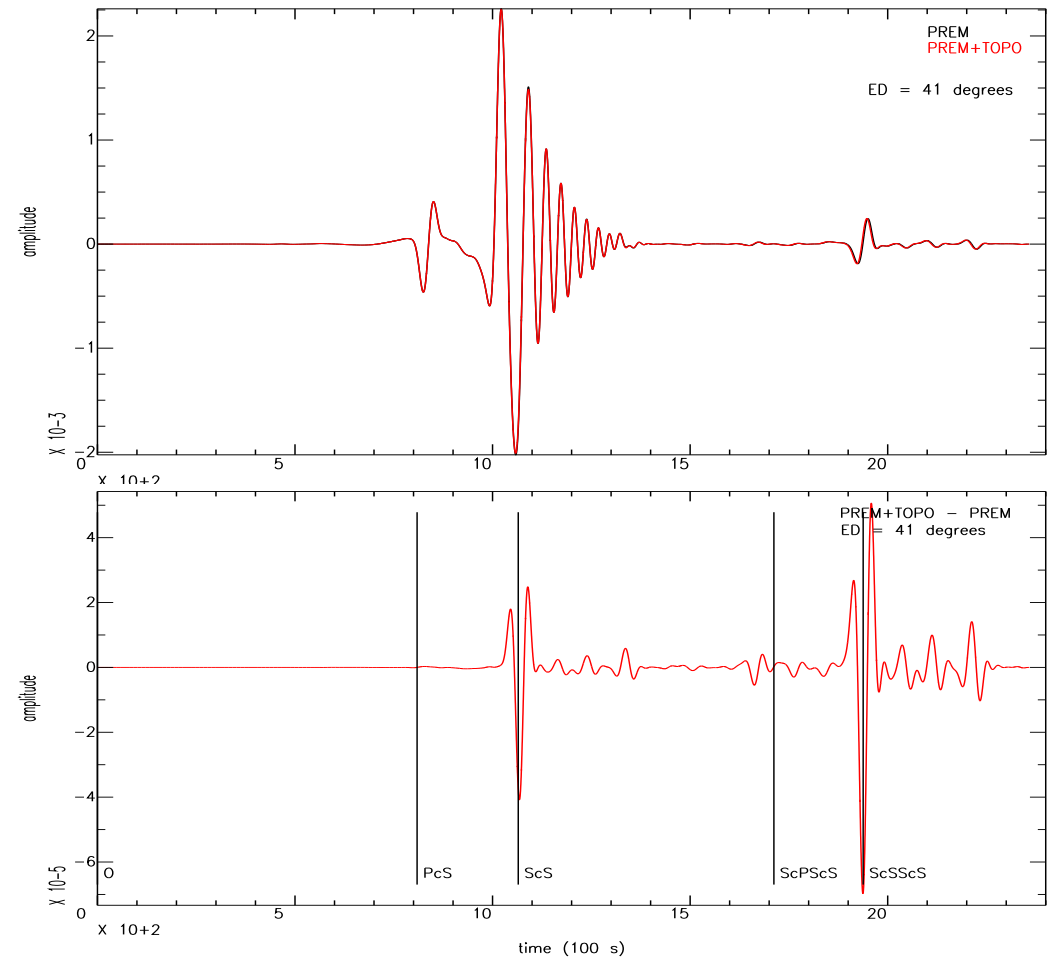

(b) $\Delta = 41°$

Figure 10: Similar to Figure 8a, but for the T-components of seismograms created by a shear source. The epicentral distance of the receiver is 8°. The most explicit phase in both seismograms is the surface wave which arrives after 200s. ScS and ScSScS are also visible on the seismogram. The bottom graph shows that these phases were affected by CMB topography. Note how smaller phases precede and follow these phases at intervals of approximately 100s. Similar to Figure 10a, but for an epicentral distance of 41°. Even though the surface wave interferes with ScS at this epicentral distance, the effect of CMB topography is still evident when one of the seismograms is subtracted from the other.

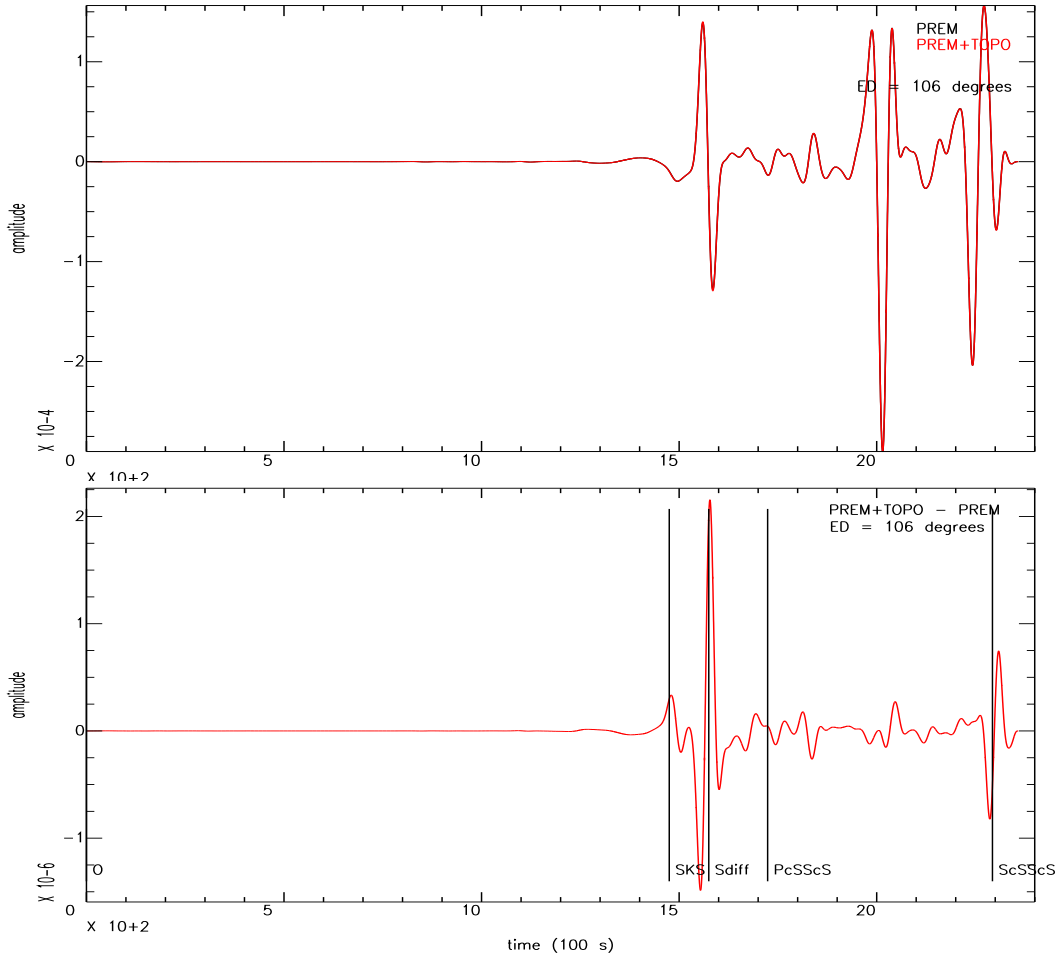

(a) $\Delta = 105°$

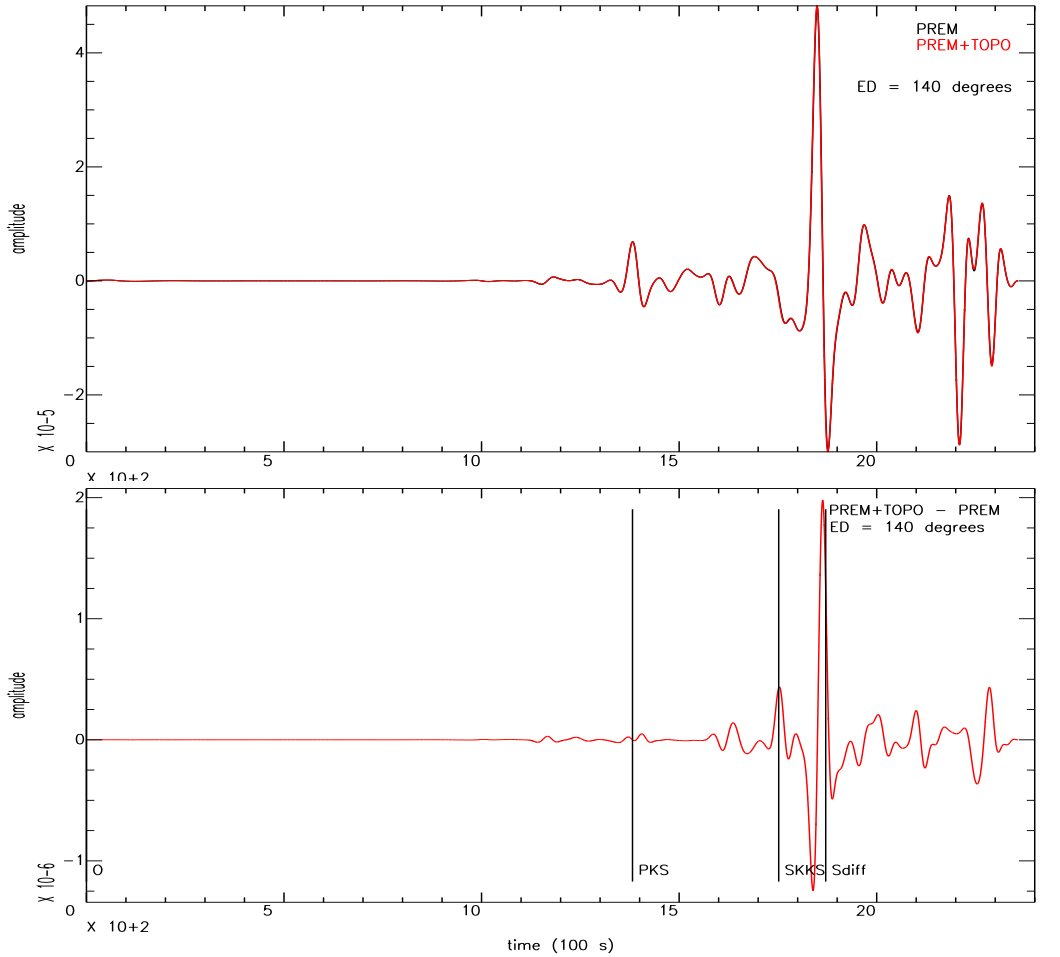

(b) $\Delta = 140°$

Figure 11: Figure 11a is the same as Figure 10a, but for an epicentral distance of 106°. At this angle, Sdiff is measured in stead of ScS. ScSScS is still visible but will soon be beyond the length for which the seismogram was calculated (2400 s). Figure 11b is the same, but for an epicentral distance of 140°. Sdiff is the only identified phase that is affected by CMB topography.

3.2 Single reflections

In this section, we compare the delay times that are predicted by ray theory, from hereon referred to as $\delta t_{\text{theoretical}}$ or *predicted delays*, to the time difference measured from cross-correlation of synthetic seismograms with and without CMB topography, from hereon referred to as $\delta t_{\text{measured}}$, δt_{cc} or *measured delays*. If ray theory correctly predicts the delays due to CMB topography, the predictions should match delays measured from cross-correlation of the full-waveform synthetic seismograms. If we measure different or no delays, then CMB topography does not affect the arrival time of the phase as predicted by ray theory. In the following subsections we compare the theoretical predictions from ray theory for ScS, ScP and PcP are compared to cross-correlation measurements of delays from the synthetic seismograms. PcS is not shown because its signal was too weak to perform a proper cross-correlation.

3.2.1 Maps

The maps in Figures 12 to 14 give an overview of the differences and similarities between ray theoretical predictions and measured delays of ScS, ScP and PcP. The locations of the dots represent bouncepoints, the colours of the dots represent the corresponding predicted delays (right figure) or measured delays (left figure). Where the left and right figure are the same, ray theory correctly predicts the delays due to CMB topography. Where the dots in the right figure have fainter colours than in the left figure, the time difference is smaller than the ray theoretical prediction.

All three figures show that the pattern predicted by ray theory reoccurs in the measurements to some extent. However for ScS, cross-correlation does not reproduce the predicted delays for bouncepoints between 15 and 25 degrees from the source and beyond 35 degrees from the source, corresponding to source-receiver epicentral distances of 30 to 50 degrees and 70 degrees respectively. From the travel time curve in Figure 3 we see that the epicentral distances of these gaps coincide with epicentral distances where the surface waves and the S wave interfere with ScS. For PcP, delays are solely measured in concentric rings of bouncepoints at epicentral distances of 10 to 15 degrees and and 20 to 25 degrees, corresponding to source-receiver distances of 20-30 degrees and 40-50 degrees. According to the travel time curve for PREM, interference with the surface waves is expected near epicentral distances of 15 to 20 degrees and and interference with PP and PPP happens around $\Delta = 40°$. Figure 2b tells us that at epicentral distances of less than 20 degrees, most of the energy of the P-wave incident to the CMB is transmitted into the core rather than reflected in the form of PcP. Roughly everywhere where cross-correlations are measured, ray theory predicted the sign of the delay correctly. However, the difference in colour intensity suggests that ray theory overestimates the magnitude of the delay.

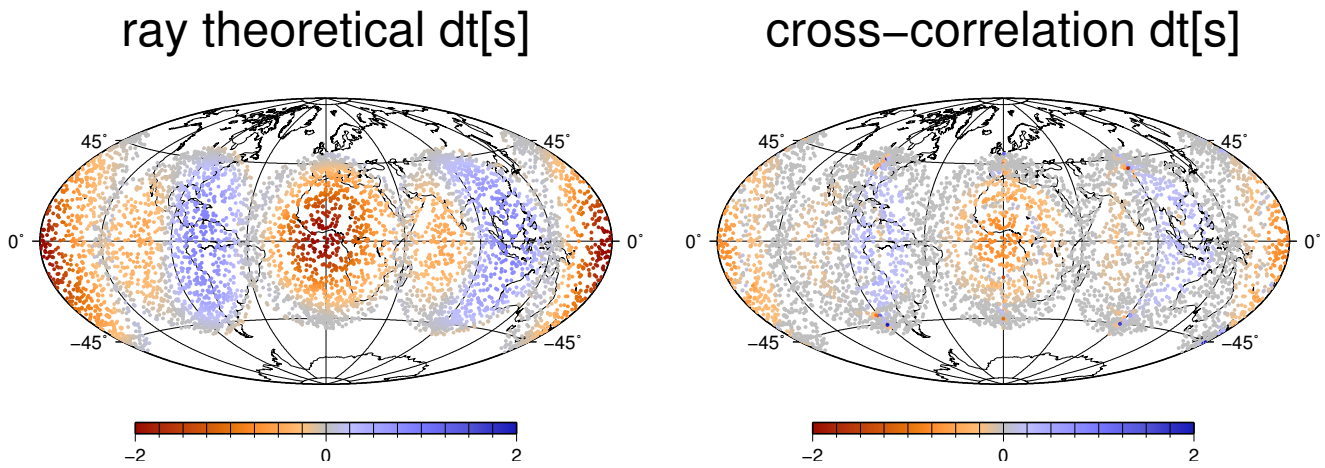

Figure 12: Each point on these maps corresponds to the location of a bouncepoint between a source and a receiver. The colour of the dot indicates the difference in arrival time of the ScS phase for T-compontents of seismograms generated with the input model PREM and the input model PREM+TOPO for a shear source. The left figure shows the ray theoretical time delay, calculated from the topography at the bouncepoint. The left figure shows the time differences that were measured from cross-correlation of seismograms with and without topography. Grey dots indicate that no time difference was predicted by ray theory or measured by cross-correlation of the seismograms.

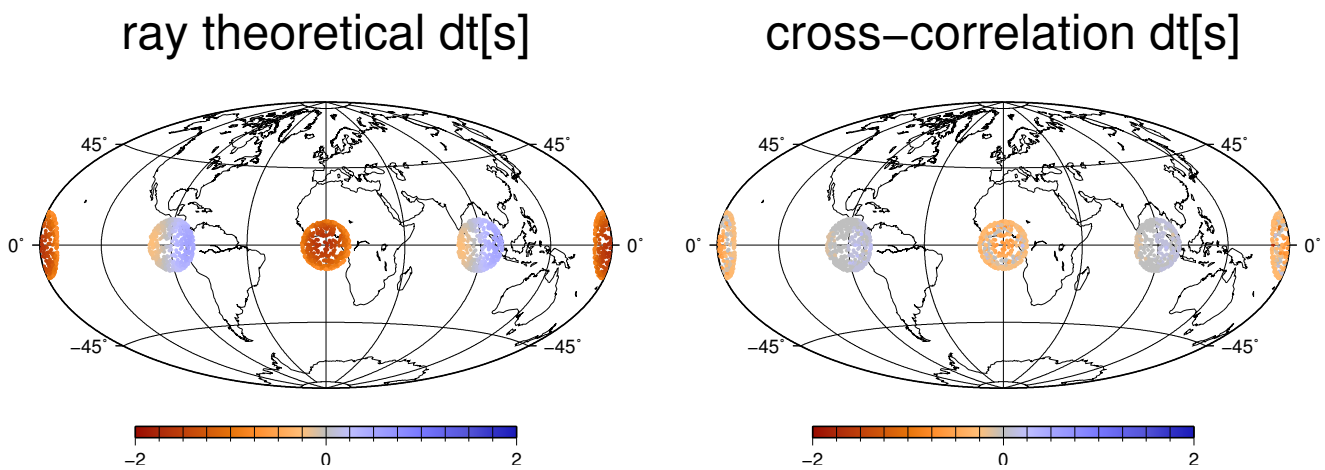

Figure 13: Similar to Figure 12, but for ScP. The bouncepoints of ScP are located closer to the source than the receiver. Therefore the a more concentrated area is sampled by this phase. The Z-component of seismograms generated by a shear source were used for the cross-correlation.

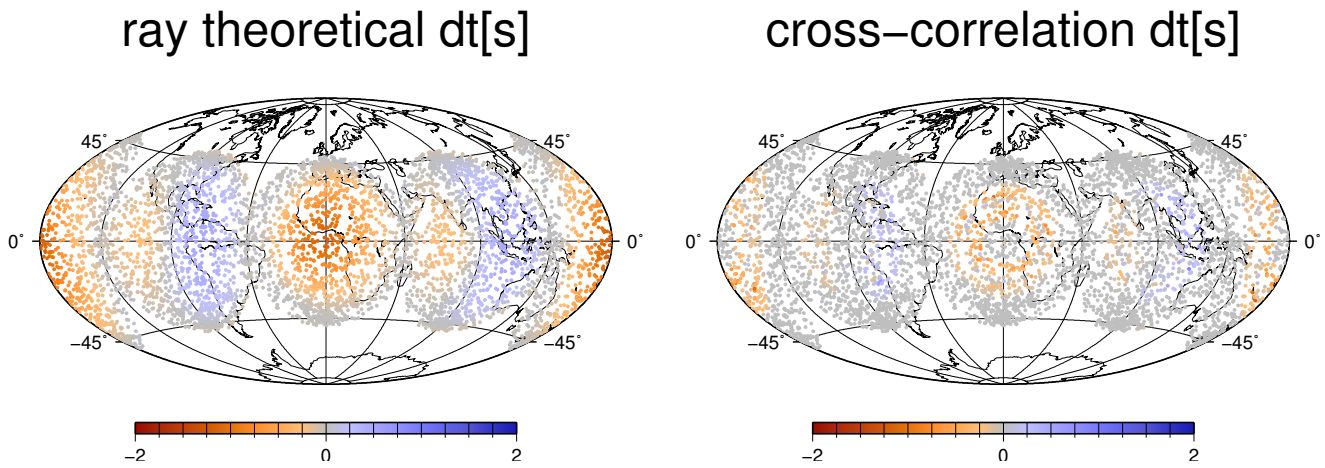

Figure 14: Similar to Figure 12, but for PcP. The Z-component of seismograms generated by an attenuated explosive source were used for the cross-correlation.

3.2.2 Scatter plots

Replotting the datapoints from Figures 12 to 14 in the form of scatter plots gives a more detailed impression of relationship between the delays predicted from ray theory and delays measured from cross-correlation of full waveform synthetic seismograms. Figure 15 shows scatter plots of predicted against measured delays for ScS, ScP and PcP. If ray theory correctly predicts both the sign and the magnitude of the delays caused by the CMB topography, these points should align along a slope of 45 degrees. A slope steeper than 45 degrees indicates that measurements from cross-correlations on average give a smaller amplitude than is predicted by ray theory. Although the datapoints are not perfectly aligned, all three scatter plots show a positive trend. In general, measured time delays have the same sign but a smaller magnitude than the ray theoretical predictions. More specifically, the linear relationships between cross-correlation measurements and ray theoretical delays are 1:1.4 for ScS, 1:2.5 for ScP and 1:1.3 for PcP. However, the spread of the datapoints tells us that there are many exceptions to these trends. The gap in the data of ScP that is seen in Figure 15b is due to the fact that bouncepoints of ScP are sampled in two areas of elevated topography and two separate areas of depressed topography. This is also evident from Figure 13.

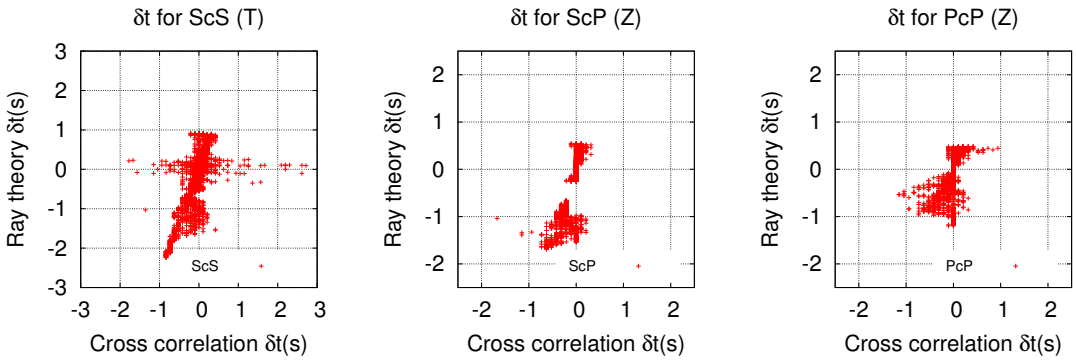

(a) (b) (c)

Figure 15: These figures show the the ray theoretical delay times of ScS, ScP and PcP of each station plotted against the values measured from-cross correlation. Using linear regression we found that the relationship between cross-correlation measurements and ray theoretical predictions is 1:1.4 for ScS, 1:2.5 for ScP and 1:1.3 for PcP.

3.2.3 Histograms

The histograms below help to visualise the errors in the ray theoretical predictions. We define the ray theoretical error of a datapoint as the difference between the delay measured from cross-correlation and the delay predicted by ray theory. If the ray theoretical predictions are equal or close to the delays measured from cross-correlation, the errors should be distributed closely around zero in the histrograms in Figure 16. To compare the relative magnitude of the errors to the magnitude of the delay time measurements, the cross-correlation measurements are also shown in the histogram. Comparing the widths of the distributions of the errors and the measurements tells us whether the errors in the ray theoretical preditions are in general small compared to the magnitude of the measurements or whether the size of the errors in the predictions are comparable to or larger than the measurements. All three histograms in Figure 16 show that the spread in the data errors is comparable to (16a) or wider than (16b, 16c) the data from cross-correlation. This tells us that there is a significant chance that a ray theoretical prediction is off in the order of its own magnitude. In all three cases the error is biased towards positive values. This could be due to phases that were predicted to arrive earlier than they were measured, or due to delays that were measured to be larger than the theoretical predictions (in absolute sense). A comparison with Figures 12 to 14 suggests that the former is the case. The statistics do not tell whether this bias is due to a weaker response of arrival times to depressed topography or whether simply less bouncepoints were sampled from these regions.

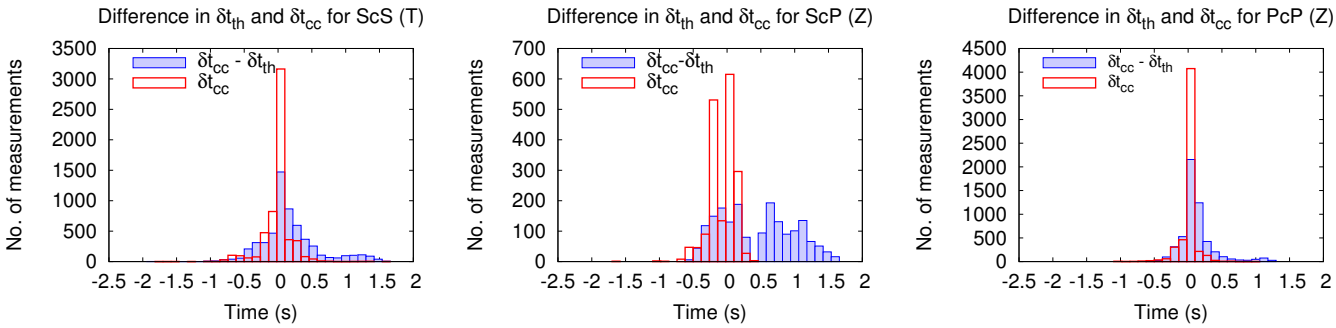

(a) (b) (c)

Figure 16: These figures show histograms for ScS, ScP and PcP with two different distributions plotted for each phase. The blue opaque boxes show the difference in measured and predicted arrival time, δt_{cc} and δt_{th}. The red opaque boxes show the distribution of the data from cross-correlation (δt_{cc}). Comparing the widths of these distributions tells us whether the errors of the ray theoretical preditions are in general small compared to the magnitude of the measurements (blue narrow compared to red) or whether the size of the errors in the predictions are comparable to or larger than the measurements (red narrower than blue). Moreover a symmetric distribution of $\delta t_{\mathrm{cc}} - \delta t_{\mathrm{th}}$ centered around zero suggests that data errors are random whereas assymmetry and bimodality suggest the presence of underlying systematic effects.

3.2.4 Linear decomposition

As was discussed in section 2.4, models of CMB topography made using body waves are built on the assumption that mantle heterogeneity and CMB topography are linearly additive. If this assumption is valid, then predictions for mantle structure can simply be subtracted from the wavefield to obtain the delay times due to CMB topography only. We generated synthetic seismograms for all combinations of PREM, S20RTS and CMB topography that are necessary to compute the right hand side of equation 5, which gives us $\delta t_{\mathrm{residual}}$. If linear decomposition of mantle heterogeneity and CMB topography is possible, $\delta t_{\mathrm{residual}}$ should be equal or close to zero. The histograms in Figure 17 allow us to compare the distribution of $\delta t_{\mathrm{residual}}$ to the distribution of the delays from cross-correlation measurements ($\delta t^{[\mathrm{S20RTS+TOPO}]-\mathrm{PREM}}$). For all three phases, the combined effect of mantle heterogeneity and CMB topography adds up to the same travel time as the sum of the two individual travel times. Comparing the spread of $\delta t_{\mathrm{residual}}$ to the spread of the delays from cross-correlation measurements, we see that the errors in the delays introduced by approaching mantle heterogeneity and CMB topography as separate contributions, are small compared to the delays due to CMB topography itself.

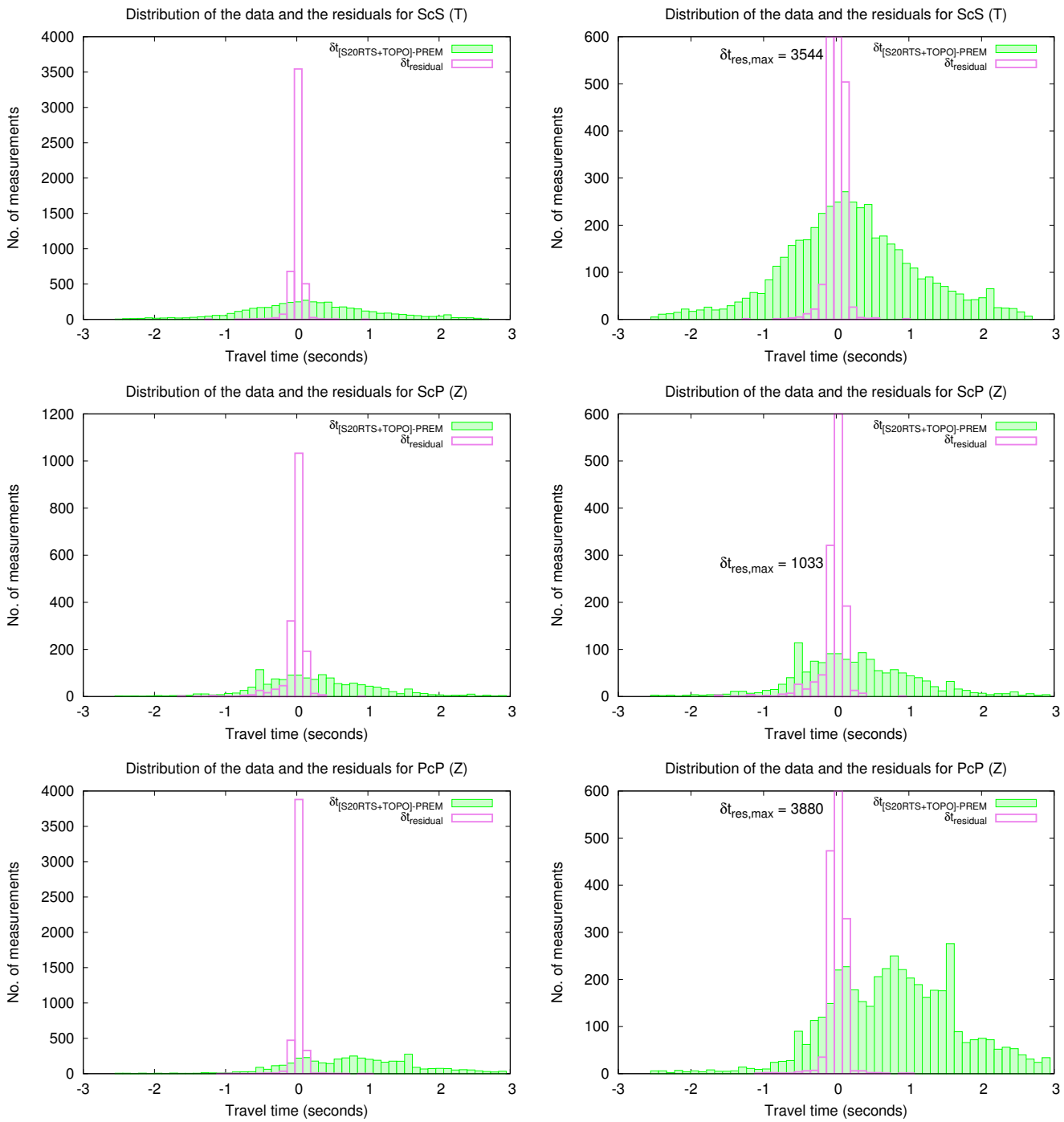

Figure 17: These historgams show the distributions of $\delta t_{\text{residual}}$ (violet) for ScS, ScP and PcP. $\delta t_{\text{residual}}$ was defined in equation 5. In case that the individual effects of mantle heterogeneity and CMB topography add up to the combined effect of the two parameters, $\delta t_{\text{residual}}$ will be zero and the two effects are said to be linearly additive. The time differences measured by cross-correlation of [S20RTS+TOPO] and [PREM] are shown on the background of each histogram in green to give an idea of the relative width of the spread in $\delta t_{\text{residual}}$ compared to the data. The figures on the right are zoomed in on the lower part of the Y-axis of the figures on the left.

3.3 Double reflections

Next, we compare the ray theoretical predictions of the delays to the delays measured from cross-correlation of full waveform synthetic seismograms for the phases ScSScS, ScSScP, ScPScP, ScPPcP and PcPPcP, as well as the linear additivity of mantle heterogeneity and CMB topography for these phases. As was explained in section 2.1, the delay time measured by the receiver consists of two contributions which we assume to be equal in both our theoretical estimates and our measurements from cross-correlation. Note that these ray theoretical estimates for delays will contain errors compared to the input model because we predict delays for unknown contributions of the bouncepoints.

3.3.1 Maps

The maps in Figures 18 and 19 plot the predicted and measured delays of each source-receiver couple at the locations of the two bouncepoints that caused the delay. The figures on the left show the ray theoretical predictions. Our assumption of equal contribution of each bouncepoint causes opposite contributions to cancel out. This is visible in Figure 18a. There is a grey shadow on the western side of the uplifted area around 0 latitude, 0 longitude. From the input model (Figure 5a) we know that the bouncepoints in this grey shadow are in fact located on uplifted topography. However, extrapolating the distance from the source at (0,0) to the first bouncepoint, we find that the second bouncepoint is located on depressed topography. The predicted delay is the sum of the contributions of the two bouncepoints, which cancel. This explains why our method leads to ray theoretical predictions that are not identical to the input model.

If ray theory correctly predicts the signs and amplitudes of the delays, the panels from full-waveform cross-correlation (right column) should be equal to panels on the left of Figure 18 and 19. The figures from full waveform cross-correlation show more grey dots than the figures of ray theorical predictions. This reveals that CMB topography in many cases does not introduce the delays predicted by ray theory. The panels of phases with more P-branches (PcPPcP, ScPPcP) show more grey dots than the figures with more S-branches (ScSScS, ScSScP). This suggests that there is a stronger signal for S-waves than for P-waves. A second observation is that where delays are measured from cross-correlation, the sign matches the ray theoretical prediction.

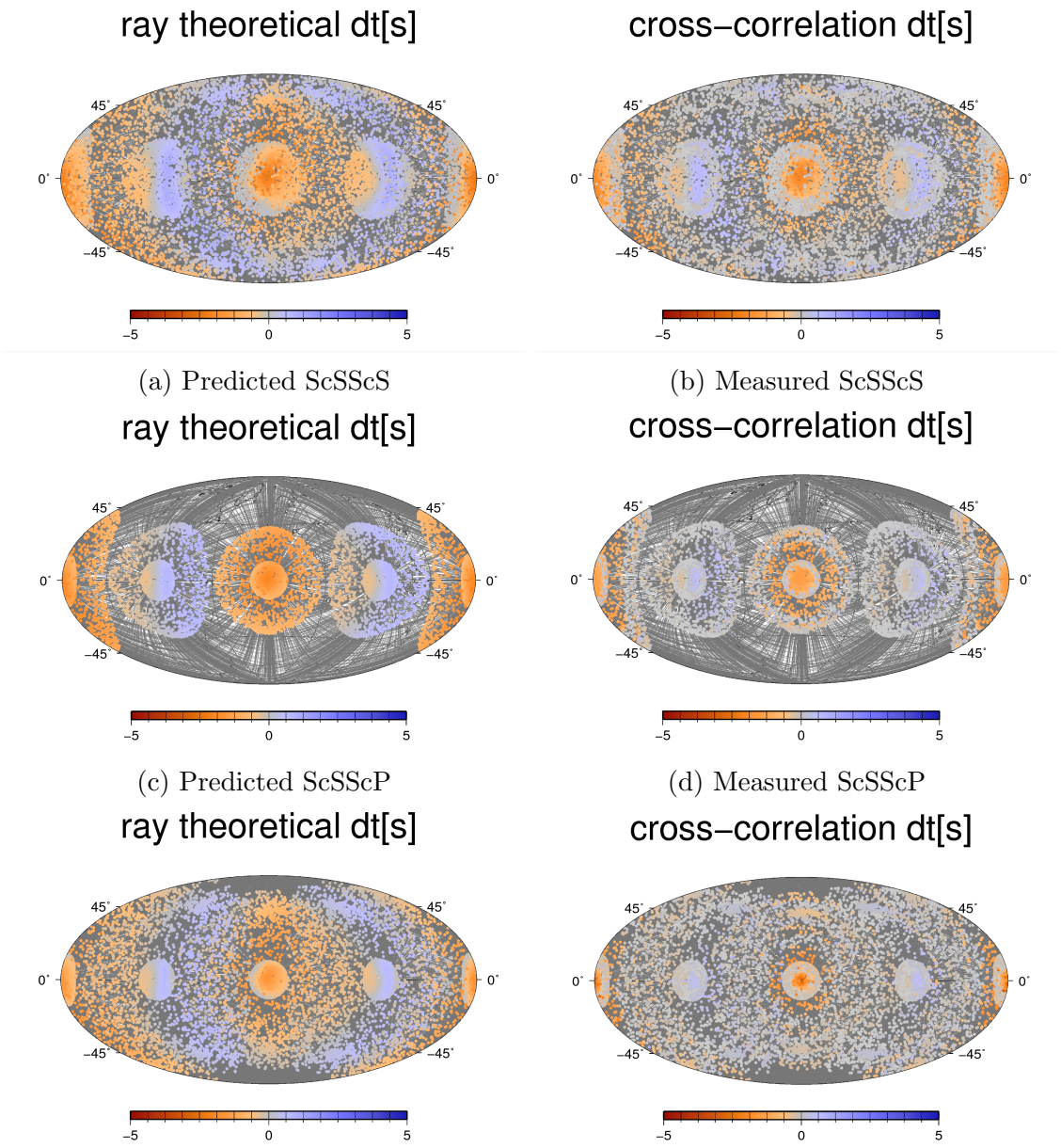

(a) Predicted ScSScS

(b) Measured ScSScS

(c) Predicted ScSScP

(d) Measured ScSScP

(e) Predicted ScPScP

(f) Measured ScPScP

Figure 18: Ray theoretical arrival time difference (left) and and time difference measured from cross-correlation for ScSScS (top), ScSScP (middle) and ScPScP (bottom). In the maps, two dots are plotted along each arclenght from source to receiver. The locations of the dots correspond to the latitude and longitude of two bouncepoint on the CMB. For ScSScS and PcPPcP these bouncepoints are located exactly on one-fourth and three-fourth of the arclength. The bouncepoints of phases with both P and S segments are slightly assymetric, depending on the configuration of the P and S segments. As the two bouncepoints contribute to one total time difference measured at the receiver, the individual contributions cannot be resolved from the seismograms. Under the assumption that the two contributions from CMB interactions are equal, the theoretically observable difference in arrival time is found by dividing the total time delay predicted from ray theory according to the known topography at the bouncepoints, by two. Similarly, the delay times measured from cross-correlations are displayed assuming two equal contributions from each bounce point.

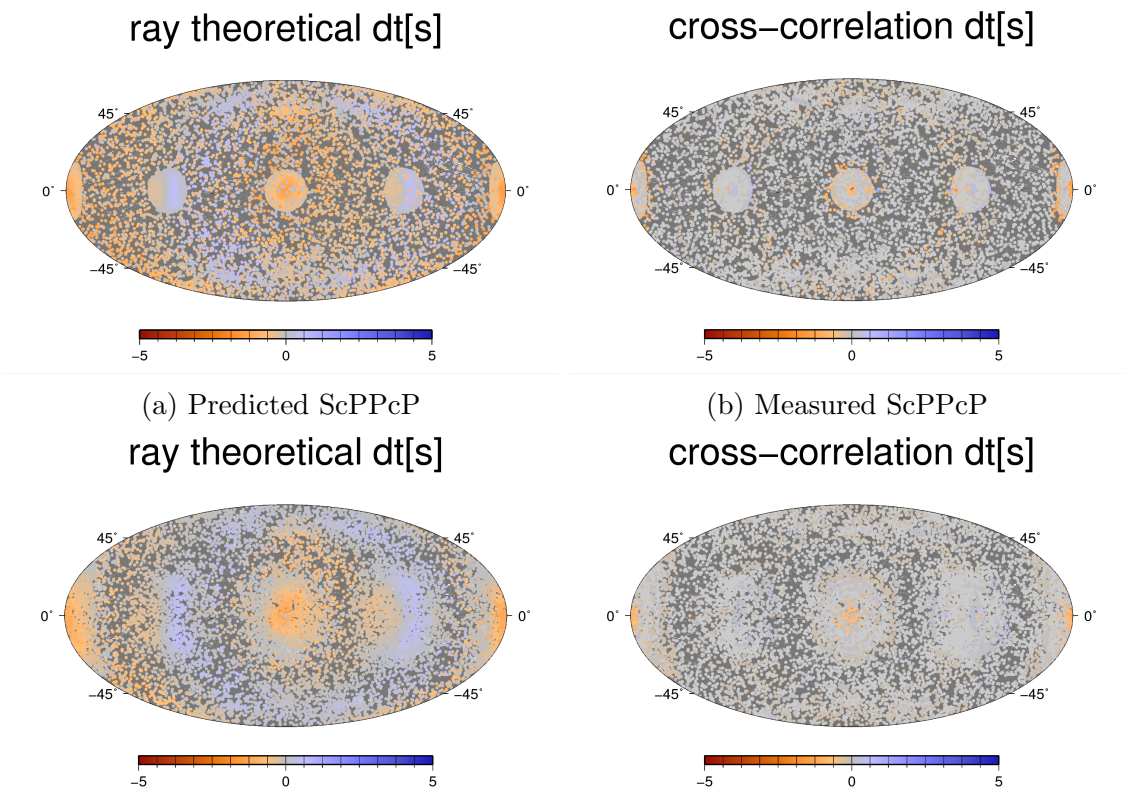

(a) Predicted ScPPcP

(b) Measured ScPPcP

(c) Predicted PcPPcP

(d) Measured PcPPcP

Figure 19: Ray theoretical arrival time difference (left) and and time difference measured from cross-correlation of Z-component for ScPPcP (top) and Z-component for PcPPcP (bottom)

3.3.2 Scatter plots

Replotting the datapoints from Figure 18 and 19 in the form of scatter plots confirms that no delays are measured from cross-correlation in many of the stations for which delays are predicted from ray theory. Meanwhile, if a delay is measured from cross-correlation, it usually has the same sign as the delay predicted from ray theory. Using linear regression, we find that the relationships between cross-correlation measurements and ray theoretical delays are 1:1.14 for ScSScS, 1:0.97 for ScSScP, 1:0.90 for ScPScP, 1:1.72 for ScPPcP and 1:0.99 for PcPPcP. Although most slopes suggest that cross-correlation measurements are close to the theoretical predictions, many individual datapoints are located far from this slope.

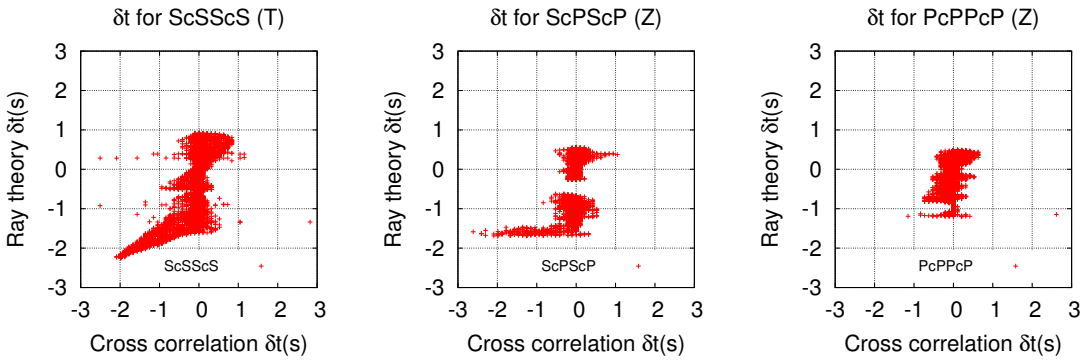

Figure 20: Scatter plot for double reflections (Similar to Figure 15)

3.3.3 Linear decomposition

Analogue to section 3.2.4, we study the linear additivity of mantle heterogeneity and CMB topography for double reflections. If the residual times $\delta t_{\text{residual}}$ are distributed in a narrow peak around zero, linear decomposition is possible for these phases. The histograms in Figure 21 show the distributions of $\delta t_{\text{residual}}$ for ScSScS, ScPScP and PcPPcP. The distribution of time differences between the models S20RTS+TOPO and PREM is shown on the background of each histogram to give an idea of the relative width of the $\delta t_{\text{residual}}$ distribution compared to the magnitude of the delays measured from cross-correlation of S20RTS+TOPO and PREM. The figures on the right are zoomed in on the lower part of the Y-axis of the figures on the left. The residual times of ScSScS, ScSScP, ScPPcP and PcPPcP are distributed closely around zero, which indicates that the assumption of linear decomposition is valid for these phases. The histogram of ScPScP stands out because the distribution of the residual times has the same width as the distribution of the measurements from full-waveform cross-correlation. This means that the magnitude of the errors introduced by assuming linear additivity of CMB topography and mantle heterogeneity is similar to the magnitude of the delays measured from full-waveform cross-correlation.

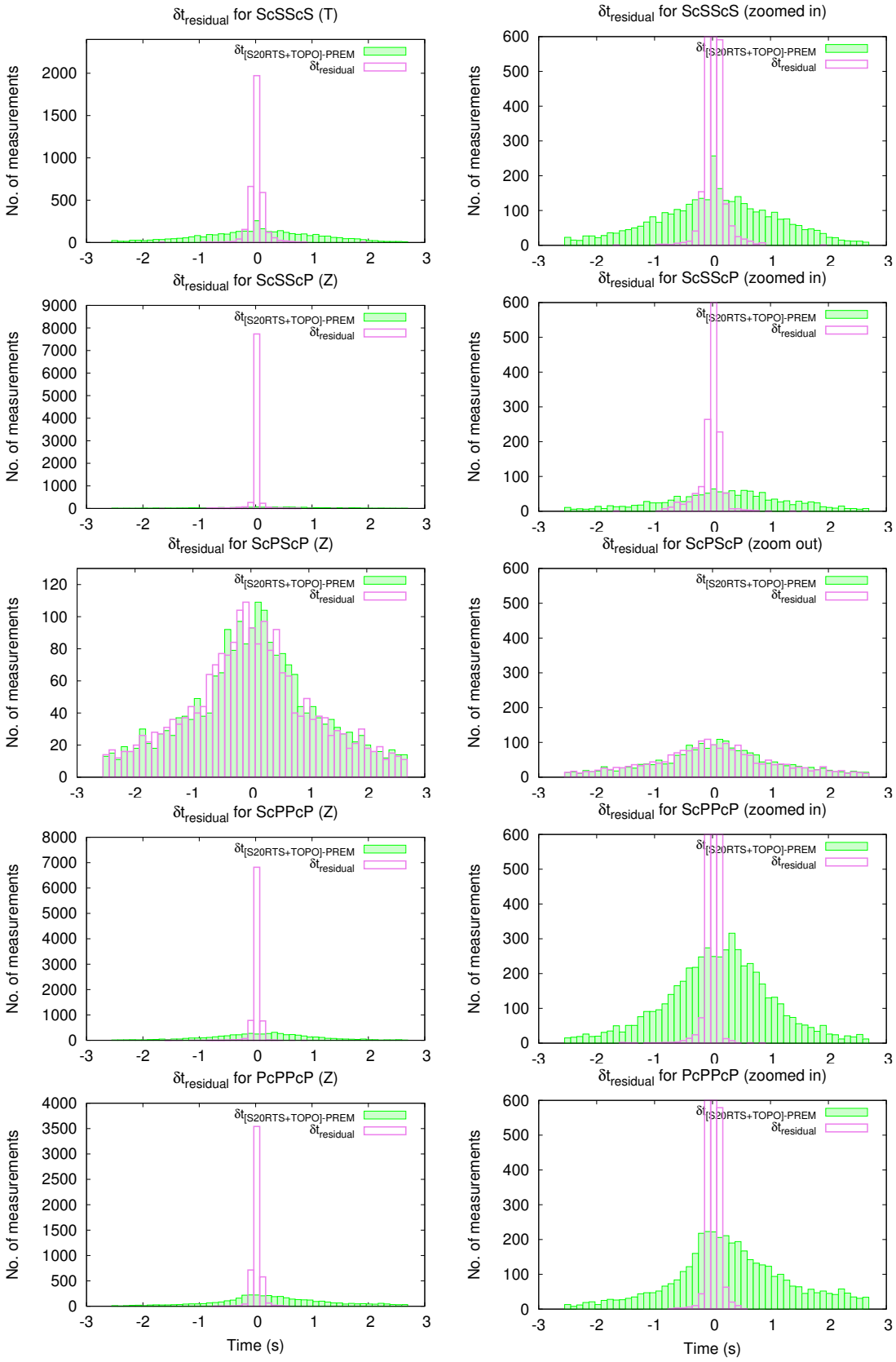

Figure 21: Similar to Figure 17, but for double reflections.

3.4 Diffracted phases

As ray theory does not take into account the effects of dispersion, there is no ray theoretical estimate for the arrival time of Pdiff and Sdiff. However, we can measure a difference in arrival time from cross-correlation of the full-waveform synthetic seismograms and compare these results directly with the input topography model to investigate if the the two physical quantities are related.

3.4.1 Maps

The following maps allow us to compare input CMB topography to the delays measured from cross-correlation. Figure 22a shows the the great circles of the paths that Pdiff samples along the CMB. The colour indicates the CMB topography along the path. The paths for Sdiff are nearly identical and are therefore not shown. Assuming that the delay caused by topography depends on the distance travelled along anomalous segments of the CMB, we divide the total delay measured from cross-correlation by the distance travelled along the CMB for each source-receiver combination. Plotting these differences in travel time per length unit results in Figure 22b and 22c. The opposite sign of delays compared to the topography is evident for both Sdiff and Pdiff, which means that diffracted waves travel longer when the topography is elevated. The response of Sdiff to the delay is slightly stronger than for Pdiff.

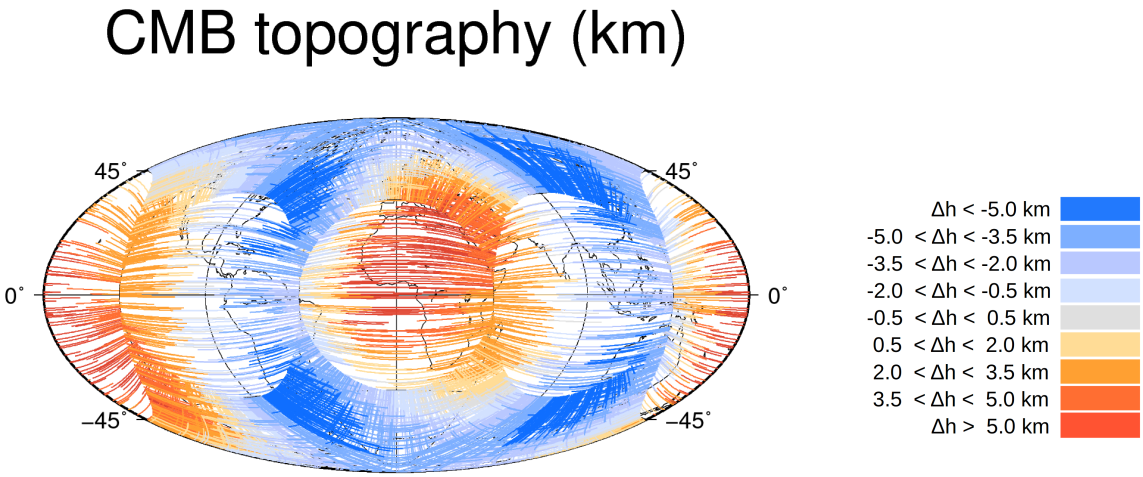

(a) Input topography

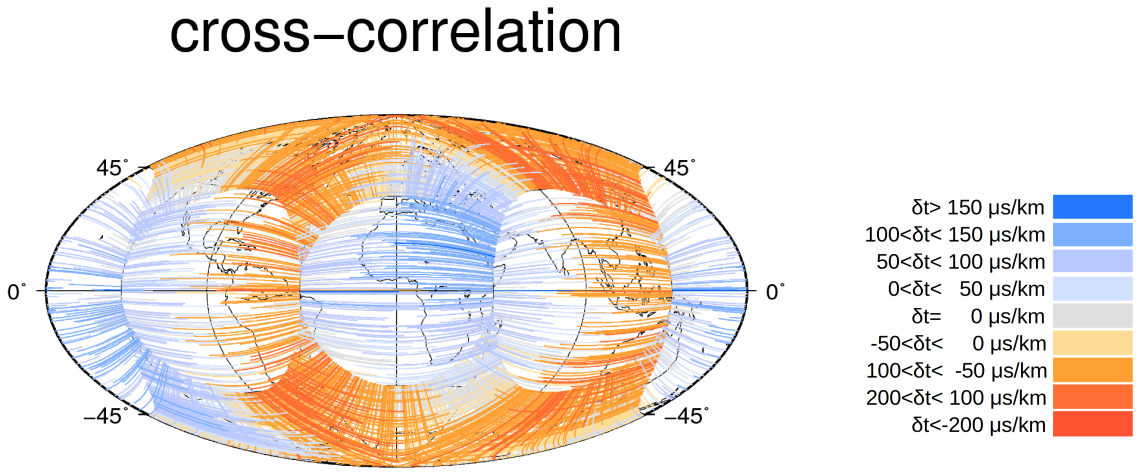

(b) Measured Pdiff

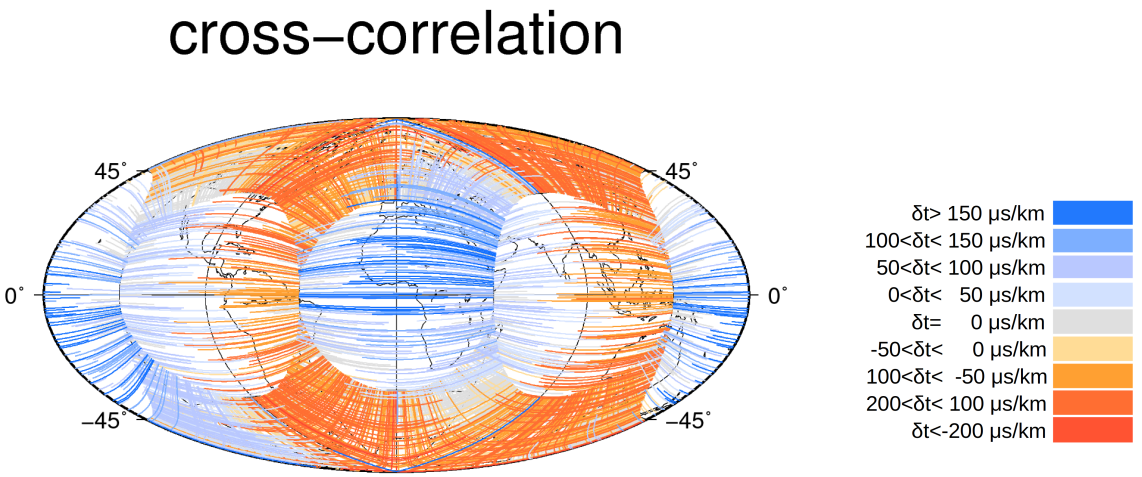

(c) Measured Sdiff

Figure 22: a) CMB topography along the path of Pdiff. Elevated topography has a positive sign (orange), depressed topography has a negative sign (blue). b) Pdiff's delay times from cross-correlation divided by the pathlength travelled along the CMB. c) Sdiff's delay times from cross-correlation divided by the pathlength travelled along the CMB.

3.4.2 Histograms

Although the maps in Figure 22 give a clear overview of the delay of diffracted waves per length unit, the histograms in Figure 23 are helpful to see the distribution of the total delays that are measured from the seismograms. For both Pdiff and Sdiff, most delays lie within ±0.3 s, which is within the measurement uncertainty of arrivals in seismograms. Therefore it may or not be possible to measure the arrival of Pdiff even if its relationship with CMB topography is evident.

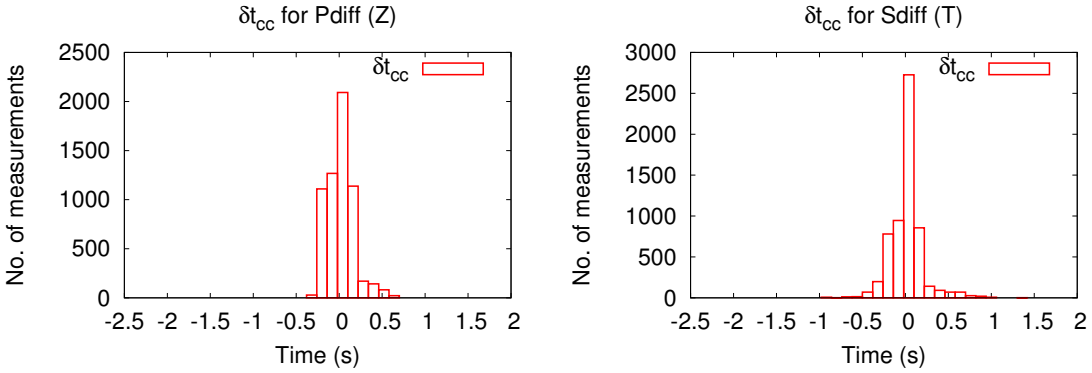

Figure 23: Histogram of the delays measured from cross-correlation in the seismograms for Pdiff (left) and Sdiff (right)

3.4.3 Linear decomposition

By comparing different configurations of PREM, S20RTS and Li *et al.*'s CMB topography we can investigate whether mantle heterogeneity and CMB topography are two independent parameters. If so, $\delta t_{\text{residual}}$ should be distributed in a narrow peak around 0 in the histograms of Figure 24. This is the case. Therefore linear decomposition of mantle heterogeneity and CMB topography is valid for Pdiff and Sdiff.

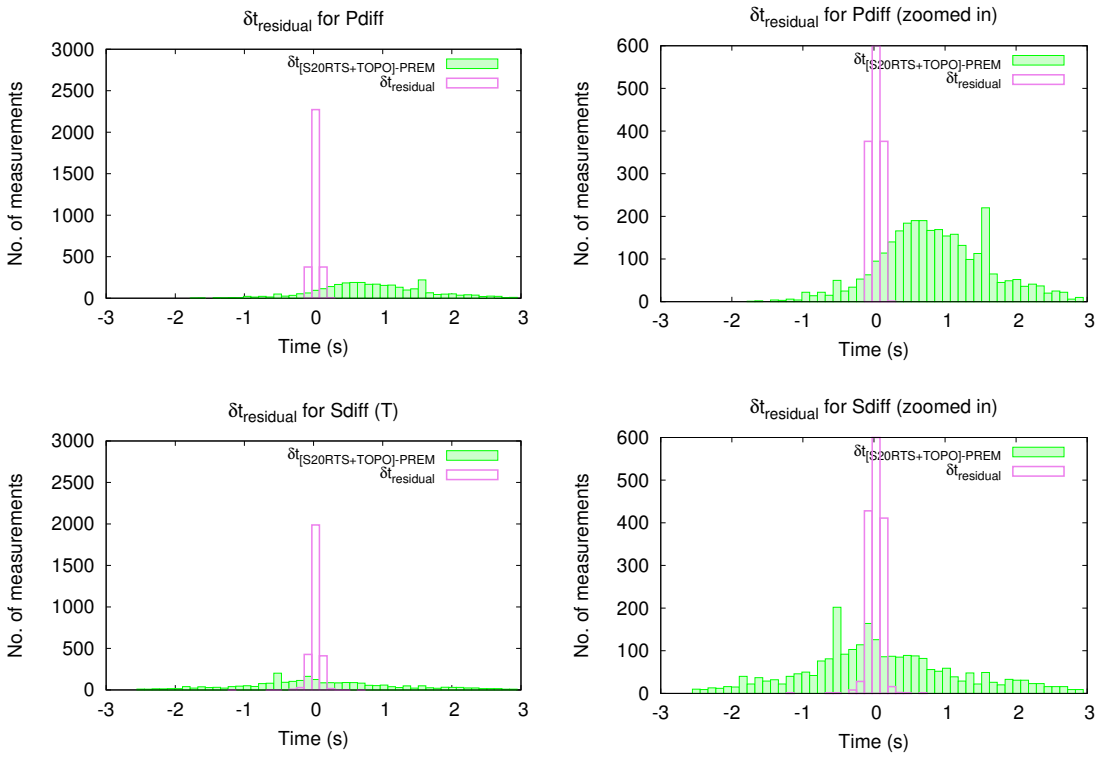

Figure 24: Linear decomposition of Pdiff and Sdiff, similar to Figure 17.

3.5 Variation along epicentral distance

In order to gain more insight into the relation between ray-theoretical predictions for delays and delays measured from full-waveform cross-correlation as a function of epicentral distance, the delays of the ScS phase, measured from cross-correlation of T-components of seismograms created by a shear source were analysed at 10° intervals. The scatter plots in Figure 25 show the ray theoretical predictions against each measurement from cross-correlation, as well as the linear regression through these data. Table 2 shows additional information about the linear regression. In Figure 25 we can see that at epicentral distances until 30°, ray theory predicts the correct sign but overestimates the amplitude of the delay by a factor of approximately 2.7. The datapoints for epicentral distances from 30° to 50° are more scattered but still show an upward trend. The 1:2.7 slope is retrieved between 60° and 70°. However, ray theory fails to predict the response to CMB topography beyond $\Delta > 70°$. The 30-50° interval coincides with the arrival of the surface waves. According to Figure 3,the travel time curves of S, PS and SP cross that of ScS beyond 70°. This is one of the possible causes that the delays due to CMB topography predicted by ray theory are not measured from cross-correlation of the synthetic seismograms.

The validity of the linear decomposition assumption was also tested at 10° intervals. We found that the contributions of mantle heterogeneity and CMB topography are linearly additive at all epicentral distances. The histograms of the residual times are not shown here for the sake of brevity, but are presented in Appendix B.

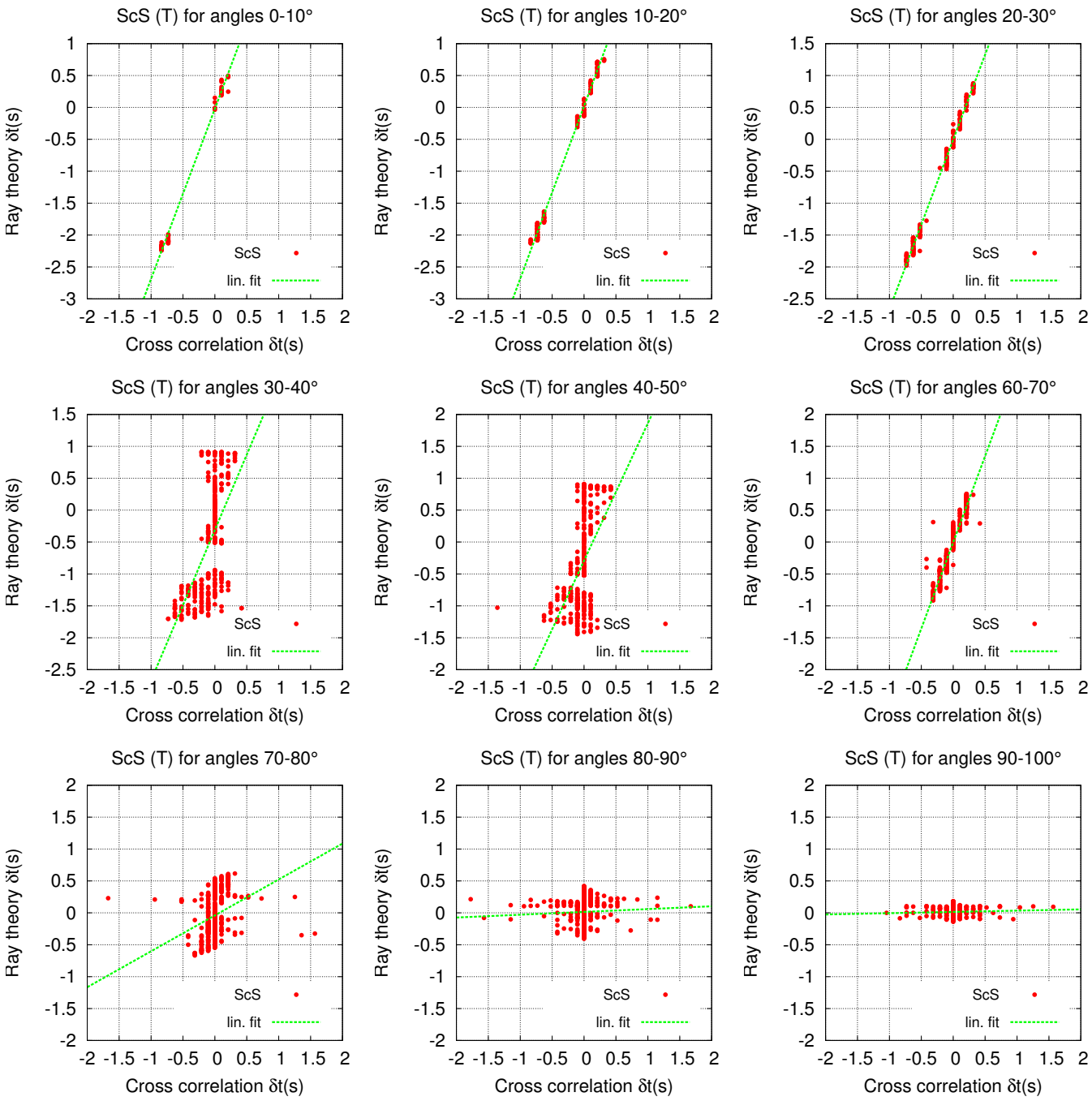

Figure 25: Scatter plots of ScS for 10° intervals.

Epicentral range	Slope	σ_{slope}	Ray theoretical relationship	Linearly additive
$0° - 10°$	2.67	0.03	yes	yes
$10° - 20°$	2.70	0.02	yes	yes
$20° - 30°$	2.66	0.02	yes	yes
$30° - 40°$	2.36	0.18	yes	yes
$40° - 50°$	2.15	0.17	partly	yes
$50° - 60°$	2.55	0.04	partly	yes
$60° - 70°$	2.70	0.03	yes	yes
$70° - 80°$	0.56	0.07	no	yes
$80° - 90°$	0.04	0.03	no	yes
$90° - 100°$	0.02	0.01	no	yes

Table 2: Statistics for different epicentral ranges. If the slope of the regression line is 1.0, the ray theoretical predictions of the delays are equal to the delays measured from cross-correlation of synthetic seismograms. σ_{slope} gives the standard deviation of the slope. The third column states whether the delays measured from cross-correlation are well described by a ray theory. If the datapoints of the scatter plot lay on a straight line, there is a linear relationship between ray theoretical predictions and delays measured from cross-correlation.

3.6 Ray theoretical prediction methods

In appendix C we compare the results from some of the single and double reflections for the two methods we used to calculate the ray theoretical estimates for the delays caused by CMB topography. One of the expressions was obtained via the polynomial fit to delays calculated by TauP, as was shown in Figure 4a. The other expression was given in equation 1. We found that for single reflections, the ray theoretical arrival times are very similar, and using either model will lead to the same results. The relationship between ray theoretical arrival times for double reflections is not 1:1. However, if we compare the main features of the topography maps as predicted by the two models, they are very similar. Both methods are suitable for the forward calculation of the ray theoretical value of the delay based on the topography.

4 Discussion

4.1 Ray theory versus cross-correlation

One of the main observations regarding the data is that ray theory in many cases is able to predict the sign of CMB topography correctly. This also holds for the S-phases studied, which have barely been used for CMB topography reconstructions until now. S-phases may therefore provide additional information on CMB topography stucture. Meanwhile, the interaction of studied phases with the topography does not always lead to differences in arrival time. The data analysis of ScS at small angle intervals in section 3.5 reveals that the quality of ray theoretical predictions depends on epicentral distance. The scatter plots in Figure 25 show that delays measured for ScS are more scattered when they are detected at epicentral distances between 30 and 50°. At angles beyond 70°, no relationship is evident. Similarly for PcP we measured no signal at epicentral distances of less than 20 degrees, between 30 and 40 degrees and beyond 50 degrees. The travel time curve in Figure 3 shows that around 40° epicentral distance, ScS arrives simultaneously with surface waves. As we saw in the seismogram in Figure 10b, the amplitude of the surface waves dominates over ScS. Therefore it may be harder to detect a time difference through cross-correlation. However, the surface waves differ sufficiently in physical properties to be able to separate the signal using more sophisticated filtering techniques. Similarly for PcP, the arrival times of PP and PPP are close to that of PcP around 40°. Reflection coefficients provide another explanation why no delays are measured from cross-correlation of synthetic seismograms at certain angles. Figure 2b shows the reflection coefficents at the CMB for PcP, PcS, ScP and ScS as a function of epicentral distance. PcP is mostly transmitted and barely reflected at epicentral distances below 20°. However, interference with other phases and reflection coefficients do not explain why no cross-correlation is measured beyond 50 ° for PcP. This suggests the presence of effects that cannot be explained by ray theory alone.

A more thorough investigation of each phase's ability to reproduce the correct sign of the topography at different epicentral distances helps to determine which subsets of seismograms are reliable for CMB mapping given the location of the source. Most of the studies cited in Table 1 already exclude epicentral distances for which multiple phases arrive simultaneously.

4.2 Diffracted phases

From Figure 22, it is evident that uplifted topography delays the arrival of diffracted phases. Similar observations were made by Colombi *et al.* (2012) who calculated sensitivity kernels of Pdiff using SPECFEM3D. One explanation of the sign of the delays is that diffracted phases travel at the velocity of the core in stead of the velocity of the mantle. The velocity in the core is lower, therefore the longer the path along the CMB, the longer the delay in arrival time. Schematic Figure 26 shows the path of diffracted phases for cores with large and small radii. Although this figure is not to scale, it illustrates how the path of the diffracted phase along the CMB is longer for a locally elevated CMB (large core radius), and shorter for a locally depressed CMB (small core radius). Combining the slow propagation

velocity of diffracted phases along the CMB with longer paths for elevated topography, we can explain that elevated topography leads to late arrivals of Pdiff and Sdiff while depressed topography leads to early arrivals.

Pdiff and Sdiff have not been used before to study CMB topography. However, there have been several studies that reconstructed velocity anomalies in the D" layer from Pdiff and Sdiff travel time anomalies (Wysession *et al.* 1992, Wysession 1996, Kárason & van der Hilst 2001). These studies, do not take into account CMB topography. Therefore, elevated CMB topography may be misinterpreted as slowness in the D" region, but we currently have no estimate for the relative error it introduces. Koelemeijer *et al.* (2013) made the first observations of CMB Stonely modes and were able to relate their splitting functions to Pdiff and Sdiff travel-time anomalies. Although this suggests a physical relationship between the two, the splitting functions do not put additional constraints on CMB topography because the Stonely modes depend on several physical quantities including velocity and density.

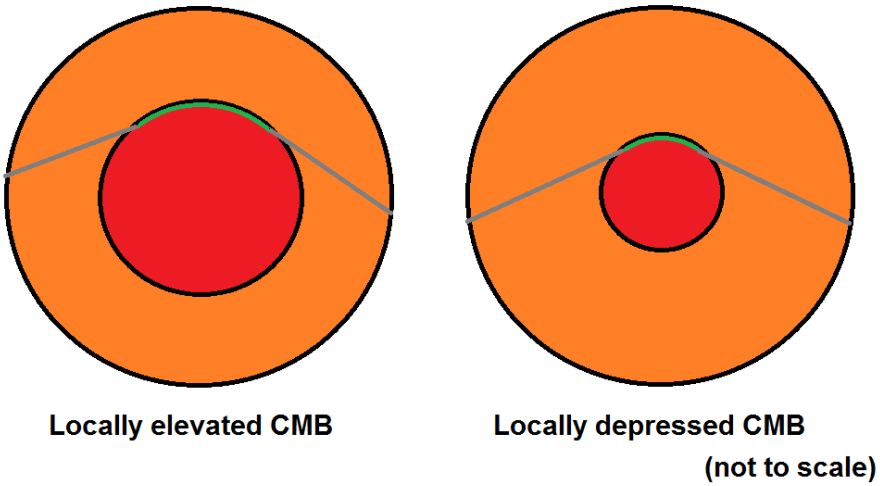

Figure 26: Schematic figure of the path of diffracted phases through the mantle (orange) and core (red). The path of the diffracted phase along the CMB (green) is longer if the core is larger.

4.3 Linear decomposition

The histograms in Figures 17, 21 and 24 show that linear decomposition is possible for all phases studied, except for ScPScP. The assumption that the delays that remain after subtracting the contribution of the mantle model, can be attributed to CMB topography, is therefore mostly valid. Provided that the used mantle model is correct, the contribution of CMB topography can therefore be isolated. The fragility of this condition should not be underestimated. Colombi *et al.* (2014) concluded for their CMB topography models that the magnitude of the traveltime anomaly due to CMB topography is as small as a tenth of the traveltime anomaly caused by mantle heterogeneities. Therefore CMB topography residuals are likely to be strongly biased by overlying structures.

The observed differences between the linear additivity of ScPScP and its neighbouring phases ScSScP and ScPPcP is striking. Although there are four permutations of 3 S branches and 1 P branch that form a double reflection that arrives at the same time as ScSScP, ScSScP is the only phase that can be recorded on the Z-component of the seismogram. Therefore it was possible to resolve its bouncepoints. For ScPPcP, it was deducted from section 3.2.1 that PcS and PcP have a weaker signal than ScP. In order to have a phase that is strong enough to be detected after a second reflection, it was reasoned that ScP should constitute the first part of the wave and that PcP should follow.

For ScPScP, there are six permutations of P and S branches. There are 3 phases that that end in P and can therefore be detected on the Z-component of the seismogram. They arrive at the same time but pierce the CMB at 6 different possible epicentral distances. If the amplitude of ScPScP does not dominate over over the amplitude of other permutations that arrive simultaneously, the ray theoretical estimate based on the topography at the bouncepoints will be off. This suggests that ScPScP is not a suitable phase to study CMB topography in the first place.

Comparing our overall results to those of Koroni & Trampert (2012), we find that ray theory predicts the CMB topography from core reflections and refractions much better than it predicts 410 and 660 discontinuity topography from SS waves. We suppose that this follows from the difference in shape of the Fresnel zones, which indicate the off-ray sensitivity of a phase. Figure 27 shows the Fresnel zones for PcP and S660S as calculated by Dahlen (2005). The Fresnel zone of the other core reflections have a circular shape similar to PcP. The Fresnel zones for Pdiff and Sdiff are larger and more elongated, but their nature is comparable. The X-shape of the S660S Fresnel zone is representative for minimax phases such as SS which was studied by Koroni & Trampert (2012) . The sensitivity of minimax phases to mantle heterogeneities relatively far from the ray theoretical path provides an explanation for the observed differences in linear decomposability of Koroni & Trampert's SS waves and our core phases.

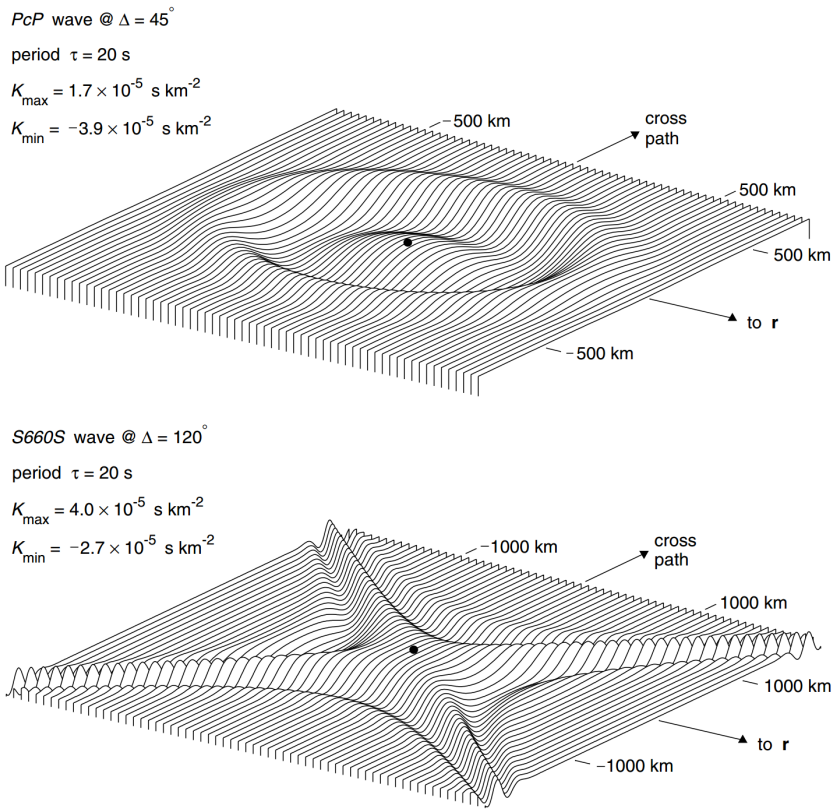

Figure 27: Fresnel zones of PcP (top) and S660S (bottom). The fresnel zones of ScP, PcS and ScS are similar to that of PcP. The fresnel zones of Pdiff and Sdiff are larger and more elongated than PcP. The sensitivity has concentric rings and decays with distance from the theoretical ray. The Fresnel zone of S660S has an X-shape. The sensitivity does not decay with distance along the four legs. Figure taken from Dahlen, 2005.

4.4 Outlook

The scope of this research was limited to single and double reflections of core phases and diffracted phases. We did not investigate the different branches of PKP and PKKP, which are often used for tomographic inversions, although some branches may have been visible on the seismograms in Section 3.1. Further inspection of the synthetic seismograms may also serve to identify more phases that are sensitive to CMB topography but have not received attention in literature yet.

In this model we investigated to what extent ray theory correctly predicts the seismic response to a core mantle boundary with very large wavelength structure. However, the CMB is likely to contain shorter wavelength structures as well. By repeating this research for increasingly shorter wavelength CMB topography, we could quantify the smallest wavelength for which CMB topography can be resolved.

When studying double reflections, equal contributions from each bouncepoint were assumed. However, information from single reflections and double reflections could be combined. Single reflections could constrain the topography at the bouncepoint

close to the source, so that the remaining delay time can be attributed to the second bouncepoint.

One of the main obstacles in the analysis of synthetic seismograms from 3D Earth models is the limited resolution of the phases. The computational lower limit for periods is 10s. Typical observed P-wave frequencies are one tenth of this value. The long period causes nearby arriving phases to interfere more than in real seismograms. If we generate synthetic seismograms for a smaller segment of the Earth, it should be possible to decrease the period. However, by studying a smaller segment we will be limited to phases that arrive at a small epicentral distance from the source.

The seismograms that were generated in this study are idealised compared to seismograms from real earthquakes. Real seismograms contain noise, making it harder to detect the exact arrival time of phases with small amplitudes. Moreover, the distribution of seismic stations on the globe is far from even. In practice there are be parts of the CMB that will be relatively undersampled. Repeating the experiments with noise and uneven station distributions will lead to a more realistic estimate of information we can and cannot gain from applying ray theory to real seismograms.

5 Conclusion

In an Earth with PREM as a base model, S20RTS as a mantle model and an 8 km-amplitude CMB topography model from Li et al., 1991a, ray theory correctly estimates the sign of the CMB topography for the phases PcP, ScP, ScS, ScSScS, ScSScP, ScPPcP and PcPPcP at most epicentral distances in absence of interference with other phases, provided that the reflection coefficients are sufficiently high. Magnitudes are generally overestimated by ray theory, by factors 1.3-2.5 for single core reflections and factors 1.0-1.7 for double core reflections. Diffracted phases are delayed by uplifted CMB topography, which is opposite to the response of reflected phases to CMB topography. Linear decomposition of effects from mantle heterogeneities and CMB topography is possible for all phases mentioned above.

References

[1] Kenneth C. Creager and Thomas H. Jordan. Aspherical Structure of the Core-Mantle Boundary from PKP Travel Ttimes. *Geophysical Research Letters*, 13(13):1497–1500, 1986.

[2] A. M. Forte, J. X. Mitrovica, and R. L. Woodward. Seismic-geodynamic determination of the origin of excess ellipticity of the core-mantle boundary. *Geophysical Research Letters*, 22(9):1013–1016, 1995.

[3] T. M. Lassak, A. K. McNamara, and S. Zhong. Influence of thermochemical piles on topography at earth's core-mantle boundary. *Earth and Planetary Science Letters*, 261(3-4):443–455, 2007.

[4] G. Soldati, L. Boschi, and A. M. Forte. Tomography of core-mantle boundary and lowermost mantle coupled by geodynamics. *Geophysical Journal International*, 189(2):730–746, 2012.

[5] P. J. Koelemeijer, A. Deuss, and J. Trampert. Normal mode sensititivy to earth's d" layer and topography on the core-mantle boundary: what we can and cannot see. *Geophysical Journal International*, 190:553–568, 2012.

[6] B. H. Hager, R. W. Clayton, A. M. Dziewonski, A.M. Richards, and R.P. Corner. P and pcp travel time tomography for the core-mantle boundary. *Nature*, 313:541–545, 1985.

[7] X. Li, D. Giardini, and J. H. Woodhouse. The relative amplitudes of mantle heteregeneity in p velocity, s velocity and density from free-oscillation data. *Geophysical Journal International*, 105(3):649–657, 1991.

[8] M. Ischii and J. Tromp. Normal-mode and free-air gravity constraints on lateral variation in velocity and density of earth's mantle. *Science*, 285:1231–1236, 1999.

[9] A. Morelli and A. M. Dziewonski. Topography of the core-mantle boundary and lateral homogeneity of the liquid core. *Nature*, 325:678–683, 1987.

[10] A. Rodgers and J. Wahr. Inference of core-mantle boundary topography from isc pcp and pkp traveltimes. *Geophysical Journal International*, 115:991–1011, 2012.

[11] L. Boschi and A.M. Dziewonski. Whole earth tomography from delay times of p, pcp and pkp phases: lateral heterogeneities in the outer core or radial anisotropy in the mantle? *Journal of Geophysical Research*, 105(B6):13675–13696, 2000.

[12] G. Soldati, L. Boschi, and A. Piersanti. Outer core density heterogeneity and the discrepancy between pkp and pcp travel time observations. *Geophysical Research Letters*, 30(4), 2003.

[13] R. Garcia and A. Souriau. Amplitude of the core-mantle boundary topographhy estimated by stochastic analysis of core phases. *Physics of the Earth and Planetary Interior*, 117:345–359, 2000.

[14] P. Hubral, J. Schleicher, M. Tygel, and Ch. Hanitzsch. Determination of fresnel zones from traveltime measurements. *Geophysics*, 58(5):703–712, 1993.

[15] M. Koroni and J. Trampert. The effect of topography of upper-mantle discontinuities on ss precursors. *Geophysical Journal International*, 204(1):667–681, 2012.

[16] D. W. Vasco, L. R. Johnson, and O. Marques. Global earth structure: inference and assessment. *Geophysics Journal International*, 137:381–407, 1998.

[17] E. K. M. Sze and R. D. van der Hilst. Core mantle boundary topography from short period pcp, pkp, and pkkp data. *Physics of the Earth and Planetary Interiors*, 135:27–46, 2002.

[18] S. Tanaka. Constraints on the core-mantle boundary topography from p4kp-pcp differential travel times. *Journal of Geophysical Research*, 115:57–71, 2010.

[19] P. M. Shearer. *Introduction to Seismology.* Cambridge University Press, Cambridge, UK, 2009.

[20] K. Aki and P. G. Richards. *Quantitative Seismology.* University Science Books, Herndon, VA, USA, 2002.

[21] A. Ben-Menahem and S. J. Singh. *Seismic Waves and Sources.* Dover Publications, Mineola, New York, 2012.

[22] D. Komatitsch and J. P. Vilotte. The spectral-element method: an efficient tool to simulate the seismic response of 2d and 3d geological structures. *Bulletin of the Seismological Society of America*, 88(2):368–392, 1998.

[23] A. M. Dziewonski, M. Anderson, and L. Don. Preliminary reference earth model. *Physics of the Earth and Planetary Interiors*, 25(4), 1981.

[24] H J. Ritsema, J. van Heijst, and J.H. Woodhouse. Global transition zone tomography. *Journal of Geophysical Research*, 109(B2), 2004.

[25] H. Kárason and R. D. van der Hilst. Tomographic imaging of the lowermost mantle with differential times of refracted and diffracted core phases (pkp, pdiff). *Journal of Geophysical Research*, 106(B4):6569–6587, 2001.

[26] M. E. Wysession, E. A. Okal, and C. R. Bina. The structure of the core-mantle boundary from diffracted waves). *Journal of Geophysical Research*, 97(B6):8749–8764, 1992.

[27] M. E. Wysession. Large-scale structure at the core-mantle boundary from diffracted waves. *Nature*, 382:244–248, 1996.

[28] P. Koelemeijer, A. Deuss, and J. Ritsema. Observations of core-mantle boundary stonely modes. *Geophysical Research Letters*, 40:2557–2561, 2013.

[29] A. Colombi, T. Nissen-Meyer, L. Boschi, and D. Giardini. Seismic waveform inversion for core-mantle boundary topography. *Geophysical Journal International*, 208(2), 2014.

A Attenuation

In this section we show that the seismic signals obtained in a medium with and without attenuation are similar, an thereby justify that we compare Z-components of attenuated seismograms and T-components of nonattenuated seismograms in the main study. Figures 28 to 31 show the seismograms of the attenuated signal (top) and the nonattenuated signal (bottom). Both the timing and amplitude of incoming phases is similar. The maps in Figure 32 show that similar delays are measured at the bouncepoints. Also the pattern of two concentric rings is conserved. From the scatter plots and histograms in Figure 32 we see some differences in the distribution of the data. The shape of a tilted hour glass is visible in both scatter plots. However, comparing the error in the data ($\delta t_{\mathrm{cc}} - \delta t_{\mathrm{th}}$), we see that the errors of the attenuated case are centered around zero whereas the errors of the nonattenuated case have a wider and slightly bimodal distribution.

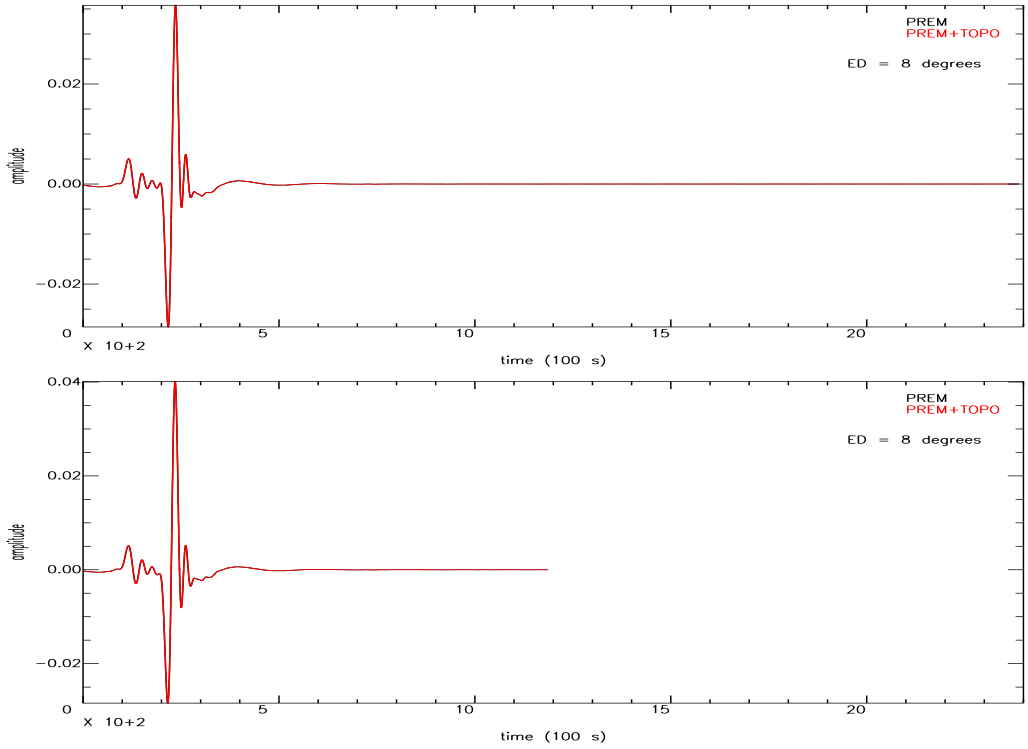

Figure 28: Z-component of seismograms at 8° epicentral distance, created by an explosive source. The top figure shows the first 2400 s of the signal in a medium with attenuation, the bottom figure shows the first 1200 s of the signal in a medium without attenuation

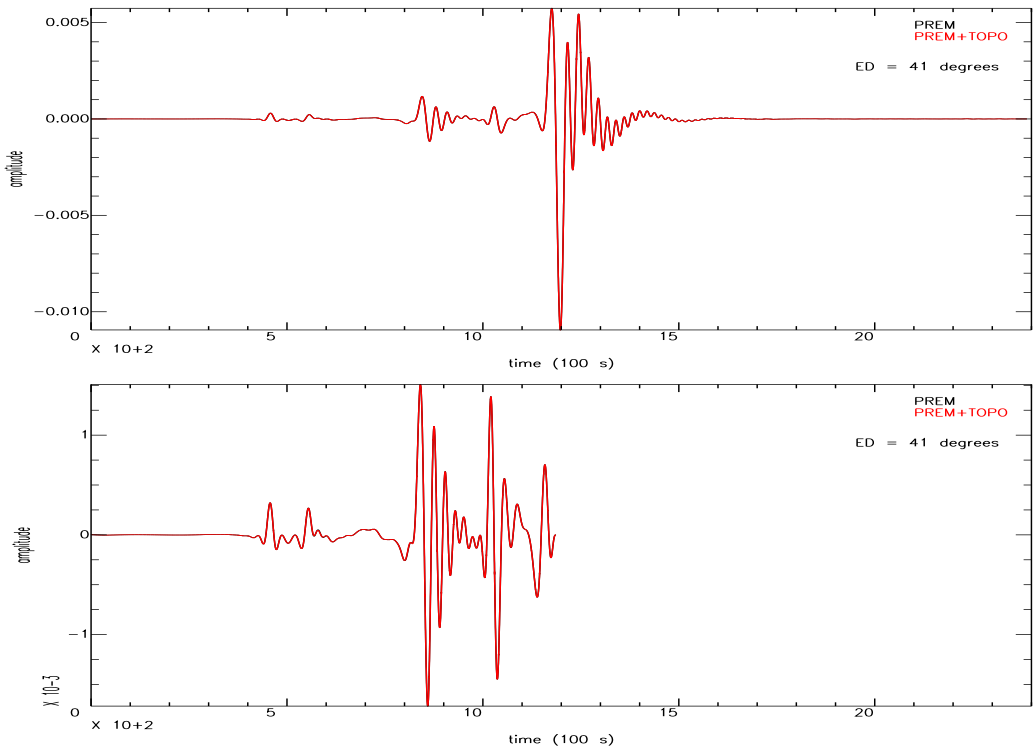

Figure 29: Z-component of seismograms at 41° epicentral distance, created by an explosive source. The top figure shows the first 2400 s of the signal in a medium with attenuation, the bottom figure shows the first 1200 s of the signal in a medium without attenuation. Note that the peaks of the two seismograms have similar amplitudes, even though the Y-axes differ.

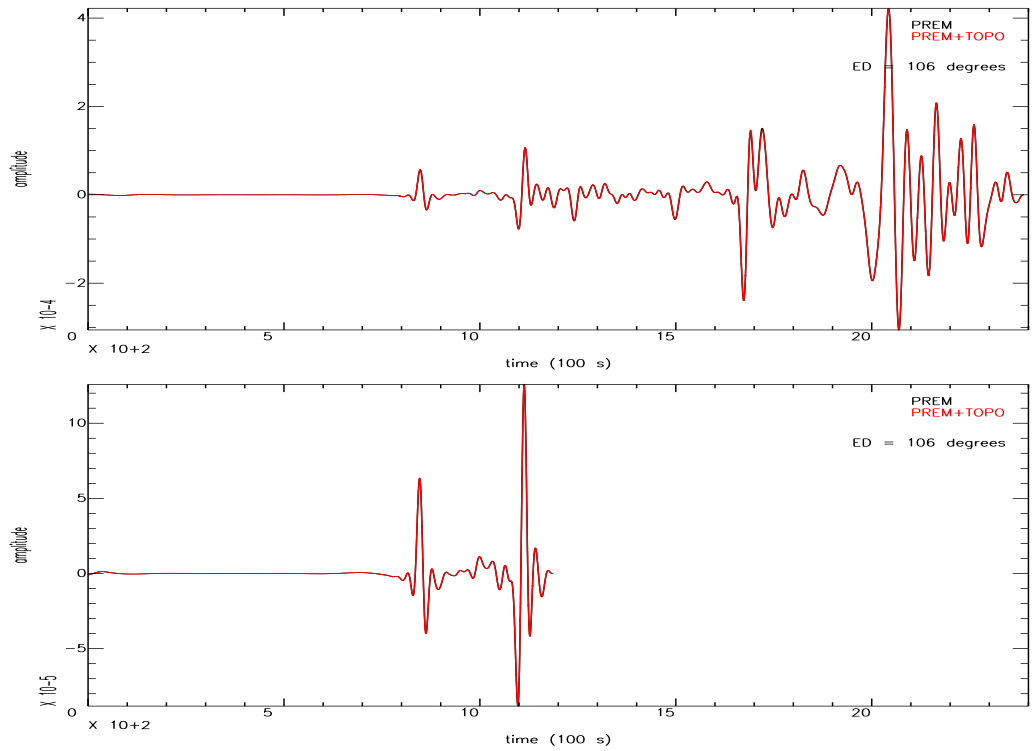

Figure 30: Z-component of seismograms at 105° epicentral distance, created by an explosive source. The top figure shows the first 2400 s of the signal in a medium with attenuation, the bottom figure shows the first 1200 s of the signal in a medium without attenuation. Note that the peaks of the two seismograms have similar amplitudes, even though the Y-axes differ.

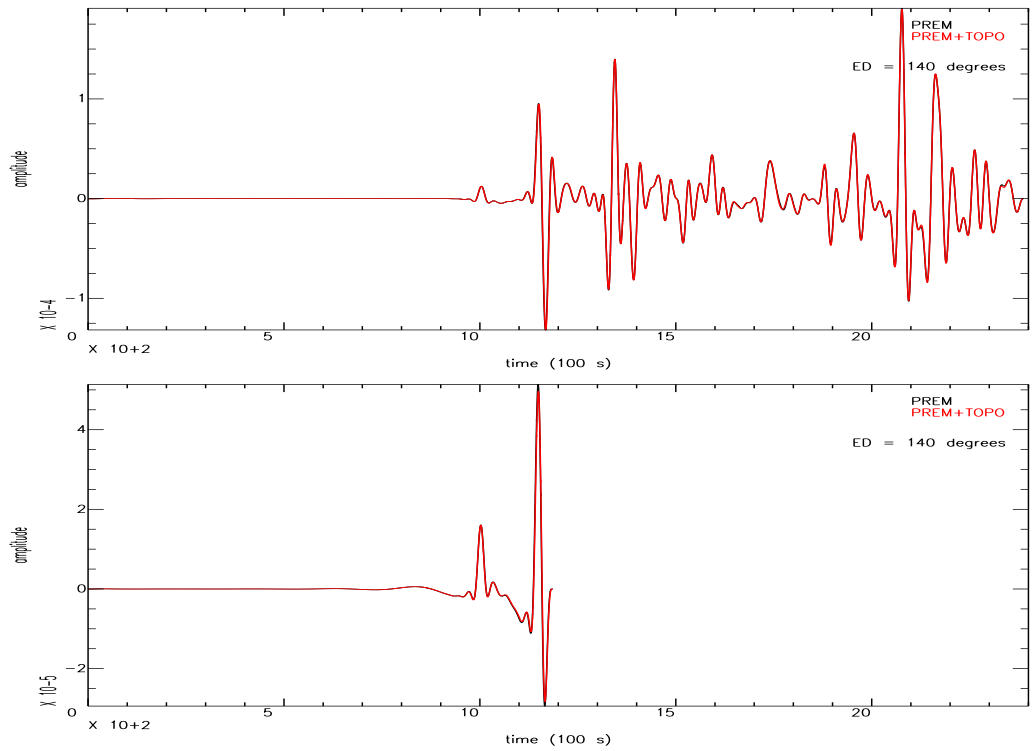

Figure 31: Z-component of seismograms at 140° epicentral distance, created by an explosive source. The top figure shows the first 2400 s of the signal in a medium with attenuation, the bottom figure shows the first 1200 s of the signal in a medium without attenuation.

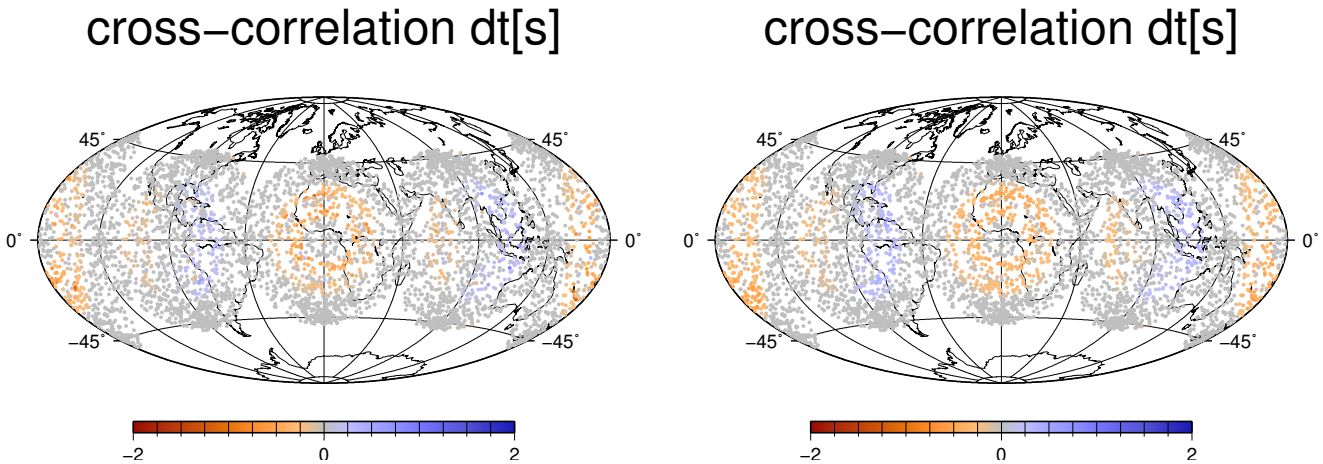

(a) (b)

Figure 32: The maps show the bouncepoints of PcP that correspond to the seismic stations that were used for cross-correlation. The colour of the dots indicates the delay measured from cross-correlation of the full-waveform synthetic seismograms. The left figure shows the measurements in an attenuated medium, the right figure shows the measurements in a nonattenuated medium.

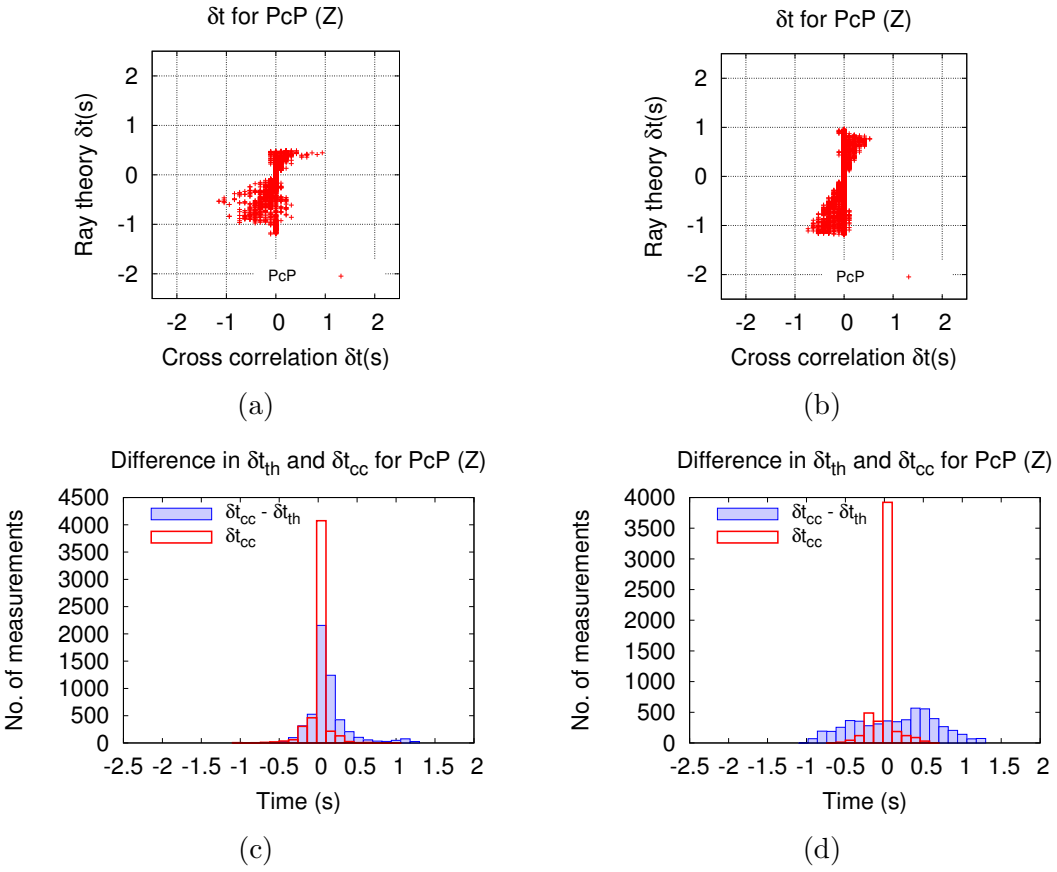

Figure 33: Figure 33a shows a scatter plot of the delays predicted by ray theory against the delays measured from cross-correlation of synthetic seismograms in an attenuated medium, Figure 33b shows the same ray theoretical predictions for delays against the delays measured from cross-correlation of synthetic seismograms for a nonattenuated medium. The histogram of Figure 33c shows the distribution of the difference between delays measured from cross-correlation and ray theoretical delays (blue). The peak around zero indicates that the measurements from cross-correlation are often identical to the predictions. Figure 33d shows the same histogram for the cross-correlation measurements of synthetic seismograms in a nonattenuated medium. The difference between cross-correlation measurements and ray theoretical predictions is more widely distributed, which indicates that the error in the predictions is larger for a nonattenuated medium.

B Variation along epicentral distance: Linear decomposition

This section is a continuation of section 3.5, where the cross-correlation measurements of synthetic seismograms are analysed at 10° intervals for ScS. Figure 34 shows histograms of the linear decomposition of mantle heterogeneity and CMB topography at different ranges of epicentral distance. In all histograms, the distributions of the residual times are narrow compared to distributions of the delays measured from cross-correlation of full-waveform synthetic seismograms generated for the input models [S20RTS+TOPO] and [PREM]. This indicates that errors introduced by assuming linear additivity are small compared to the delays measured from cross-correlation.

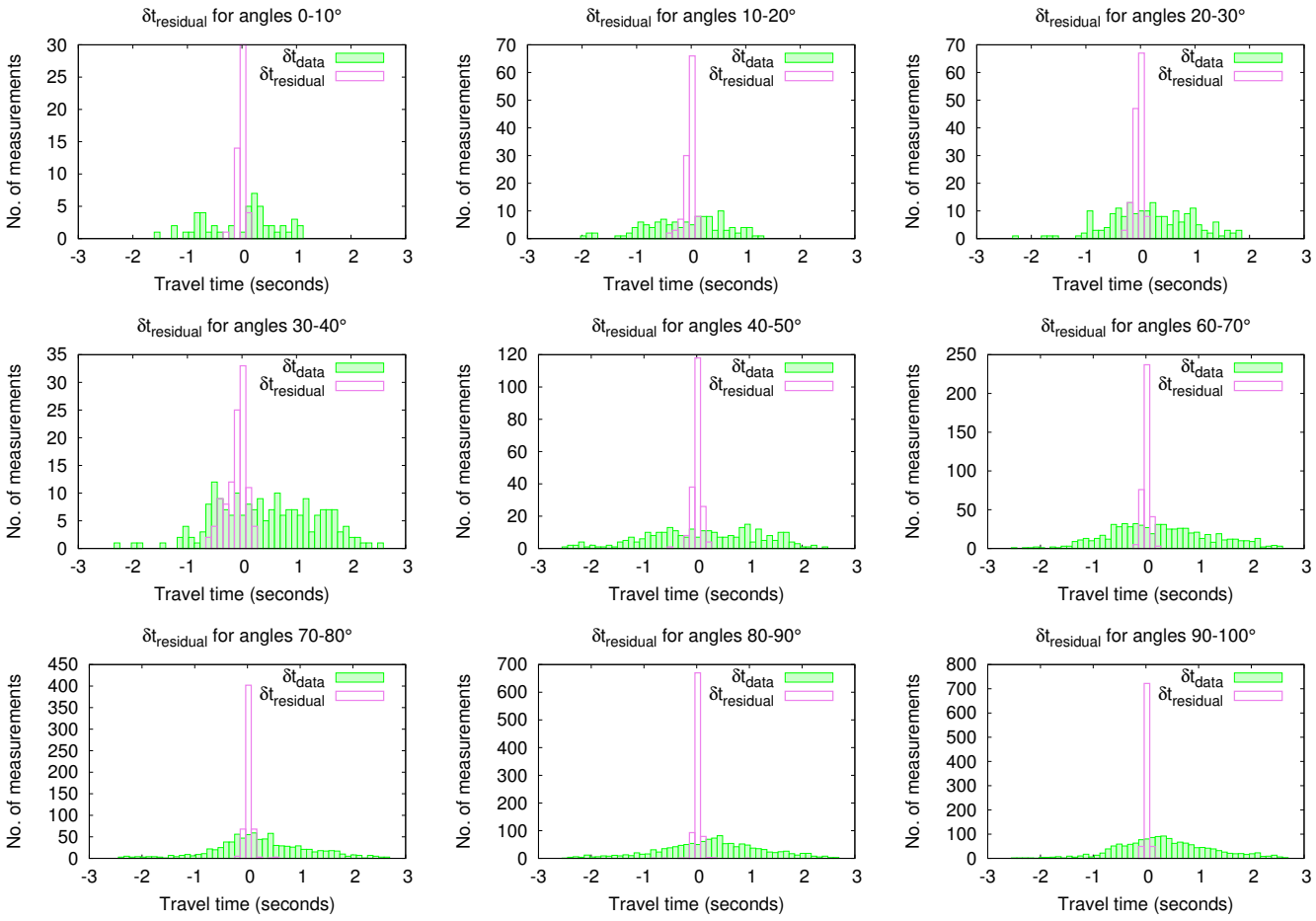

Figure 34: Histograms of residuals times of ScS for 10° intervals. $\delta t_{\text{residual}}$ (green) was defined in equation 5 as the difference between the delays measured from cross-correlation for a model with both mantle heterogeneity and CMB topography, and the sum of the individual delays caused by mantle heterogeneity and CMB topography. δt_{data} (violet) shows the delays measured from cross-correlation of the input models [S20RTS+TOPO] and [PREM]. A narrow distribution of $\delta t_{\text{residual}}$ compared to δt_{data} indicates that errors introduced by assuming linear additivity is small compared to the delays measured from cross-correlation.

C Ray theoretical prediction methods

In this section we compare the differences in ray theoretical predictions for delays due to CMB topography calculated via equation 1 and the predictions calculated via the polynomial fit made using TauP. We do not expect the predictions to be exactly the same, because in Figure 4a we observed that at large epicentral distances, equation 1 overestimates the magnitude of the delay compared to the delays predicted by the polynomial fit. We compare several key results obtained using the two ray theoretical prediction methods, in order to see if the difference in ray theoretical predictions for delays leads to significantly different final conclusions about the relationship between CMB topography and travel time delays.

Figure 35 shows the relationship between the delays predicted from equation 1 and the polynomial fit. For the single core reflections (PcP, ScP, ScS), most datapoints lie on a straight line with a slope of 45°, indicating a 1:1 relationship between most ray theoretical predictions from equation 1 and the polynomial fit. For double core relfections (PcPPcP, ScPScP, ScSScS) we observe a different pattern. In each plot we see a cloud of data on the left with the shape of an upside-down drop and a cloud of data on the right in the shape of an arc. This shows that for double reflections, the difference in ray theoretical predictions can be large and is not explained by a linear relationship.

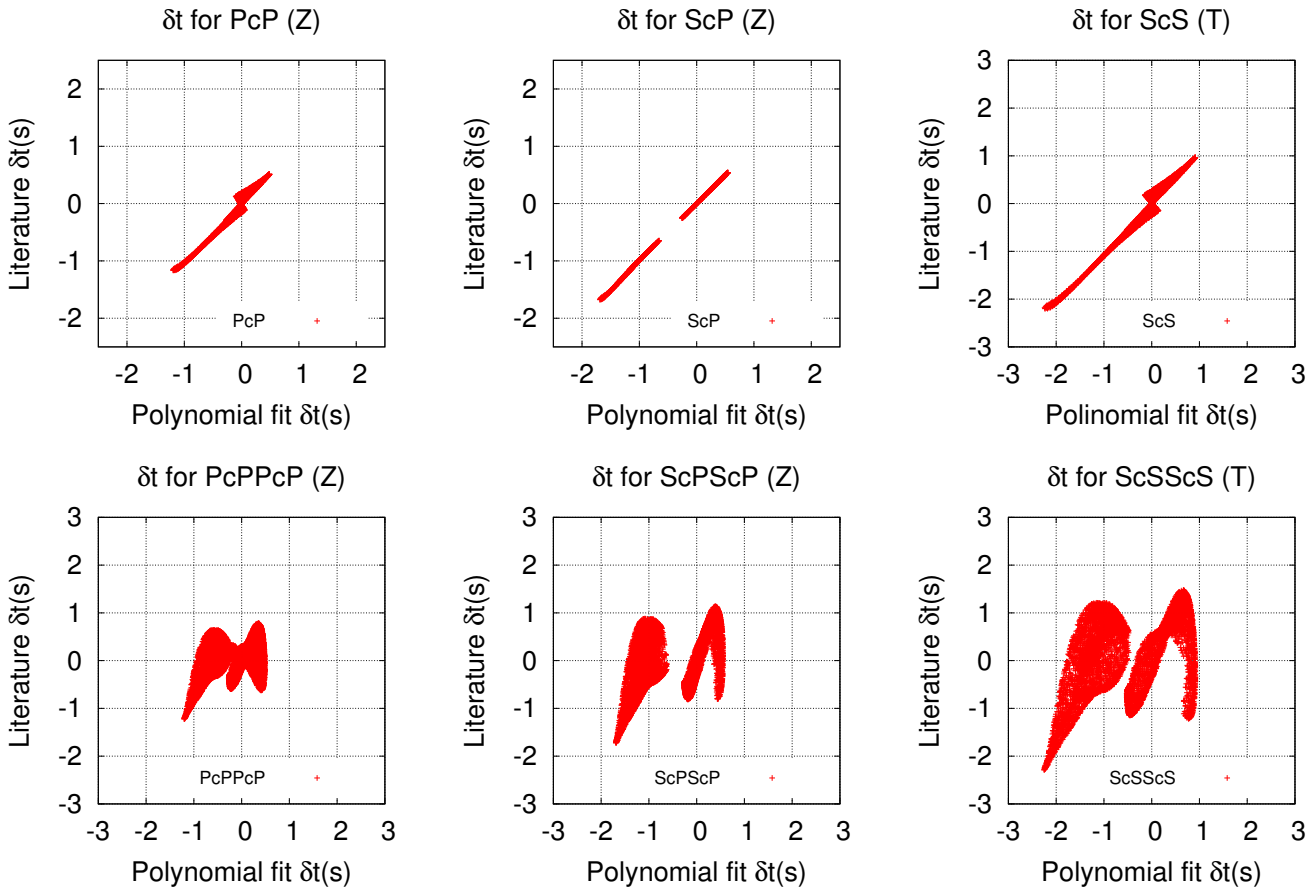

Figure 35: Scatter plots of ray theoretical predictions for delays using equation 1 against ray theoretical predictions for delays from the polynomial fits made using TauP. If the predictions are always the same, the data points lay on a straight line with a slope of 45°.

We now compare the results obtained for PcP using each method. As is shown in Figures 36a and 36b, the geographical distribution of the the delays that correspond to the sampled bouncepoints is nearly identical for the figures calculated using the polynomial fit (left) and equation 1. The shape of the scatter plots that show the delays from ray theoretical predictions against delays measured from cross-correlation of synthetic seismograms is also very similar (Figures 36c and 36d). The histograms in Figure 36e and 36f show the difference between delays measured from cross-correlations (δt_{cc}) and the delays predicted from ray theory (δt_{th}). The distribution of $\delta t_{\mathrm{cc}} - \delta t_{\mathrm{th}}$ has a higher peak around zero when the ray theoretical predictions are calculated using the polynomial fit from TauP (Fig. 36e). This tells us that the ray theoretical predictions for delays made using the polynomial fit are more often identical to the delays measured from cross-correlation of synthetic seismograms, than the predictions made using equation 1.

In Figure 37 the results of ScSScS are shown for ray theoretical predictions calculated using the polynomial fit (left panels) and the predictions calculated from equation 1 (right panels). Even though the scatter plots of Figure 35 suggested that the predicted delays of double core reflections significantly differ between the two methods, the maps in Figure 37a and 37b look very similar. Therefore the

difference in ray theoretical predictions does not affect the spatial distribution of delays measured at the bouncepoints.

The differences in the two prediction methods are more evident in the scatter plots of Figure 37c and 37d. The alignment of datapoints in Figure 37d shows that there is a more pronounced relationship between cross-correlation measurements and ray theoretical delays predicted using equation 1. The histograms in Figure 37e and 37f show that neither of the prediction methods is optimal.

The distribution of Δt (blue) shows the difference between delays measured from cross-correlations and the delays predicted from ray theory. The highest peak of Δt in Figure 37e is located at 0 seconds, which shows that ray theoretical predictions for delays from the polynomial fit are often equal to the delays measured from cross-correlation of synthetic seismograms. However, the bimodality of the distribution of Δt also shows that there is a systematic effect causing an error of approximately one second between a part of the ray theoretical predical delays and the corresponding cross-correlation measurements. The distribution of Δt for ray theoretical predictions calculated via equation 1 is centered around -0.6 seconds, which suggests that this method overestimates delayed arrivals due to depressed CMB topography more than it overestimates early arrivals due to elevated CMB topography (Fig. 37f). We can draw the same conclusions from Figure 38, which shows the same Figures for ScPScP.

Although we observe several differences in the characteristics of the scatter plots and the histograms of Figures 37 and 38, their main features are conserved. The maps in Figures 36a, 37a and 38a calculated using the polynomial fit, and the maps in Figures 36b, 37b and 38b calculated using equation 1 are also similar. The approximation made to obtain equation 1 does not lead to worse results than those obtained using the polynomial fit. Therefore both methods are valid to calculate ray theoretical predictions for delays due to CMB topography.

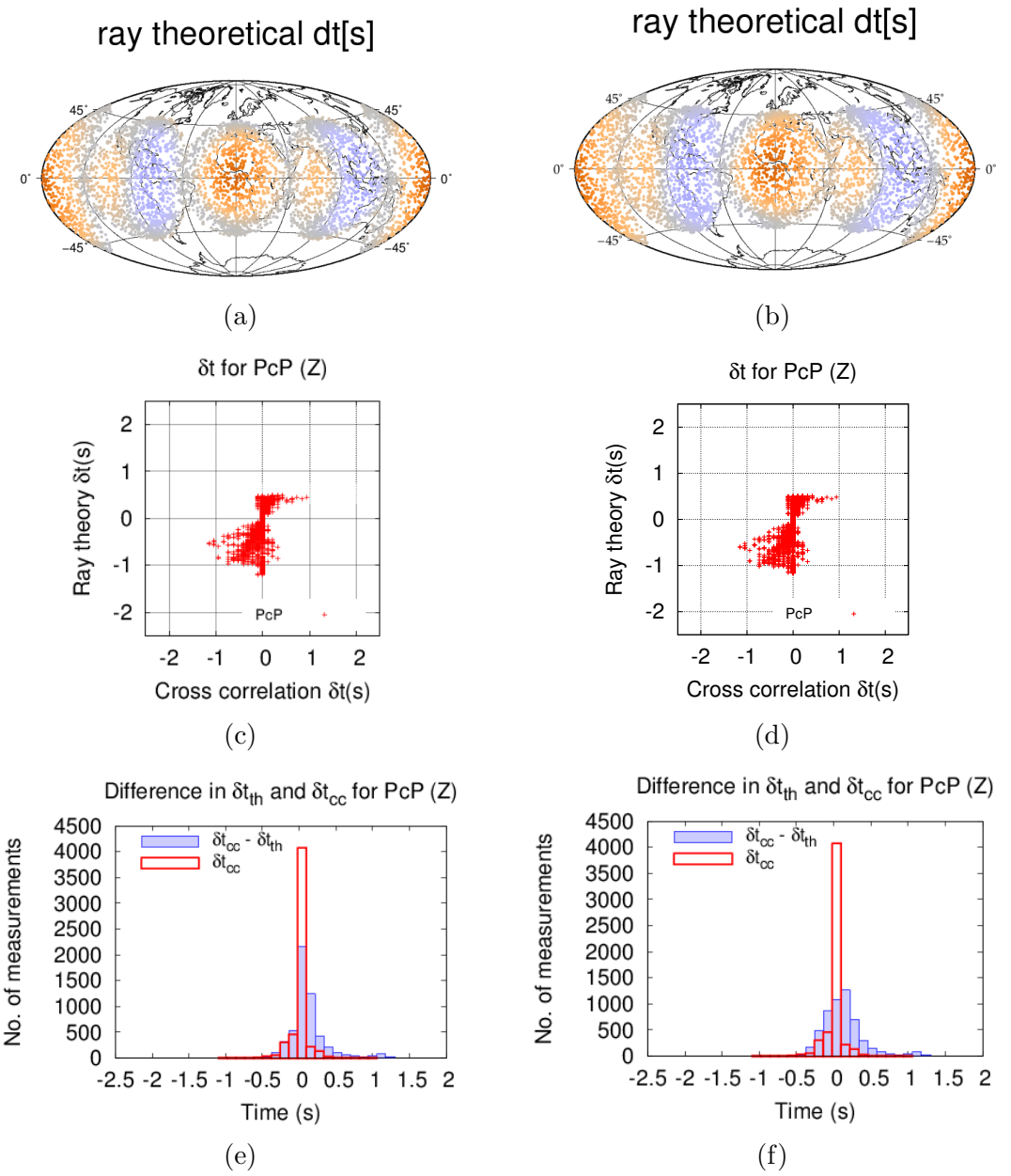

Figure 36: Figure 36a shows the geographical distribution of bouncepoints that are sampled by PcP. The colour of the dot indicates the ray theoretical delays predicted using ray theoretical predictions for delays calculated via the polynomial fit from TauP. Figure 36b shows the same map for delays calculated using equation 1. Figure 36c shows the same scatter plot as Figure 15, where the ray theoretical predictions for delays are calculated via the polynomial fit. Figure 36d shows the same scatter plot but for ray theoretical predictions calculated using equation 1. Figure 36e is the same as Figure 16c, with δt_{th} calculated using the polynomial fit. Figure 36f shows the histogram for δt_{th} predicted using equation 36f.

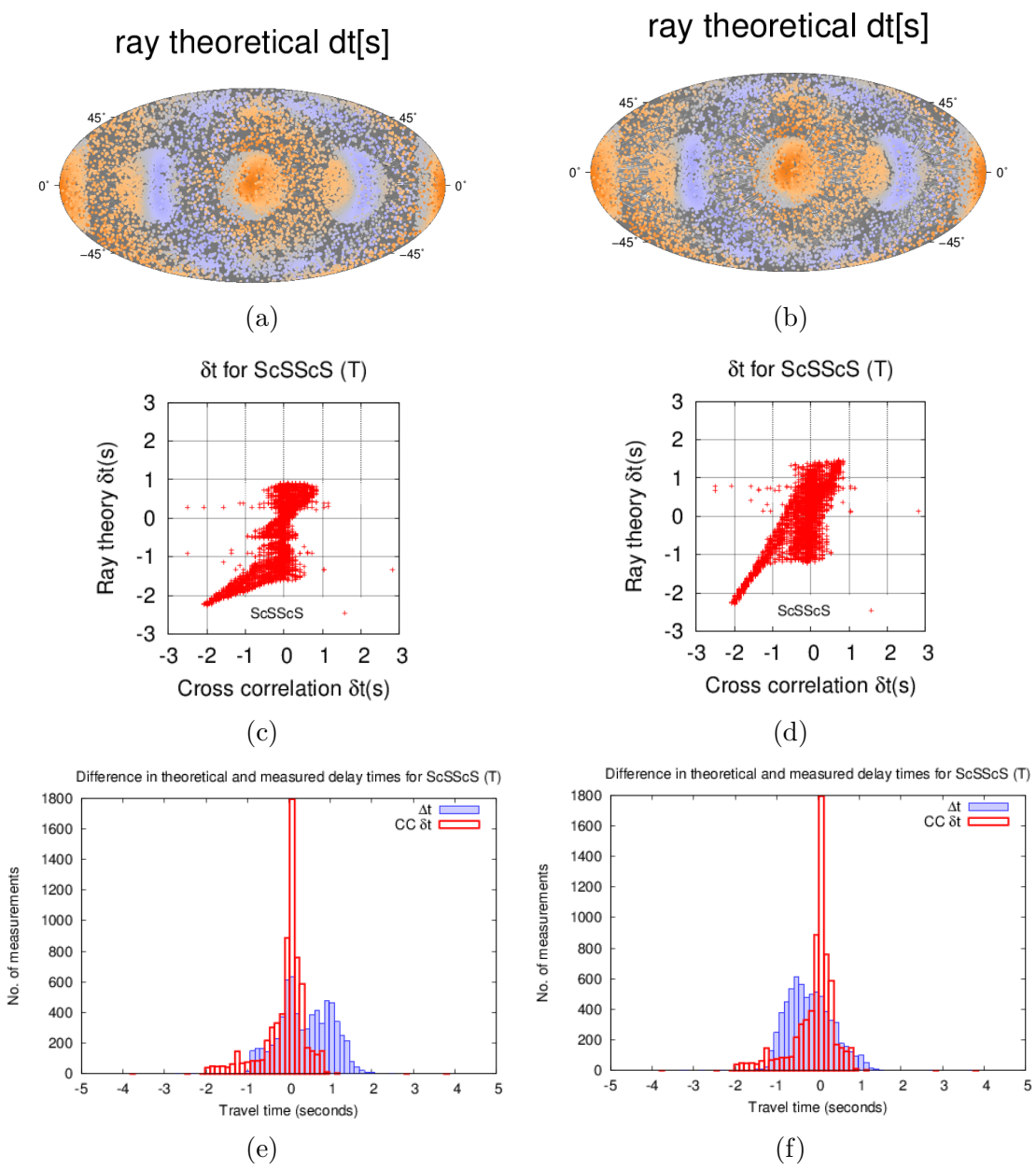

Figure 37: Figure 37a shows the geographical distribution of bouncepoints that are sampled by ScSScS. The colour of the dot indicates the ray theoretical delays predicted using ray theoretical predictions for delays calculated via the polynomial fit from TauP. Figure 37b shows the same map for delays calculated using equation 1. Figure 37c shows the same scatter plot as Figure 20, where the ray theoretical predictions for delays are calculated via the polynomial fit. Figure 37d shows the same scatter plot but for ray theoretical predictions calculated using equation 1. Figures 37e and 37f show the histograms for Δt, the difference between delays measured from cross-correlations and the delays predicted from ray theory.

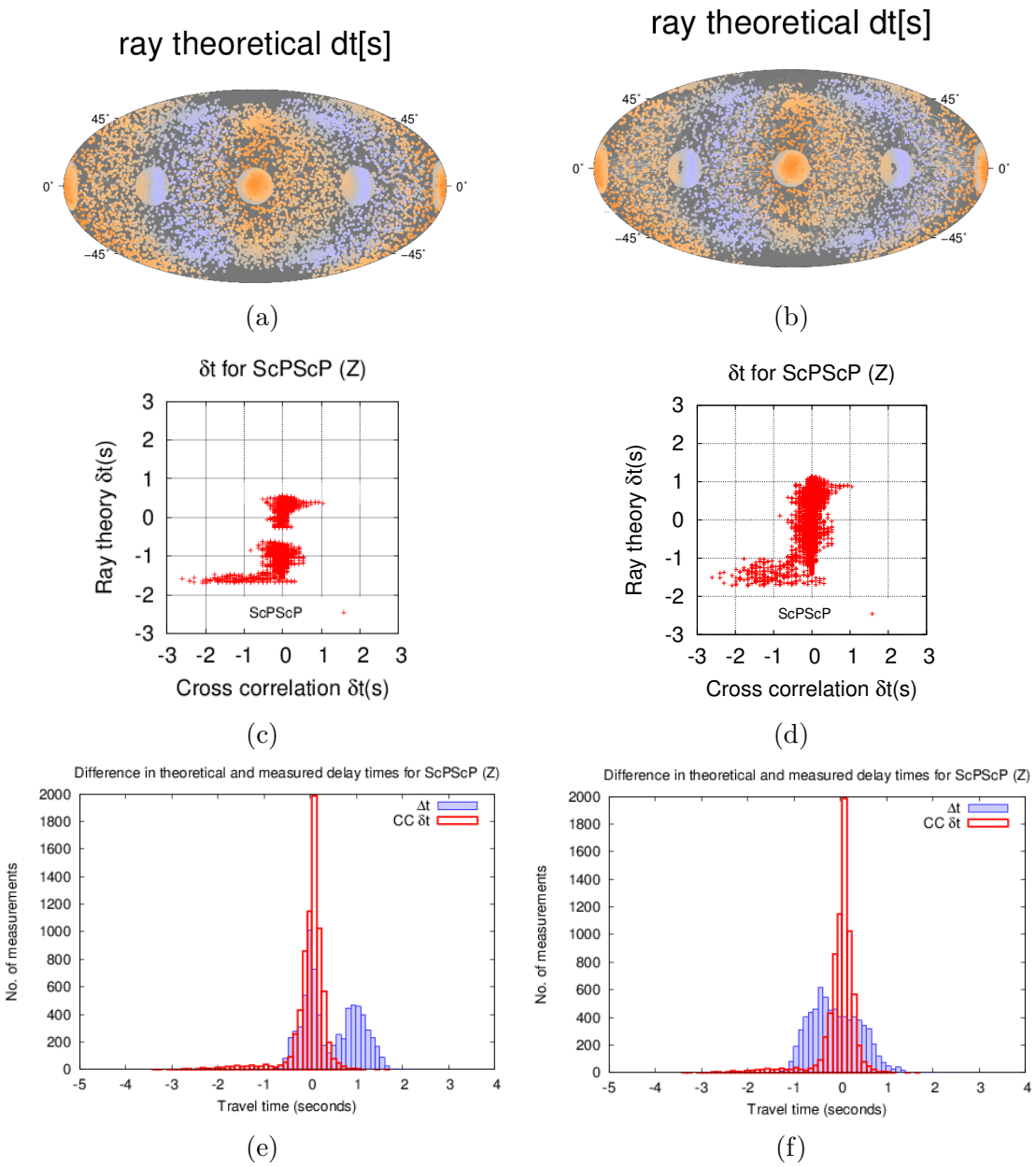

Figure 38: Same as Figure 37, but for ScPScP

D Z-components of seismograms for an explosive source

The following Z-components of seismograms show the development of the seismic phases created by an explosive source in an attenuated medium. For each figure, the top graph shows the seismogram of PREM and PREM+TOPO, which overlap when the phases have similar waveforms and arrival times. The bottom figure shows the difference between PREM+TOPO and PREM as a function of time. The epicentral distances as well as the exact arrival time of the main phases are given in the figure captions.

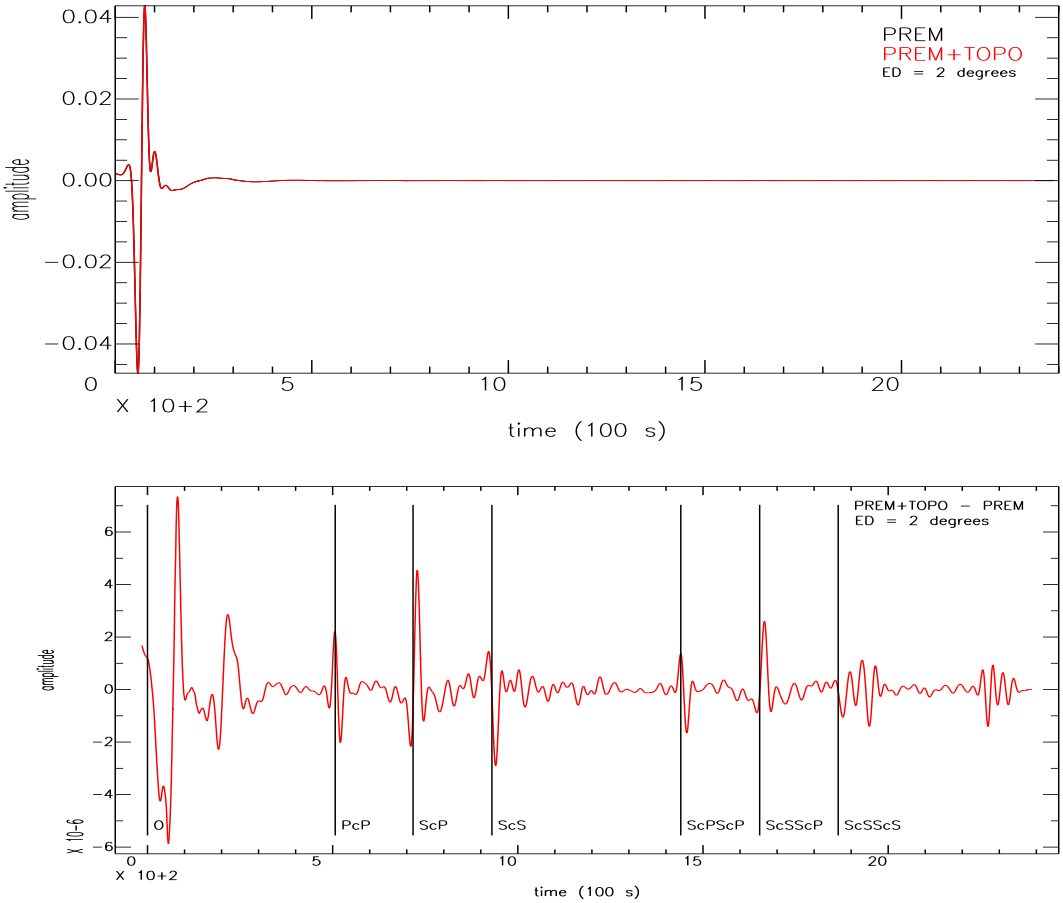

Figure 39: Station=1318, distance= 2°, P=33 s, PP=40 s, PPP=44 s, PcP=507 s, ScP=717 s, PKiKP=989 s, PcPPcP=1017 s

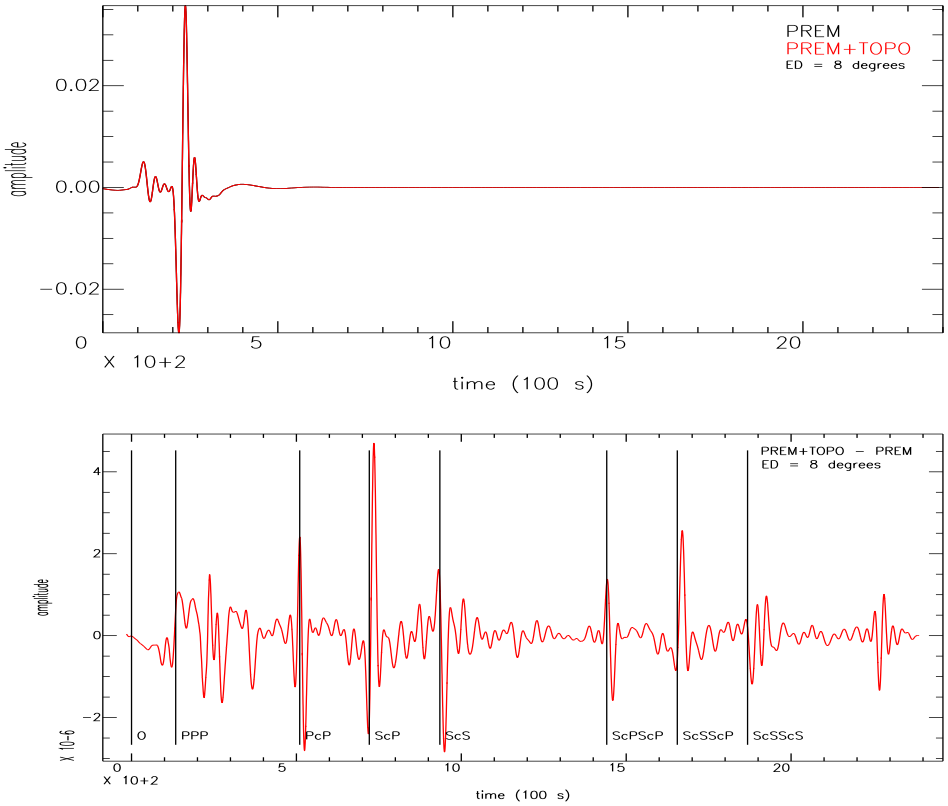

Figure 40: Station=1294, distance= 8°, P=110 s, PP=130 s, PPP=134 s, PcP=510 s, ScP=721 s, PKiKP=989 s, PcPPcP=1019 s

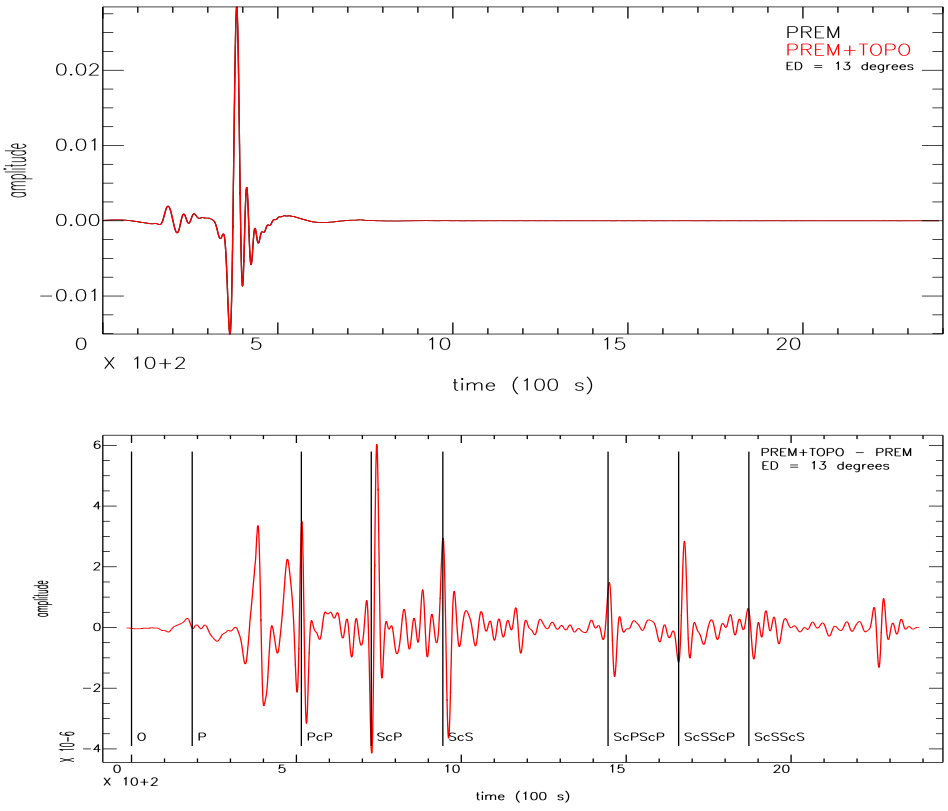

Figure 41: Station=1201, distance= 13°, P=184 s, PP=204 s, PPP=212 s, PcP=515 s, ScP=727 s, PKiKP=331 s, PcPPcP=1021 s

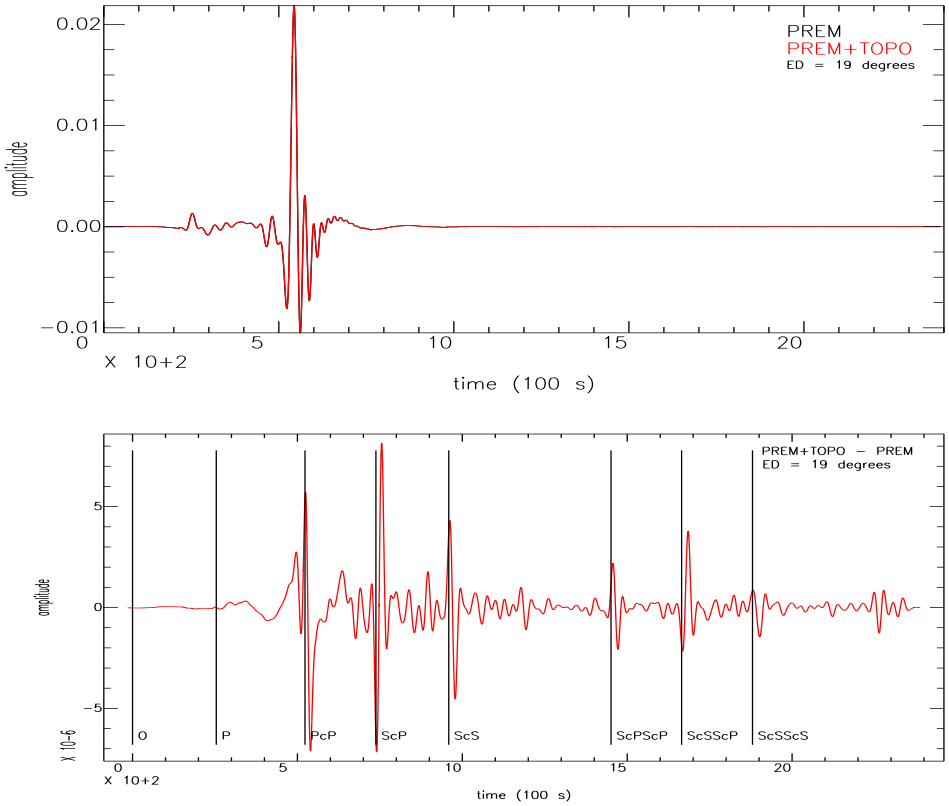

Figure 42: Station=1374, distance= 19°, P=254 s, PP=279 s, PPP=293 s, PcP=523 s, ScP=738 s, PKiKP=993 s, PcPPcP=1026 s

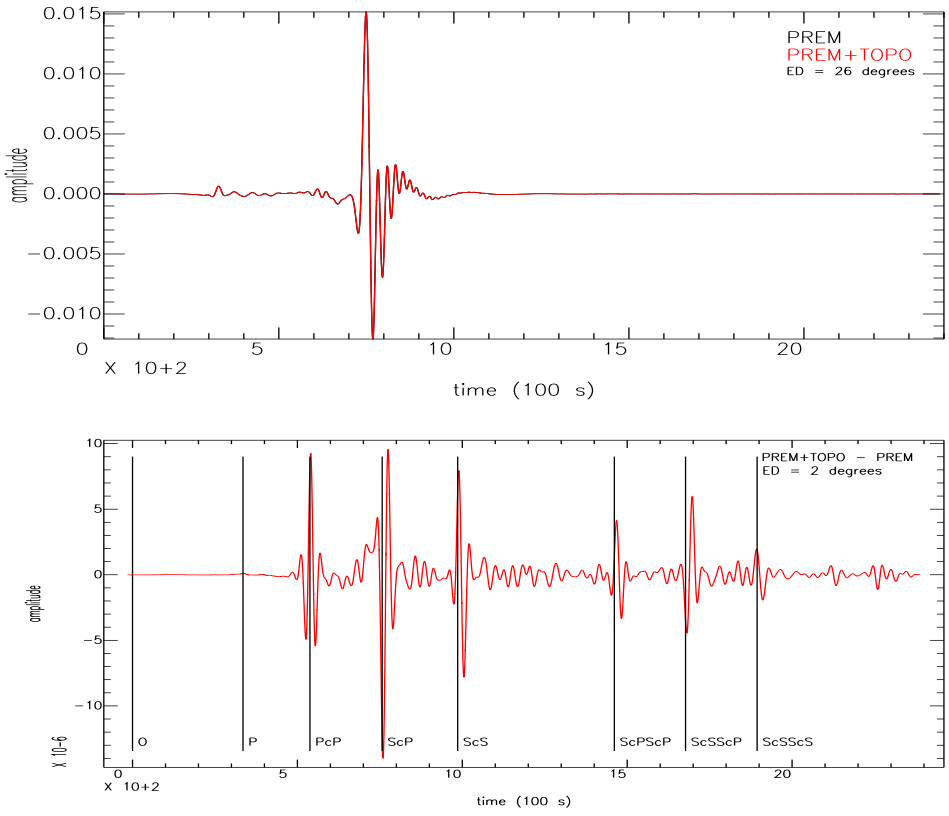

Figure 43: Station=1866, distance= 26°, P=335 s, PP=371 s, PPP=392 s, PcP=538 s, ScP=757 s, PKiKP=996 s, PcPPcP=1033 s

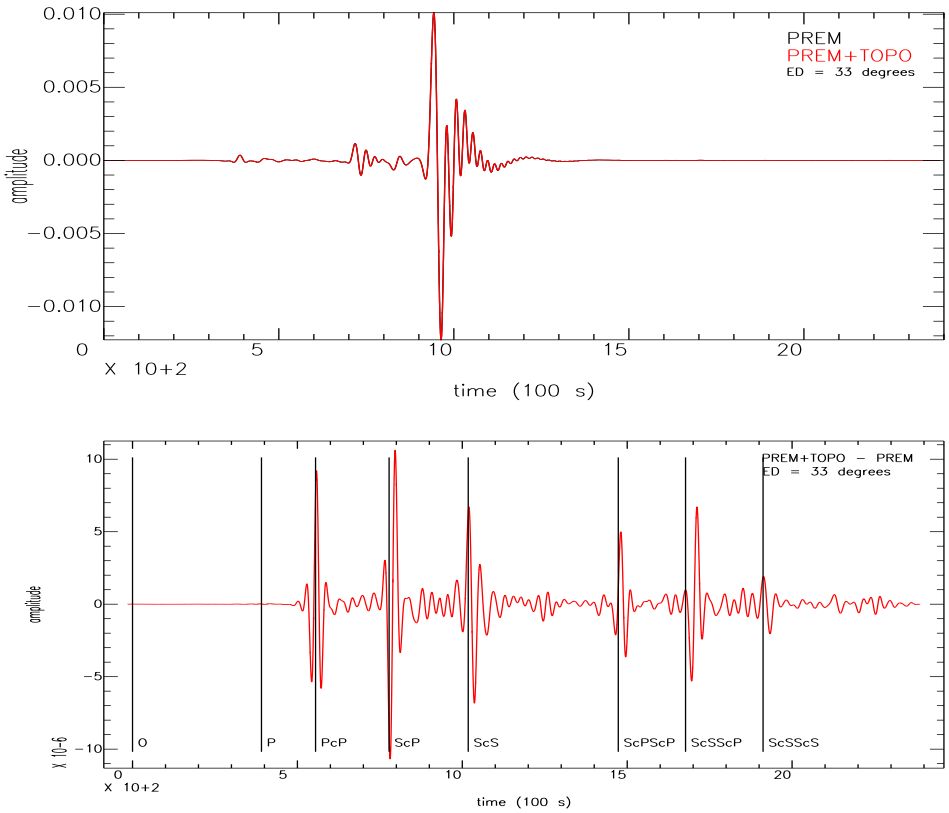

Figure 44: Station=1307, distance= 33°, P=391 s, PP=456 s, PPP=481 s, PcP=555 s, ScP=778 s, PKiKP=1001 s, PcPPcP=1043 s

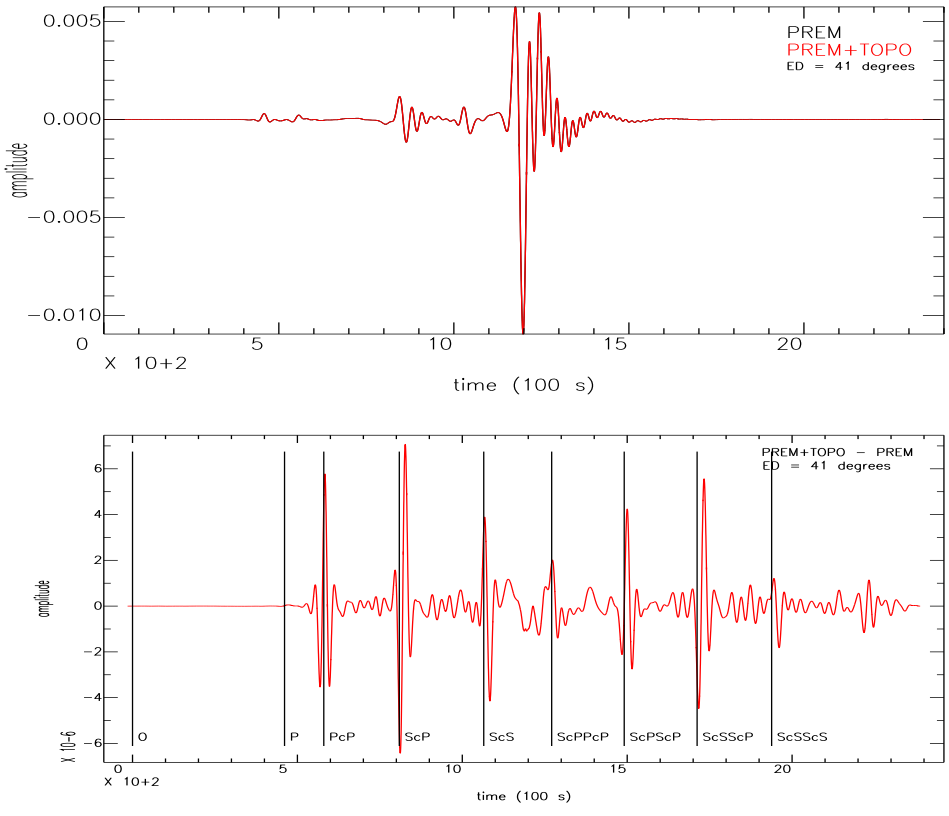

Figure 45: Station=1327, distance= 41°, P=461, PP=558 s, PPP=584 s, PcP=580 s, ScP=809 s, PKiKP=1007 s, PcPPcP=1057 s

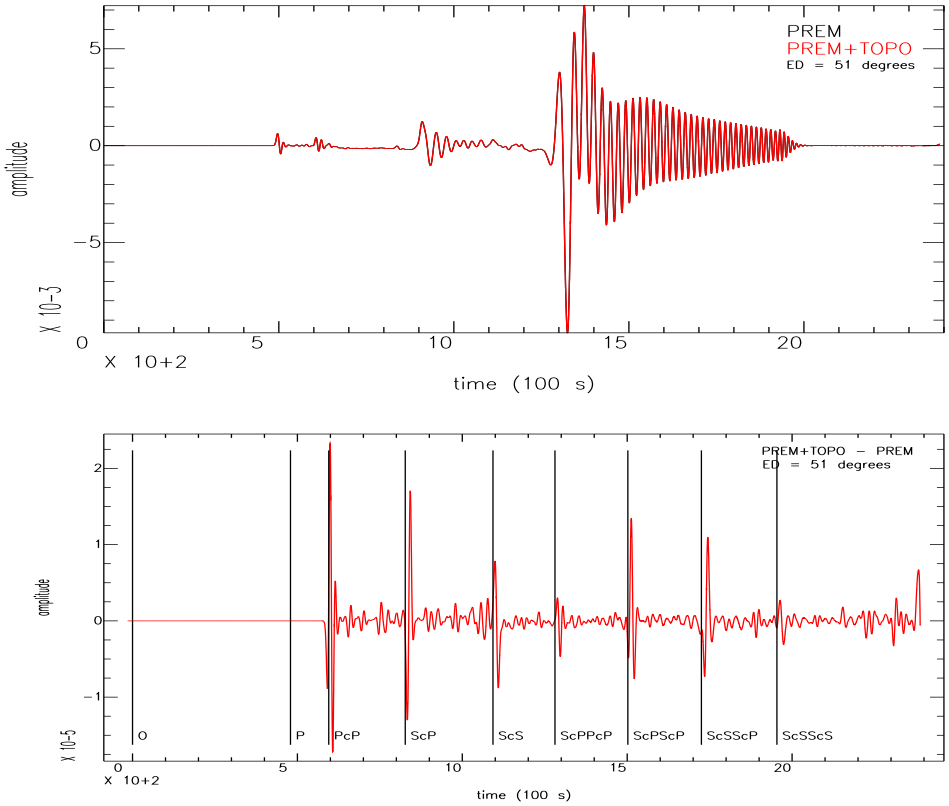

Figure 46: Station=1392, distance= 51°, P=479, PP=605 s, PPP=640 s, PcP=595 s, ScP=827 s, PKiKP=1011 s, PcPPcP=1066 s

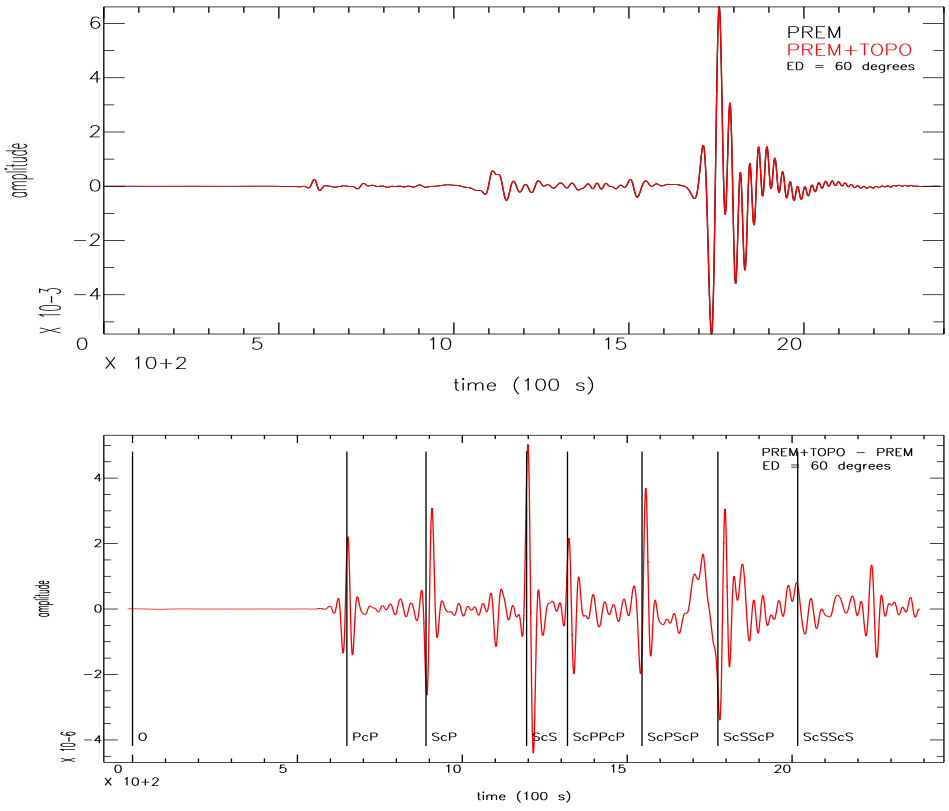

Figure 47: Station=1181, distance= 60°, P=605, PP=738 s, PPP=820 s, PcP=650 s, ScP=890 s, PKiKP=1028 s, PcPPcP=1099 s

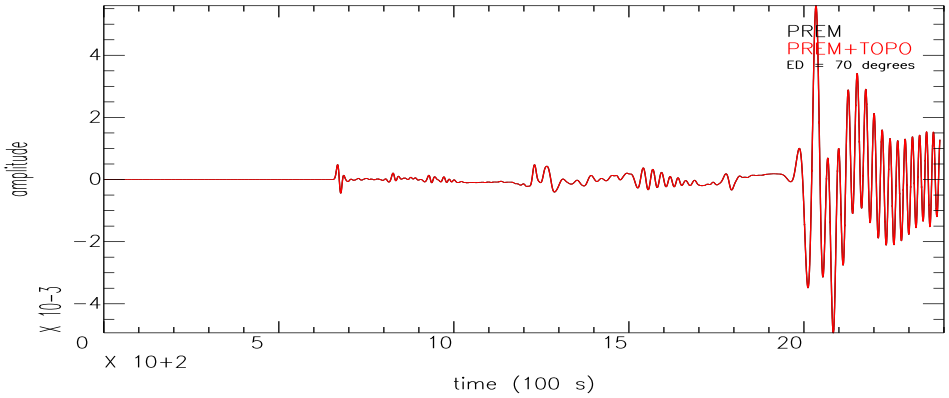

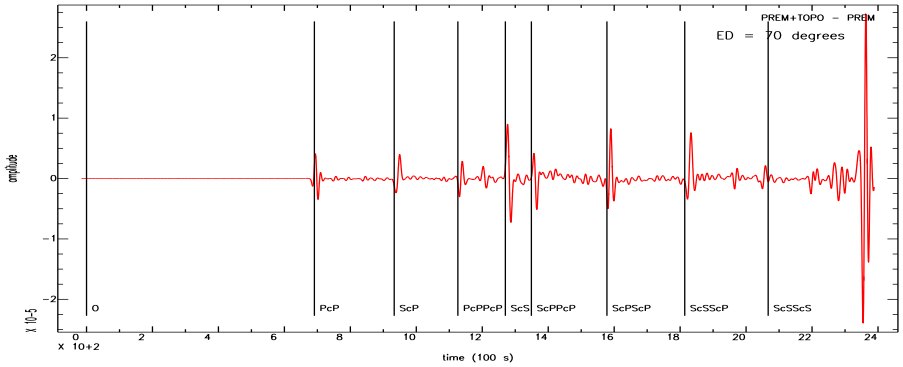

Figure 48: Station=1140, distance= 70°, P=669, PP=823 s, PPP=931 s, PcP=691 s, PKiKP=1041 s, PcPPcP=1126 s

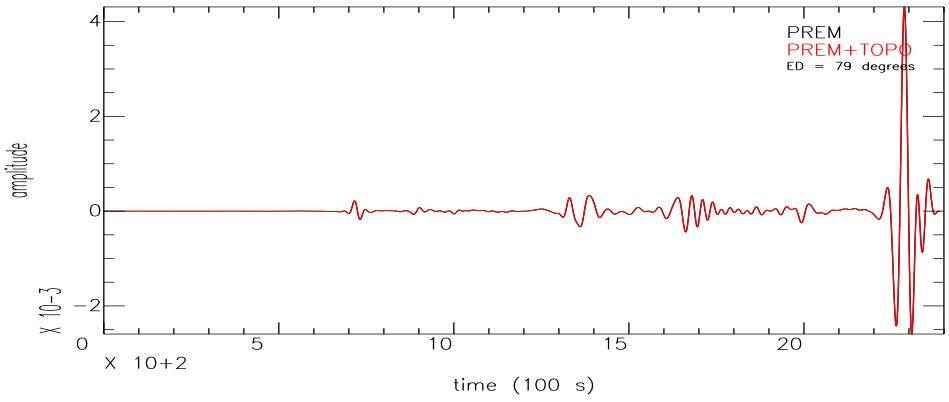

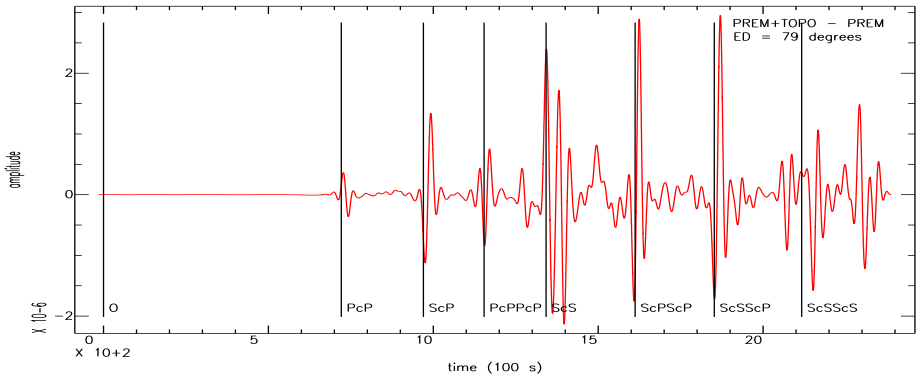

Figure 49: Station=1165, distance= 79°, P=721, PP=899 s, PPP=1007 s, PcP=729 s, PKiKP=1054 s, PcPPcP=1154 s, PKKP=1852 s

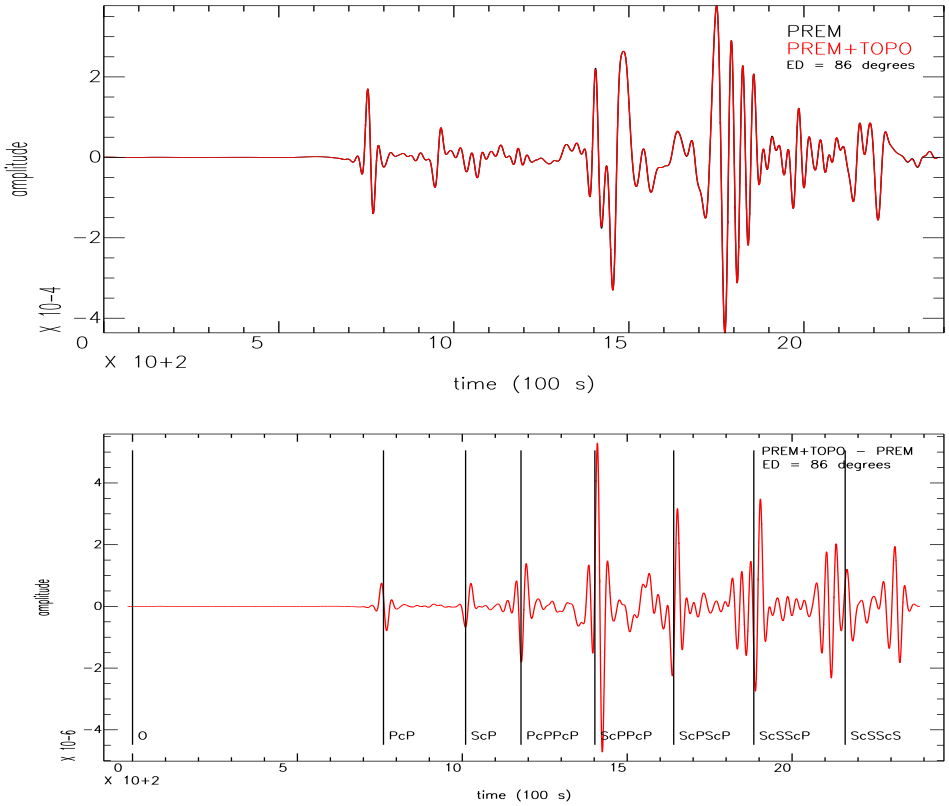

Figure 50: Station=1105, distance= 86°, P=758, PP=959 s, PPP=1073 s, PcP=761 s, PKiKP=1066 s, PcPPcP=1178 s, PKKP=1836 s, SKKP=2052 s, PKPPcP=2120 s

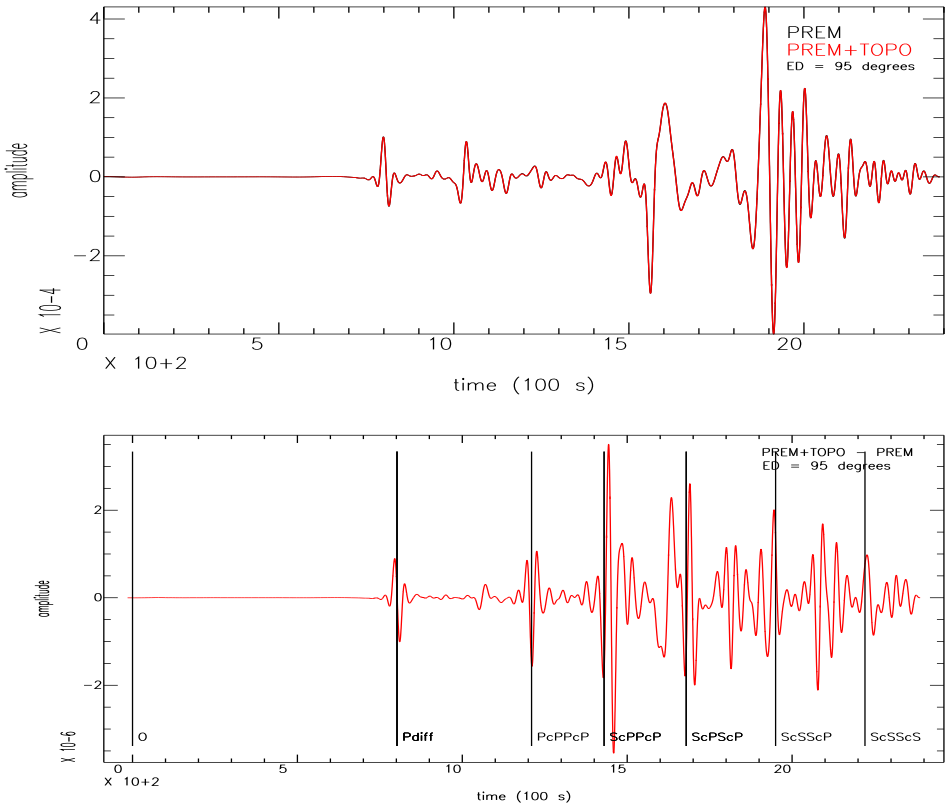

Figure 51: Station=1015, distance= 95°, Pdiff=802 s, PP=1033 s, PKiKP=1081 s, PPP=1155 s, PcPPcP=1210 s, PKKP=1812 s, SKKP=2031 s, PKPPcP=2079 s

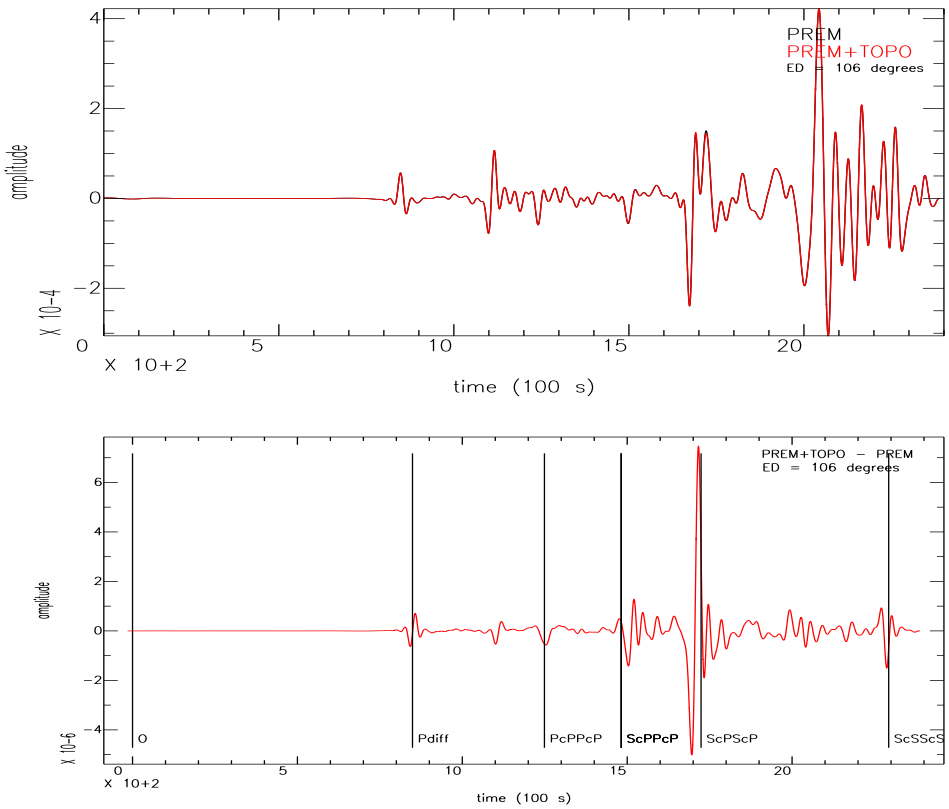

Figure 52: Station=1076, distance= 106°, Pdiff=849 s, PP=1112 s, PKiKP=1100 s, PPP=1246 s, PcPPcP=1249 s, PKJKP=1753 s, PKKP=1782 s, SKKP=2003 s, PKPPcP=2033 s

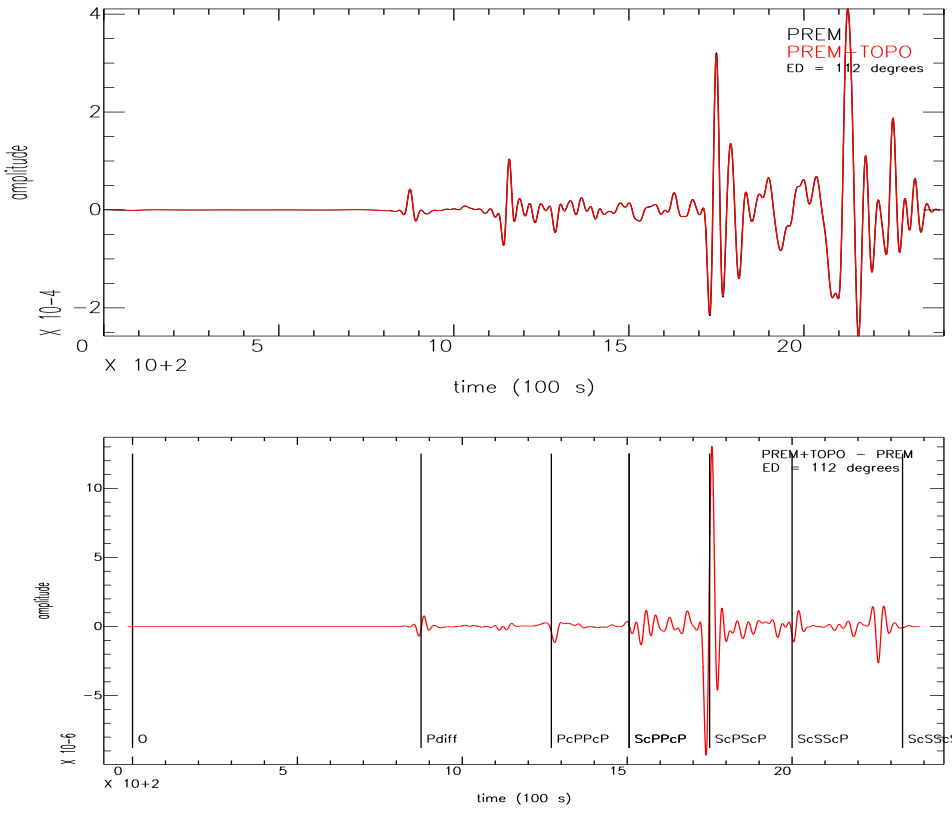

Figure 53: Station=1082, distance= 112°, Pdiff=875 s, PP=1155 s, PKiKP=1111 s, PPP=1296 s, PcPPcP=1270 s, PKJKP=1742 s, PKKP=1763 s, SKKP=1987 s, PKPPcP=2007 s

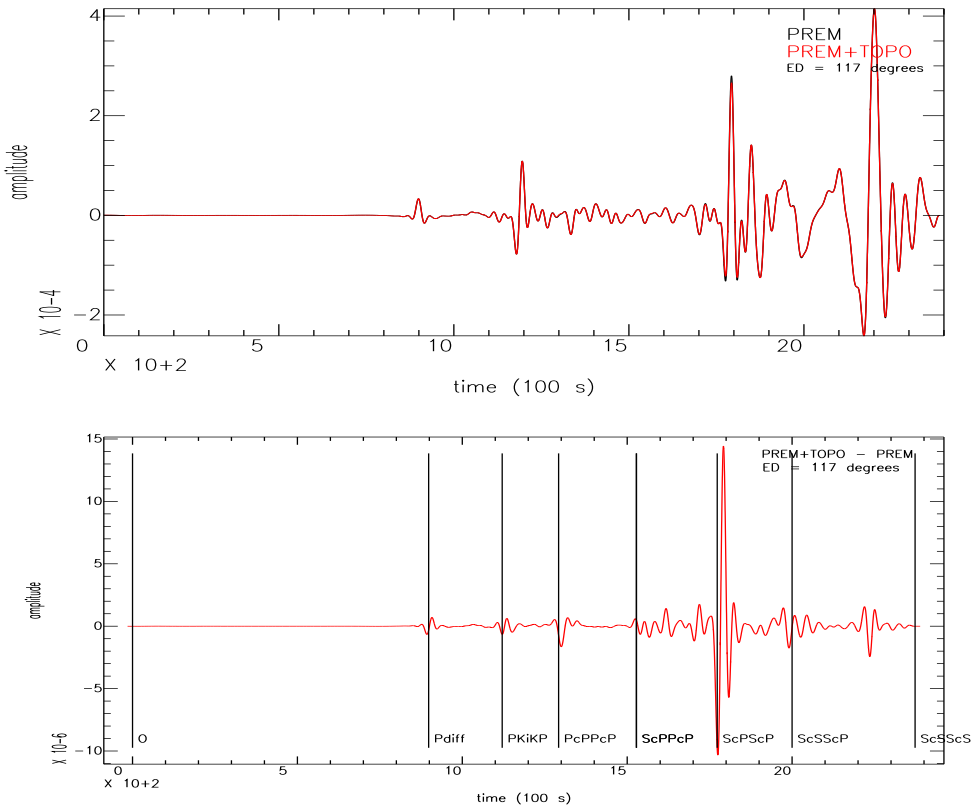

Figure 54: Station=1019, distance= 117°, Pdiff=898 s, PP=1192 s, PKIKP=1121 s, PPP=1341 s, PcPPcP=1292 s, PKJKP=1732 s, PKKP=1745 s, SKKP=1971 s, PKPPcP=1984 s

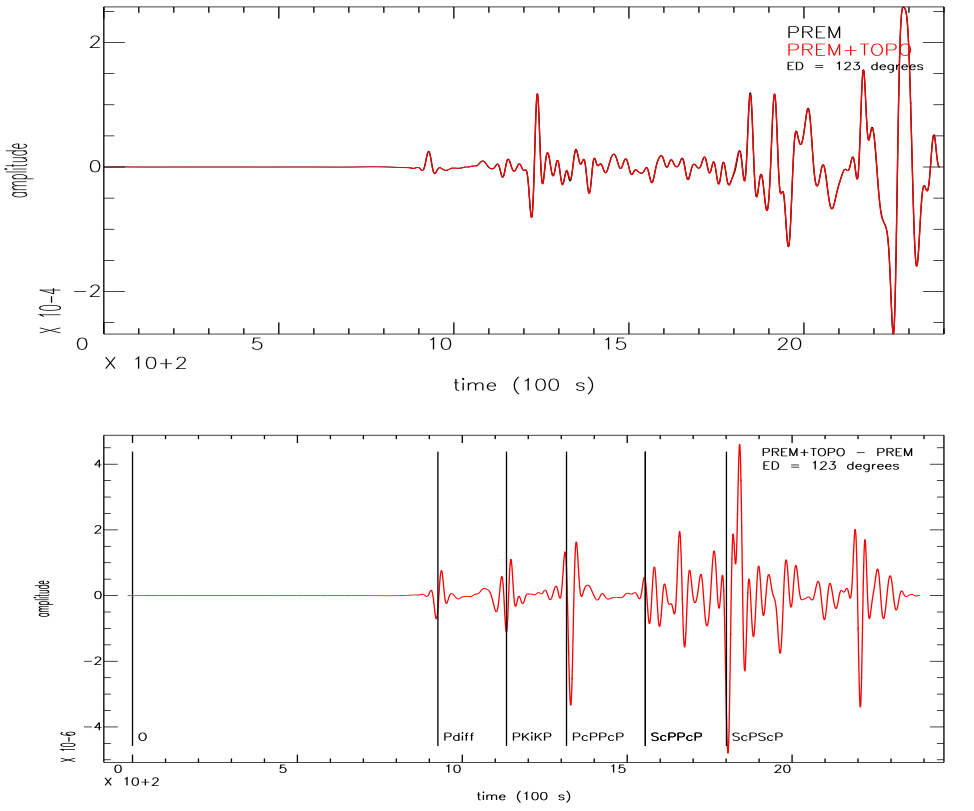

Figure 55: Station=1037, distance= 123°, Pdiff=926 s, PP=1235 s, PKIKP=1134 s, PPP=1393 s, PcPPcP=1371 s, PKJKP=1721 s, PKKP=1722 s, SKKP=1951 s, PKPPcP=1957 s

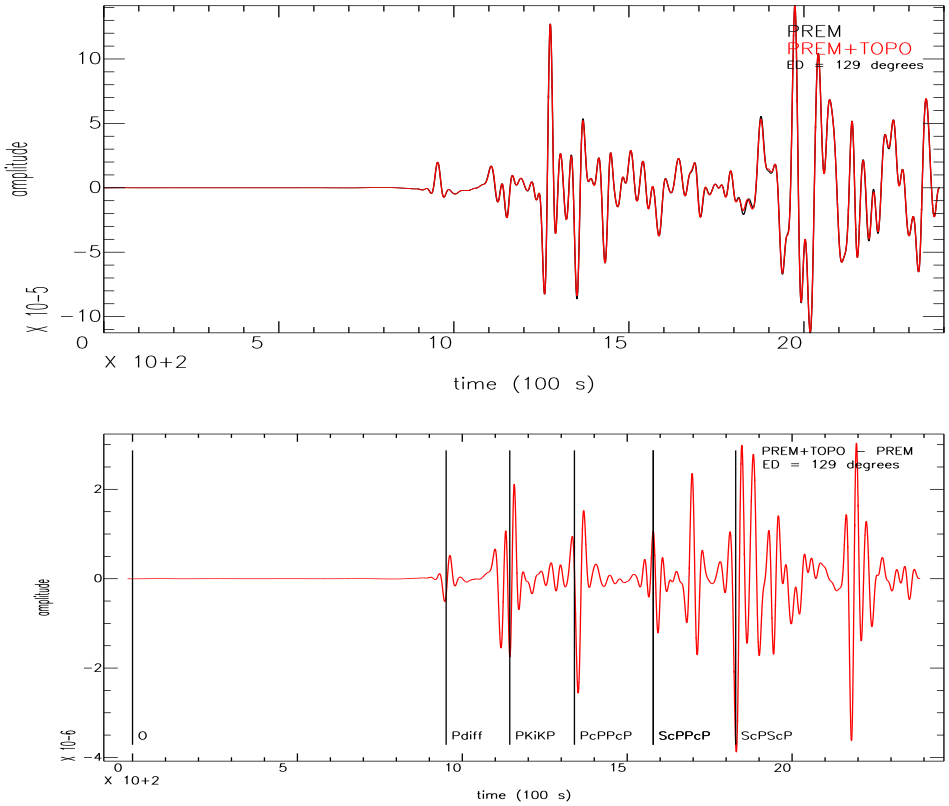

Figure 56: Station=1119, distance= 129°, Pdiff=951 s, PP=1272 s, PKIKP=1144 s, PKiKP=11145 s, PPP=1439 s, PcPPcP=1340 s, PKJKP=1721 s, SKP=1347 s, SKKP=1931 s, PKPPcP=1932 s

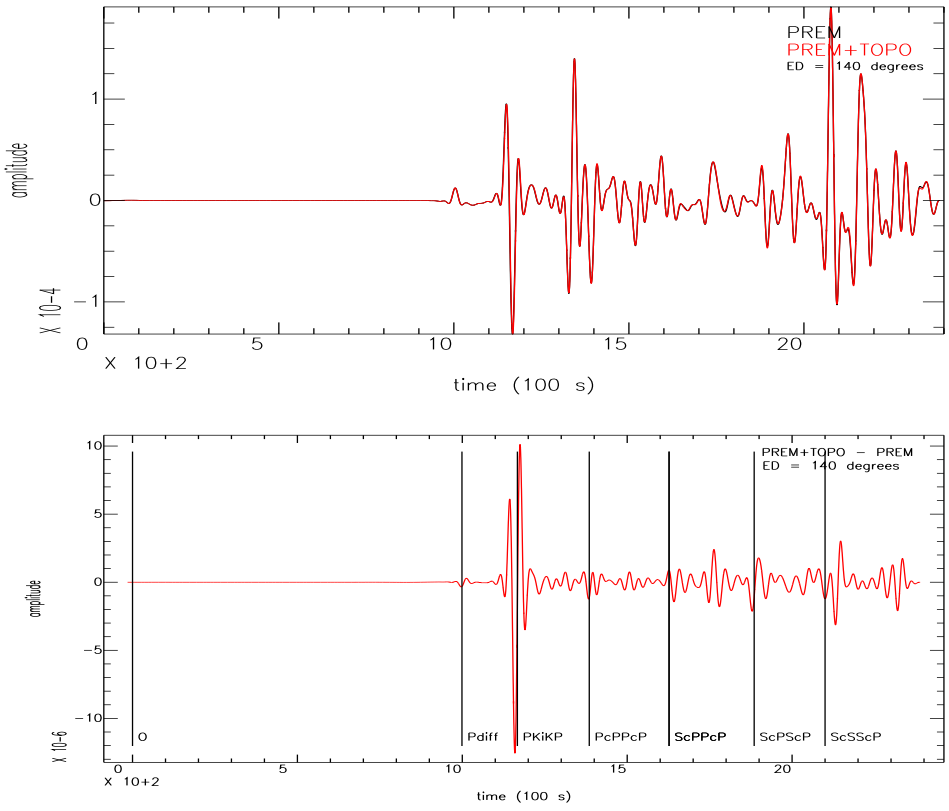

Figure 57: Station=1221, distance= 140°, Pdiff=999 s, PP=1341 s, PKIKP=1165 s, PKiKP=1167 s, PPP=1525 s, PcPPcP=1385 s, PKJKP=1695 s, SKP=1380 s, SKKP=1891 s, PKPPcP=1886 s

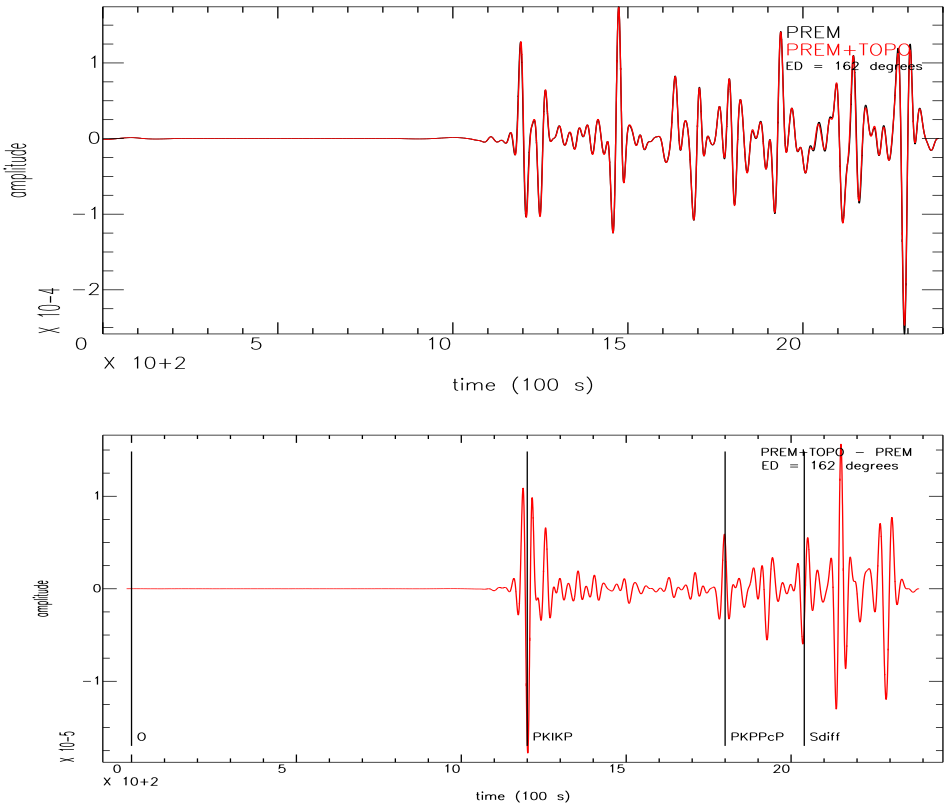

Figure 58: Station=1005, distance= 162°, PP=1470 s, PKIKP=1199, PPP=1696 s, PcPPcP=1481 s, PKJKP=1671 s, PKP=1247 s, PKPPcP=1796 s

E T-components of seismograms for shear source

The following T-components of seismograms show the development of the seismic phases created by a shear source in a nonattenuated medium. For each figure, the top graph shows the seismogram of PREM and PREM+TOPO, which overlap when the phases have similar waveforms and arrival times. The bottom figure shows the difference between PREM+TOPO and PREM as a function of time. The epicentral distances as well as the exact arrival time of the main phases are given in the figure captions.

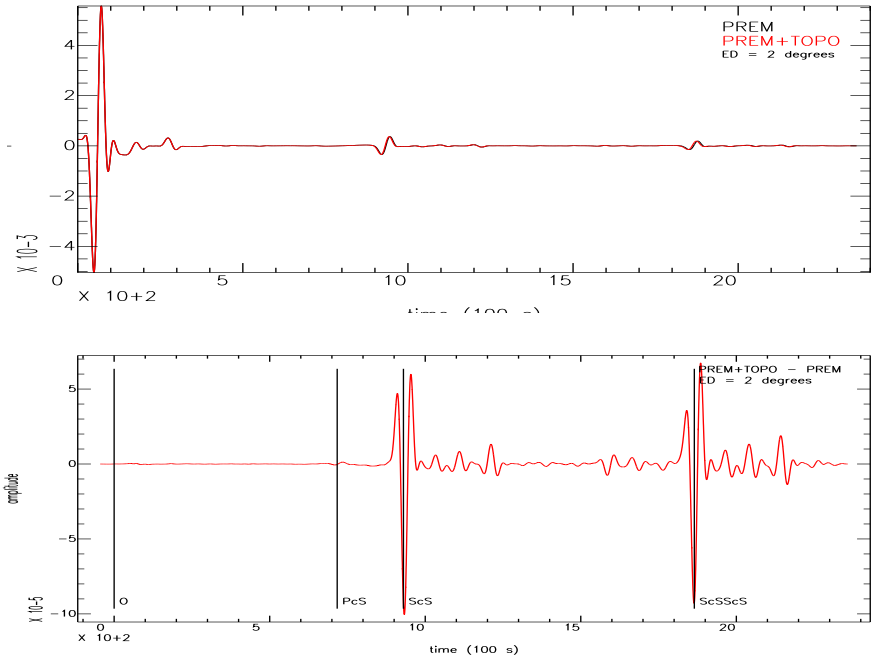

Figure 59: Station=1318, distance= 2°, S= 59 s, SSS= 76 s, PcS= 719 s, ScS= 930s, SKiKS= 1411 s, ScSScS=1865 s

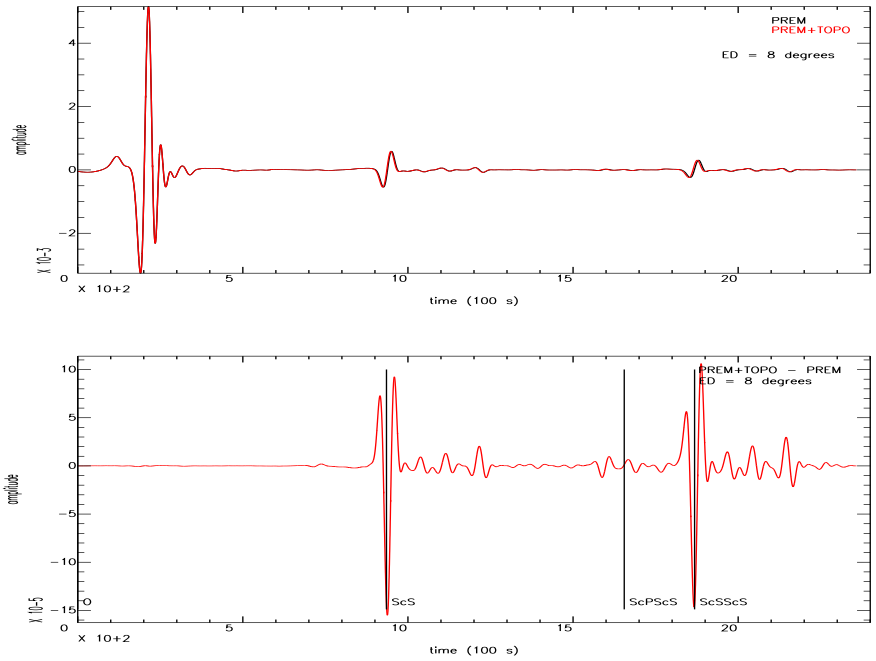

Figure 60: Station=1294, distance= 8°, S= 197 s, SSS= 215 s, PcS= 723 s, ScS= 935s, SKiKS= 1412 s, ScSScS=1868 s

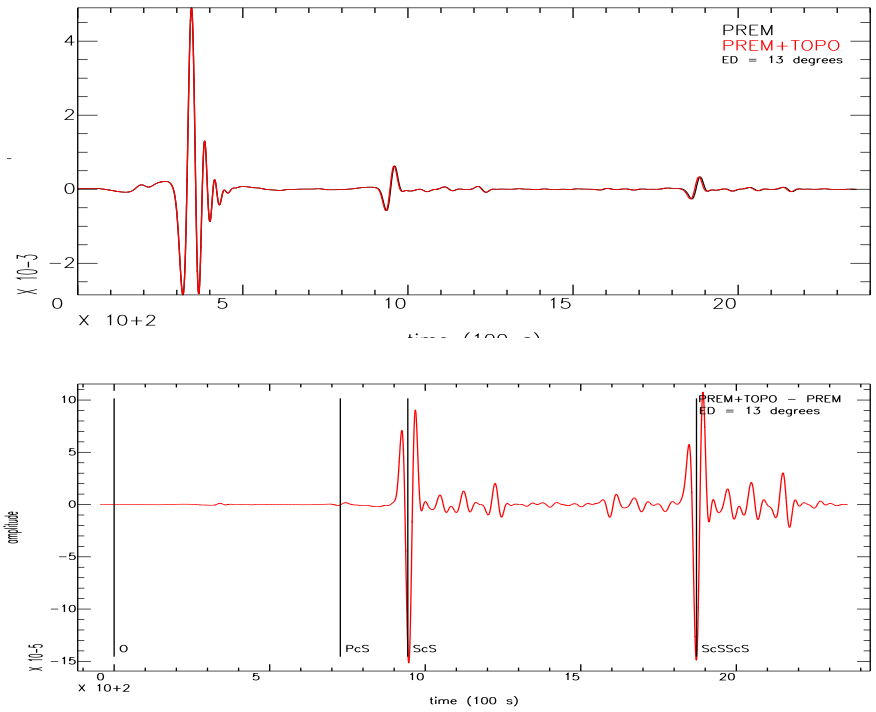

Figure 61: Station=1201, distance= 13°, S= 324 s, SSS= 342 s, PcS= 730 s, ScS= 944s, SKiKS= 1413 s, ScSScS=1872 s

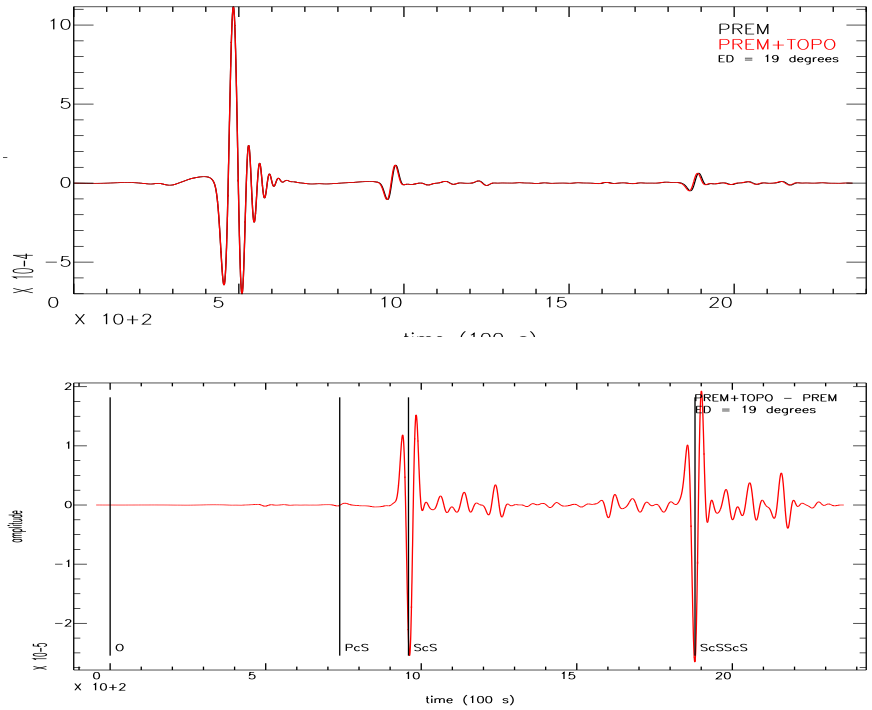

Figure 62: Station=1374, distance= 19°, S= 465 s, SSS= 482 s, PcS= 740 s, ScS= 959s, SKiKS= 1415 s, ScSScS=1880 s

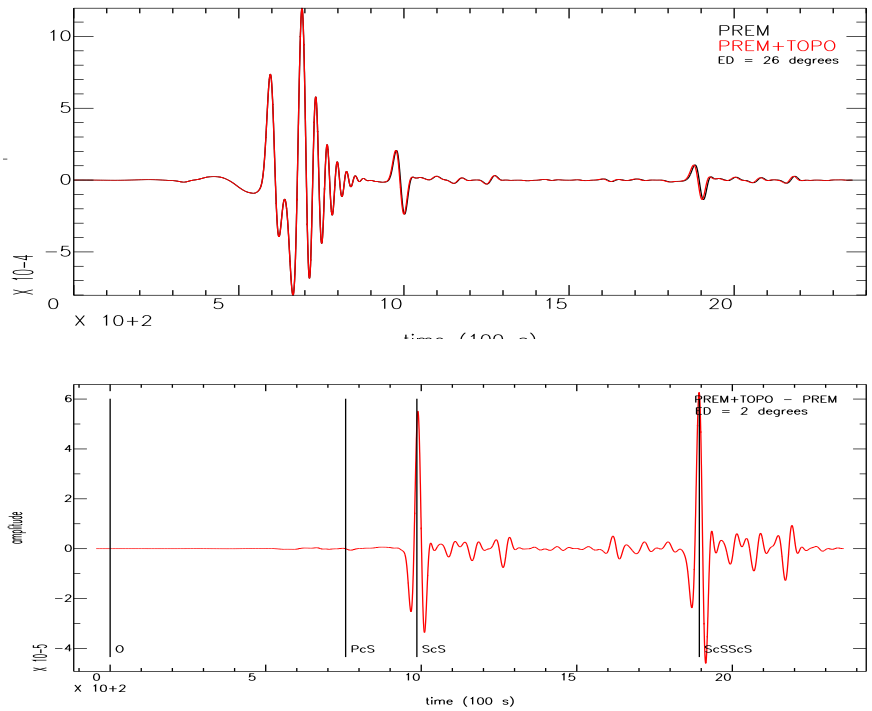

Figure 63: Station=1866, distance= 26°, S= 601 s, SSS= 662 s, PcS= 759 s, ScS= 986s, SKiKS= 1419 s, ScSScS=1894 s

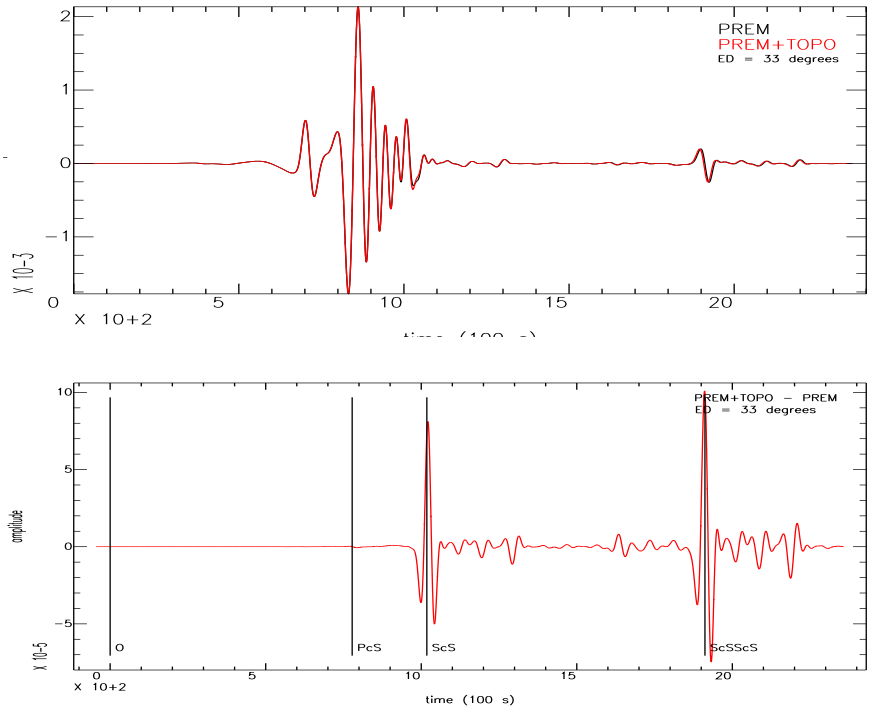

Figure 64: Station=1307, distance= 33°, S= 708 s, SSS= 831 s, PcS= 781 s, ScS=1018s, SKiKS= 1424 s, ScSScS=1912 s

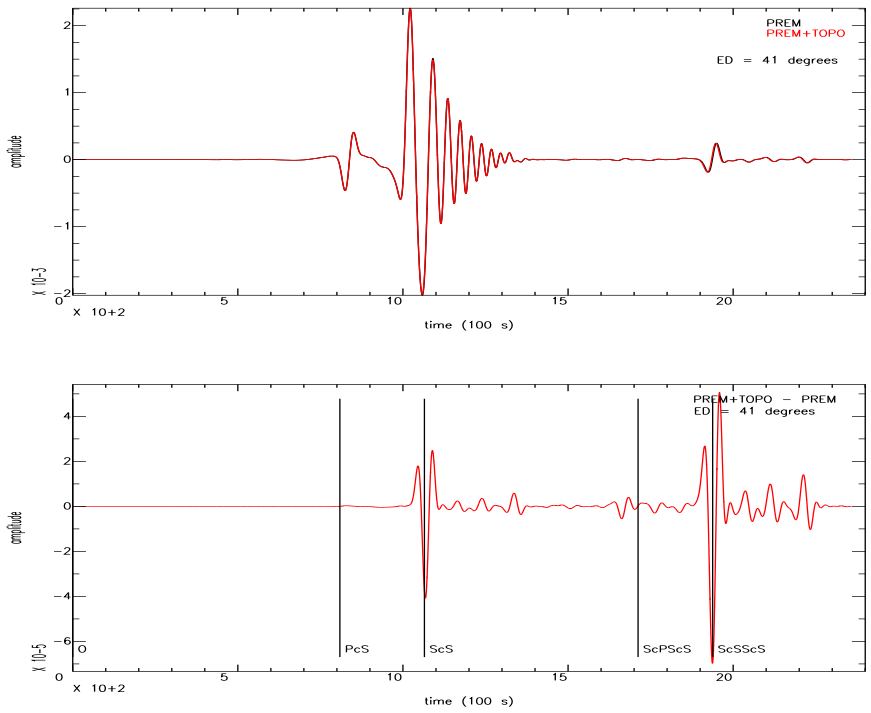

Figure 65: Station=1327, distance= 41°, S= 834 s, SSS= 1035 s, PcS= 811 s, ScS=1065s, SKiKS= 1432 s, ScSScS=1938 s

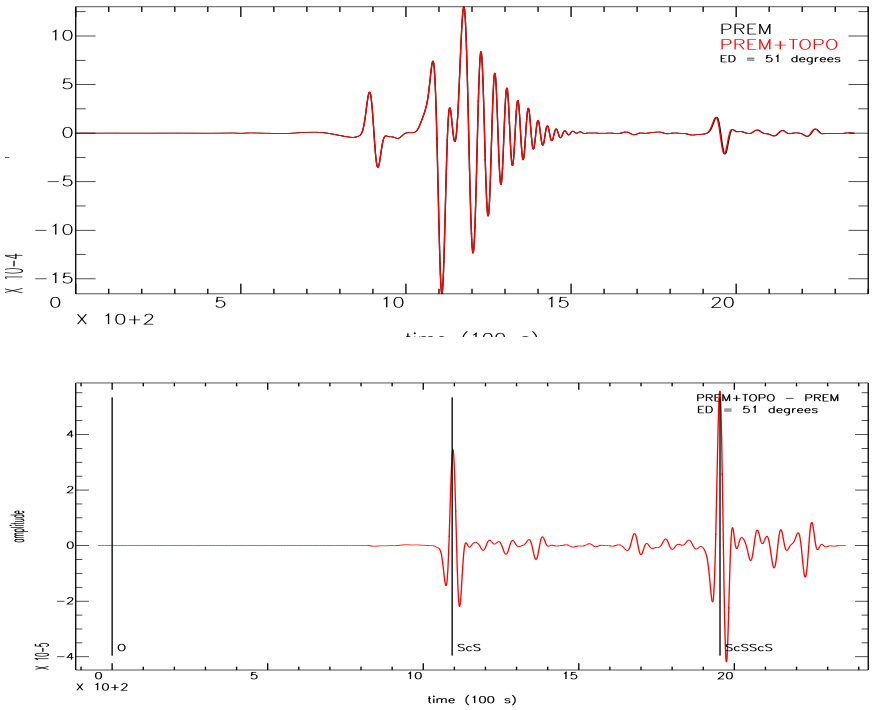

Figure 66: Station=1392, distance= 51°, S= 899 s, SSS= 1145 s, PcS= 829 s, ScS=1093s, SKiKS= 1436 s, ScSScS=1954 s

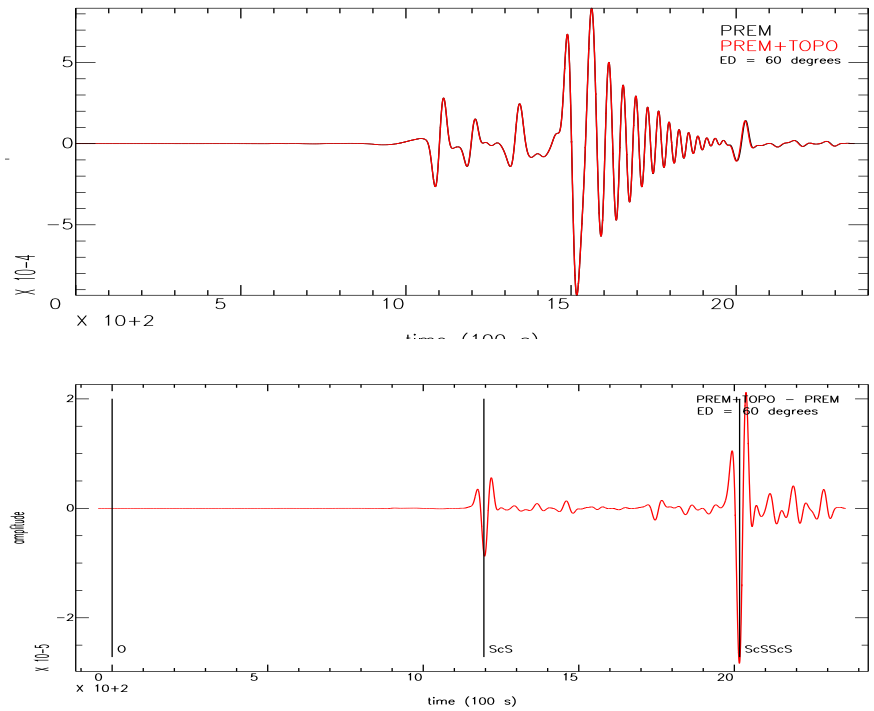

Figure 67: Station=1181, distance= 60°, S=1098 s, SSS= 1527 s, PcS= 893 s, ScS=1195s, SKiKS= 1454 s, ScSScS=2016 s

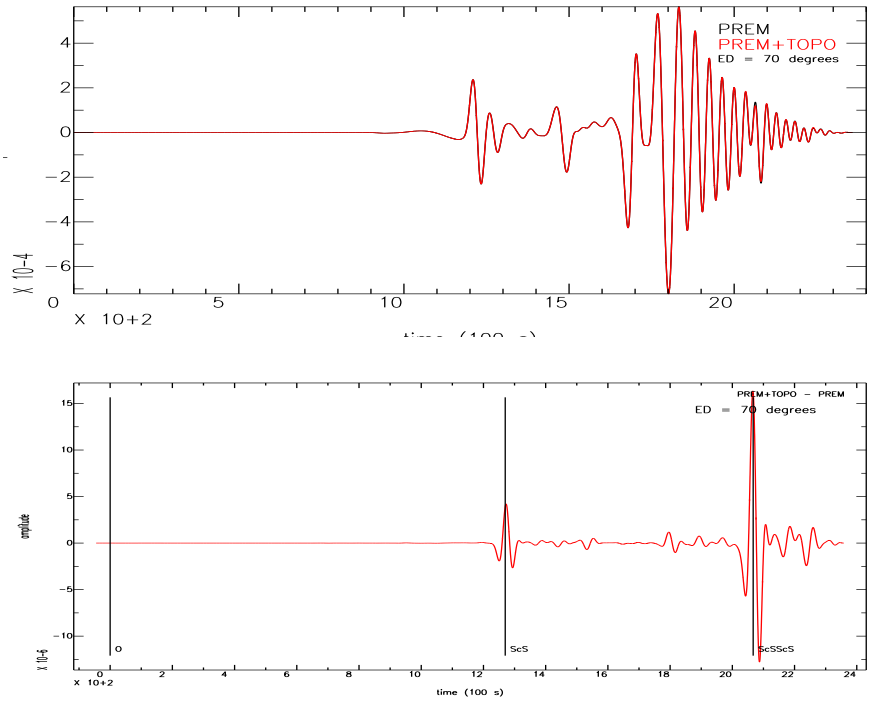

Figure 68: Station=1140, distance= 70°, S=1218 s, SSS= 1691 s, ScS=1270s, SKiKS= 1468 s, SKKS=1268 s, ScSScS=2066 s, SKS=1268

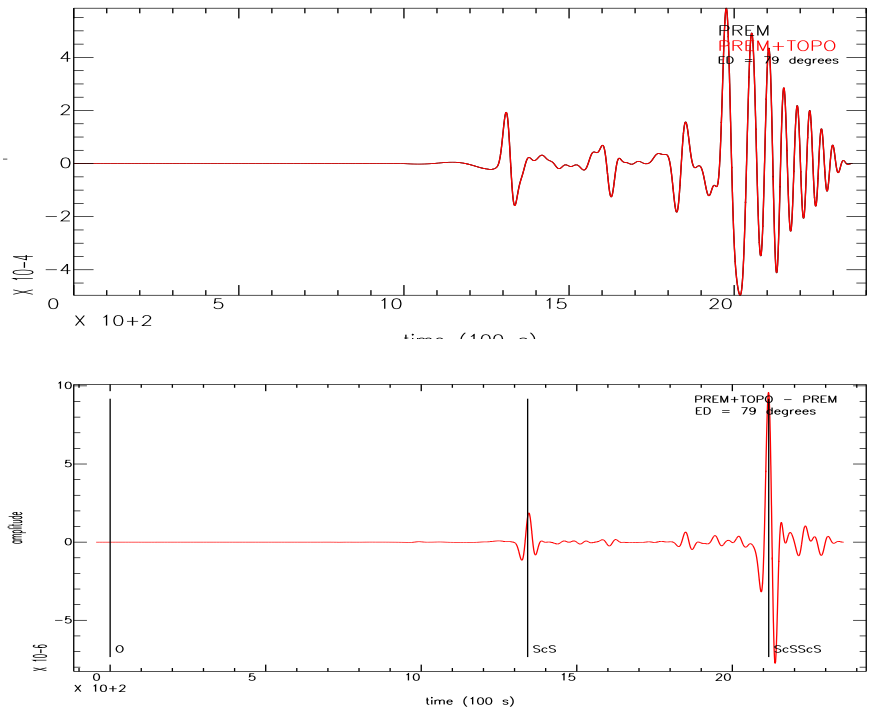

Figure 69: Station=1165, distance= 79°, S=1318 s, SSS= 1834 s, ScS=1342s, SKiKS= 1482 s, SKKS=1335 s, ScSScS=2117 s, SKS=1333

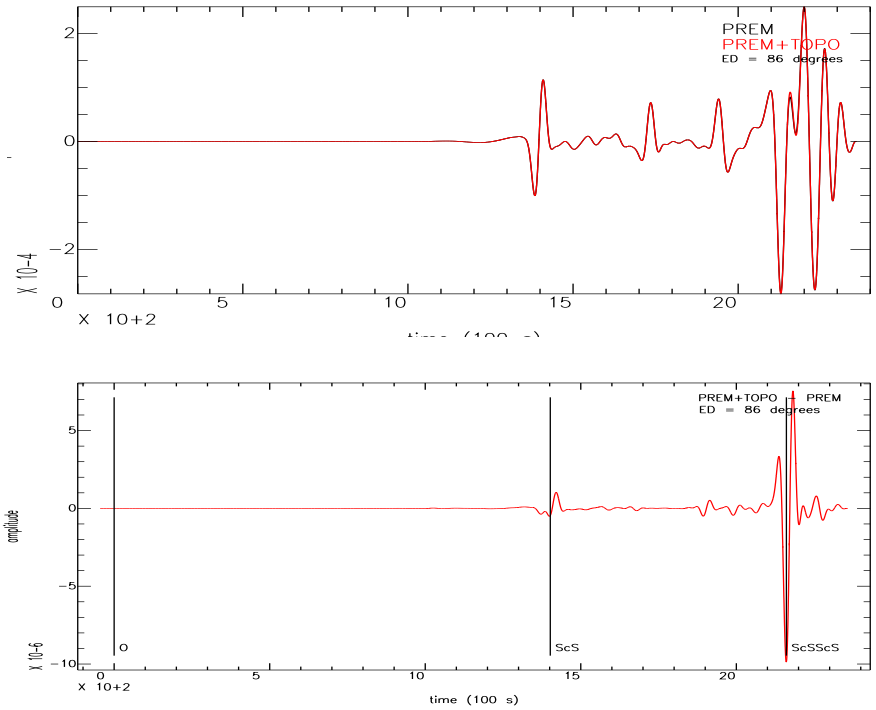

Figure 70: Station=1105, distance= 86°, S=1393 s, SSS= 1949 s, ScS=1402s, SKiKS= 1495 s, SKJKS=2225 s, PKKS= 2054 s, SKKS=1390 s, ScSScS=2161 s, SKS=1382

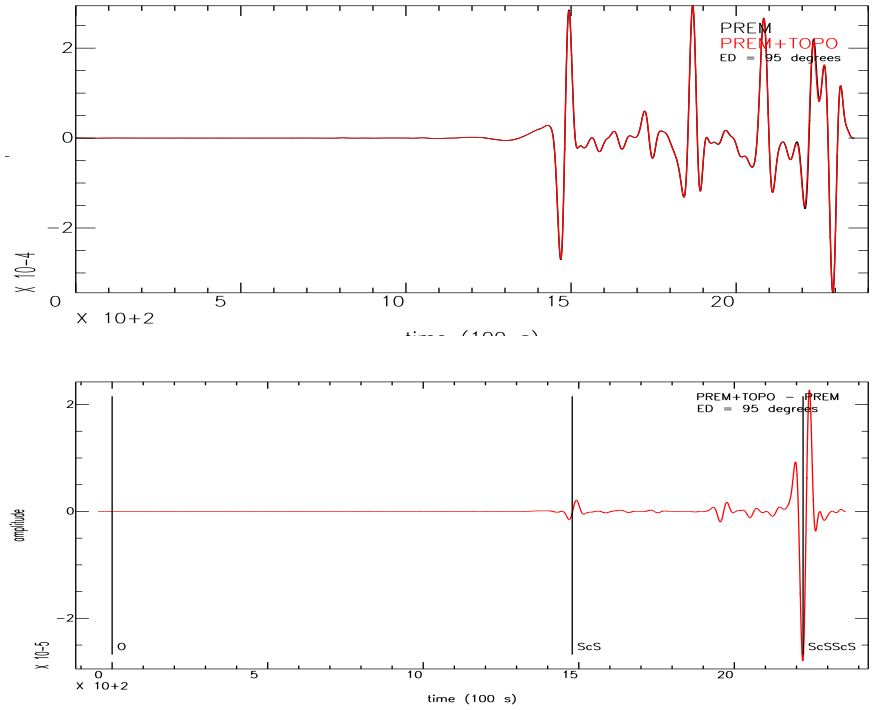

Figure 71: Station=1015, distance= 95°, S=1478 s, SSS= 2093 s, ScS=1479s, SKiKS= 1512 s, SKJKS=2206 s, PKKS= 2033 s, SKKS=1458 s, ScSScS=2221 s, SKS=1436

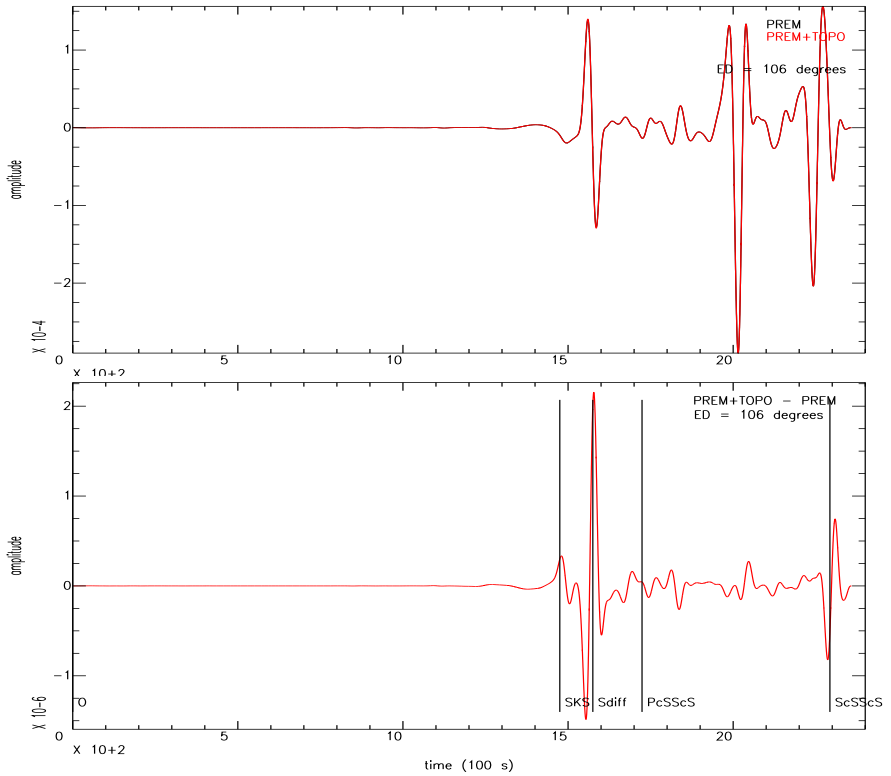

Figure 72: Station=1076, distance= 106°, SSS= 2256 s, SKiKS= 1532 s, SKIKS=1532 s, SKJKS=2184 s, PKKS= 2006 s, SKKS=1533 s, ScSScS=2293 s, Sdiff= 1567 s, SKS=1488

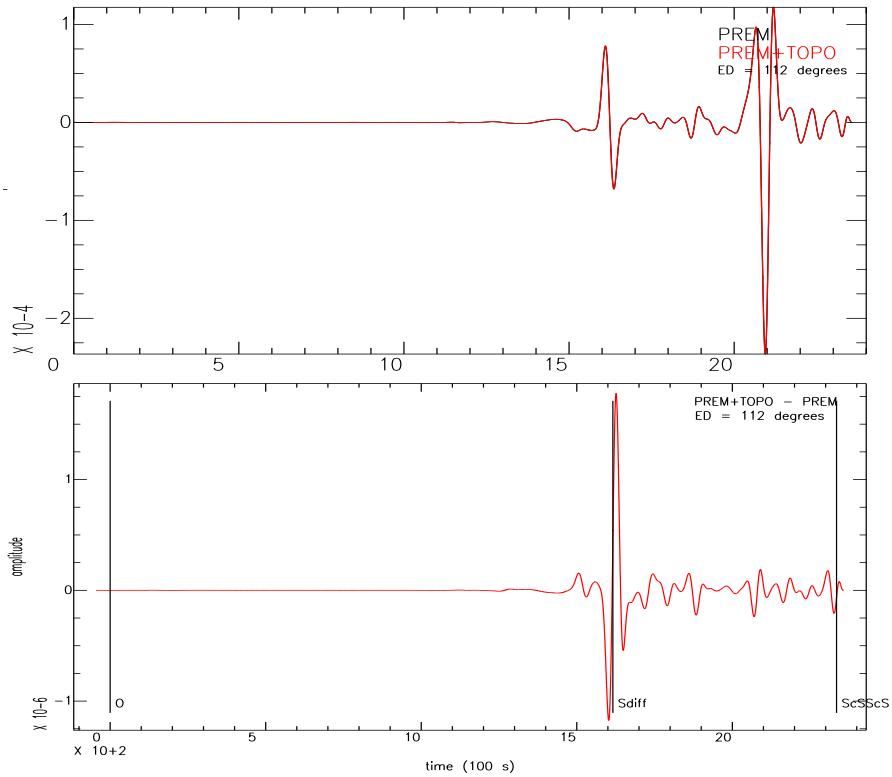

Figure 73: Station=1082, distance= 112°, SSS= 2345 s, SKiKS= 1543 s, SKIKS=1543 s, SKJKS=2173 s, PKKS= 1989 s, SKKS=1573 s, ScSScS=2335 s, Sdiff= 1616 s, PScS=1745 s, SKS=1513

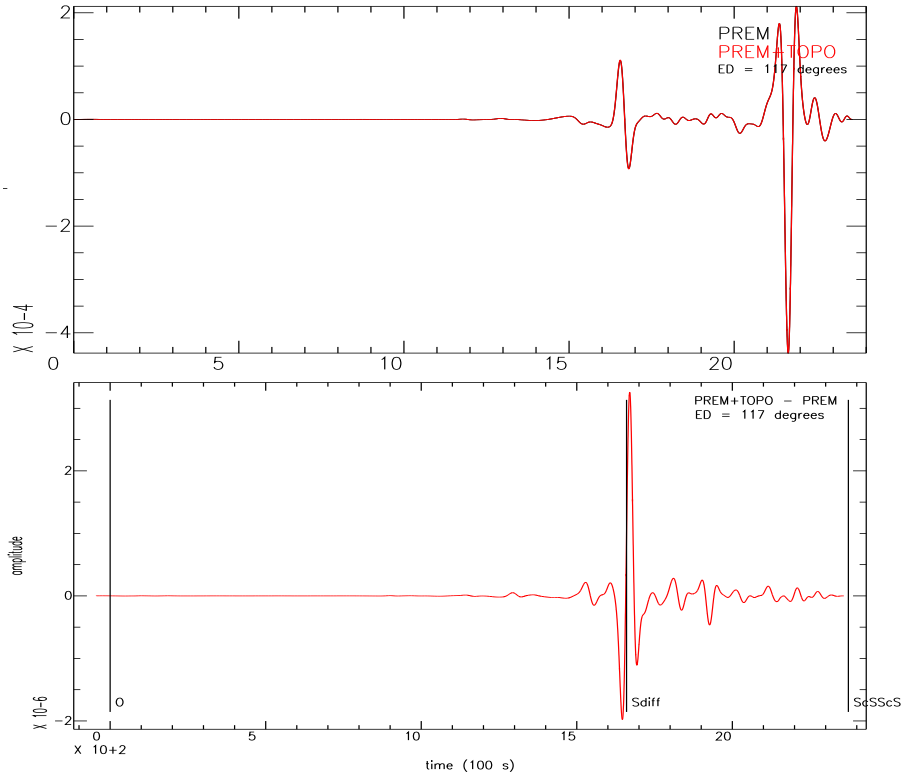

Figure 74: Station=1019, distance= 117°, SSS= 2424 s, SKiKS= 1553 s, SKIKS=1553 s, SKJKS=2163 s, PKKS= 1973 s, SKKS=1608 s, ScSScS=2373 s, Sdiff= 1660 s, PScS=1774 s, SKS=1534

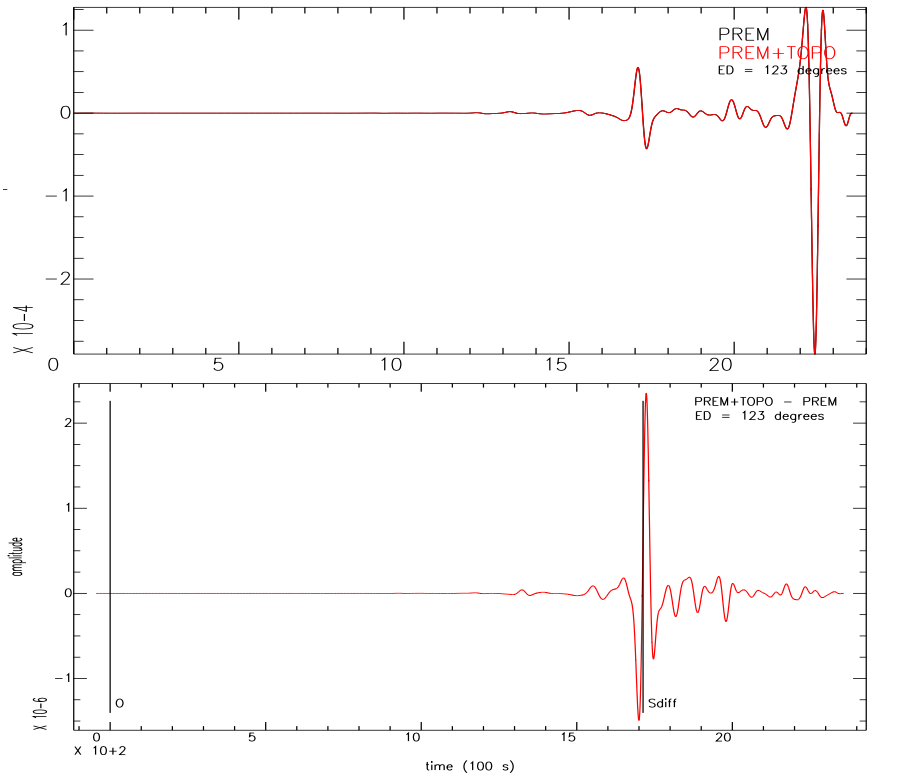

Figure 75: Station=1037, distance= 123°, SSS= 2518 s, SKiKS= 1566 s, SKIKS=1565 s, SKJKS=2151 s, PKKS= 1953 s, SKKS=1650 s, ScSScS=2420 s, Sdiff= 1713 s, PScS=1803 s, SKS=1555

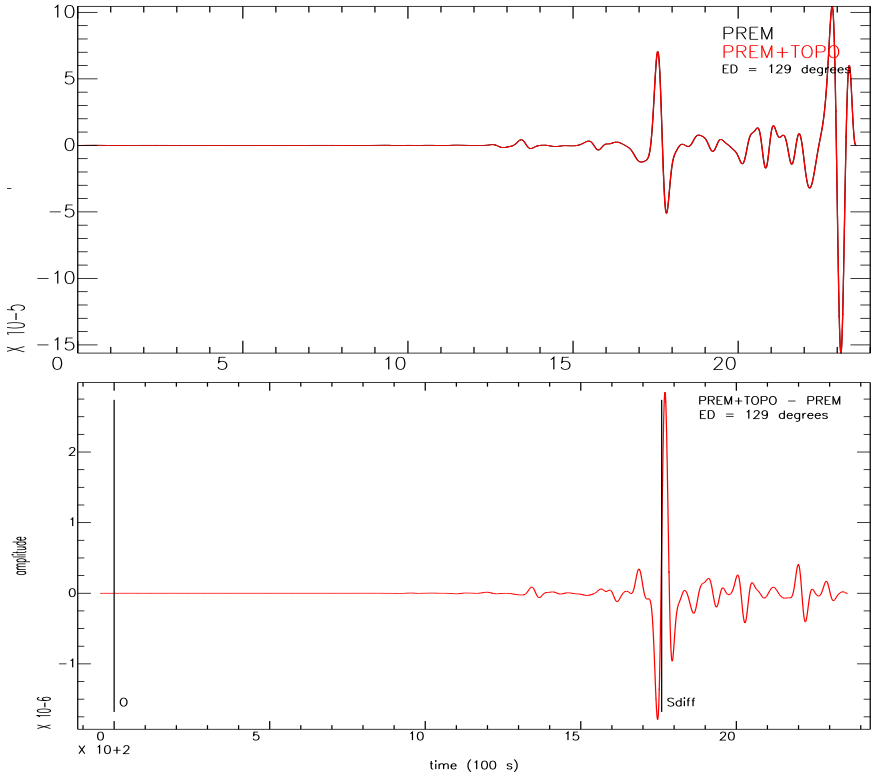

Figure 76: Station=1119, distance= 129°, SSS= 2601 s, SKiKS= 1578 s, SKIKS=1575 s, SKJKS=2141 s, PKKS= 1934 s, SKKS=1685 s, ScSScS=2462 s, Sdiff= 1760 s, SKS=1573

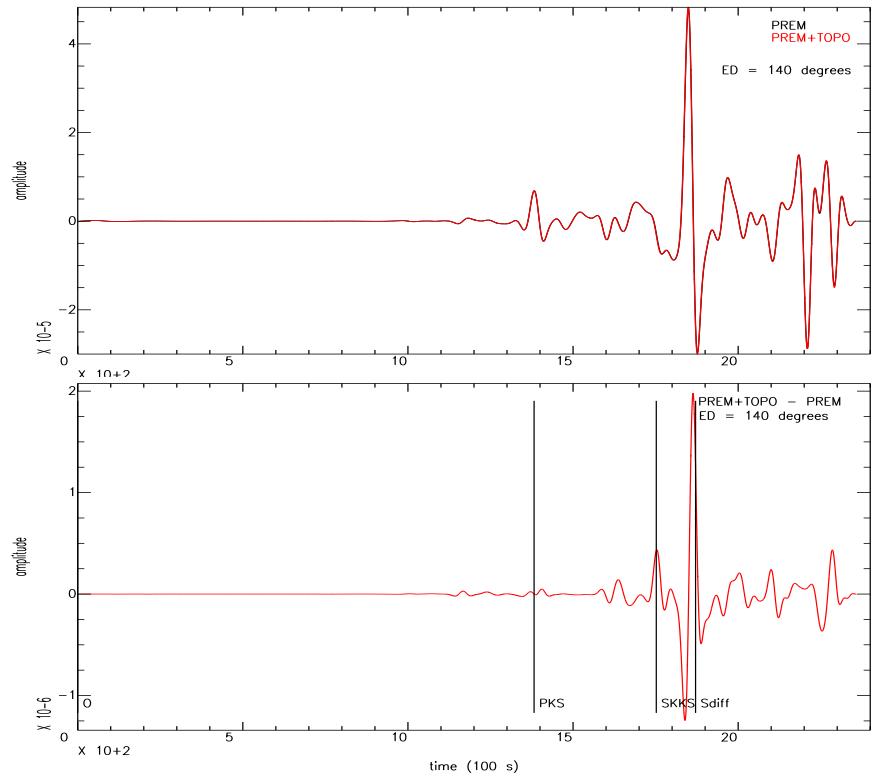

Figure 77: Station=1221, distance= 140°, SSS= 2758 s, SKiKS= 1600 s, SKIKS=1595 s, SKJKS=2123 s, PKKS= 1893 s, SKKS=1752 s, ScSScS=2547 s, Sdiff= 1851 s, PKS= 1382 s, SKS=1600

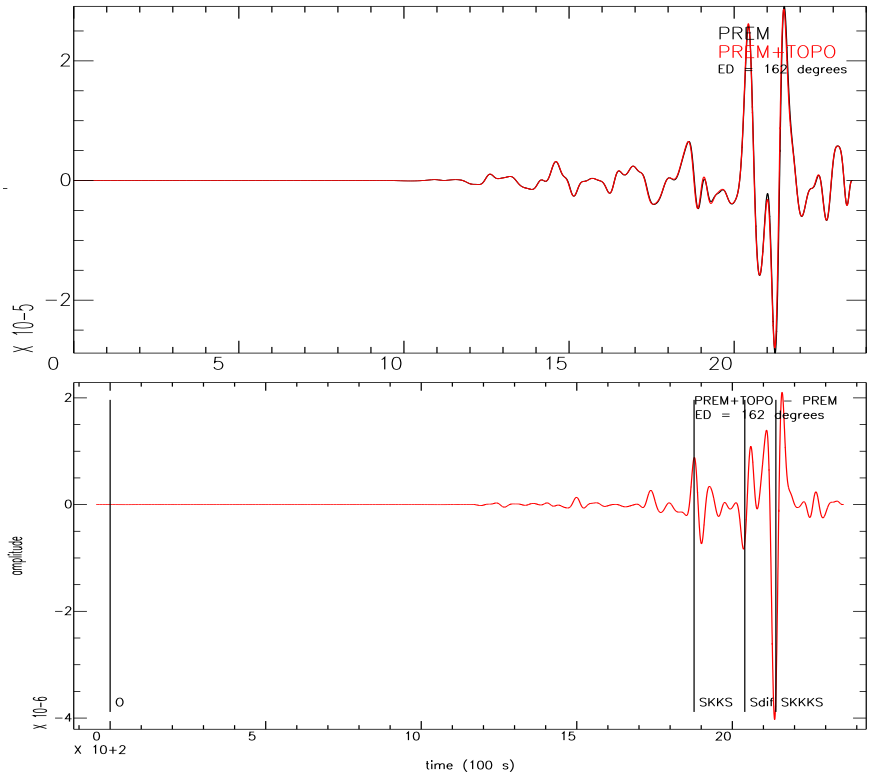

Figure 78: Station=1005, distance= 162°, SSS= 3073 s, SKIKS=1623 s, SKJKS=2095 s, SKKS=1877 s, ScSScS=2729 s,